NTNU – Trondheim
Norwegian University of
Science and Technology

Parameter study of electric power production in wind farms

experiments using two model scale wind turbines

Clio Ceccotti

Master's Thesis
Submission date: Januar 2015
Supervisor: Lars Sætran, EPT
Co-supervisor: Renato Ricci, Università Politecnica delle Marche

Norwegian University of Science and Technology
Department of Energy and Process Engineering

To my family,
for their wholehearted support.

Acknowledgments

I would like to thank Prof. Lars Roar Sætran, firstly for the big opportunity he gave me of working in this project, nevertheless, for his great help and for being an essential support, especially in the most frustrating moments, during the thesis work.

A thank is also addressed to NOWITECH research centre for its financial support.

At Università Politecnica delle Marche a thank goes to Prof. Renato Ricci for supervising this project from distance.

Many people have been involved in the project, so thanks to Andrea Spiga, Szymon Łuczyński and Piotr Wiklak for the countless hours spent together in the wind tunnel lab, and also to NTNU PhD Candidate Jan Bartl with whom I had several useful discussions.

I would like also to thank PhD candidate Pål Egil for his unlimited technical help and for conveying to instruments care to me.

A big thank to Debbie Koreman, Higher Executive Officer at NTNU Department of Energy and Process Engineering, for being extremely kind and patient with all my official papers.

A special thank goes to Fabio Pierella for his constant technical help (also from distance) and for teaching me that experiments can be hard but also enjoyable.

A final thank to all the people that make my Norwegian experience unforgettable: particularly, Manuel, Sara, Giovanna, Amro, Jolanda, Lorenzo, Annalucia, and all the others.

Trondheim, 21 January 2015

C.C.

Abstract

Wind farms are widely developed even if several unsolved problems need to be faced. The rotor-wake interaction involves different physical phenomena, not yet fully understood, directly affecting the overall wind farm power production. Numerical models and engineering rules have always been used to design wind farm layout but a spread between power predictions and results is verified. In this context wind energy research assumes a "back to basic" approach, by means of wind tunnel experiments, under controlled conditions, that represent the method to calibrate and correct the theoretical simulation models.

The aim of this project is to provide a useful set of wind tunnel measurements focused on the wake-rotor interaction analysis and on wind farm power output optimization. A benchmark is obtained, arranging a two-turbine wind farm, in order to calibrate numerical models and to show a wind farm case study.

Two three-blade wind turbine models are used in the present study. Despite some small geometrical differences, they are both equipped with the same blade-set, based on the NREL S826 airfoil, and they have a rotor diameter of $D = 0.9$ m.

A characterization concerning power performances and wake features of both turbines is performed, in order to obtain reference values for array efficiency assessment. The used reference velocity is set to $U_{ref} = 11.5$ m/s. Afterwards, the two models are arranged inline building a two-turbine wind farm case. Different tests are carried out varying several parameters: the separation distance between the models (3D, 5D and 9D), the inflow condition (low and high turbulence background level) and both turbines tip speed ratios.

First turbine wake measurements reveal that the velocity deficit recovery and the radial expansion of the wake are dependent on the flow turbulence. Higher the turbulence, faster the velocity recovery and bigger the expansion. As a consequence, high turbulence flows allow an earlier transition from near to far wake. Turbulence generation is analysed and related to the rotor operating point.

The array parametric study points out that the overall efficiency increases by moving further downstream the second turbine, rising the background turbulence level and by choosing a suitable operating point for each turbine. The analysis suggest to obtain the maximum wind farm efficiency by an accurate management of these different parameters: a strong reliance on downstream distance and on turbulence level is confirmed, smaller variations are found depending on the turbines operating point, but the relevance is still essential.

Contents

List of Figures

List of Tables

Chapter 1

Introduction

"Sustainable development is development that meets the needs of the present without compromising the ability of future generations to meet their own needs" [10].

1.1 Wind energy

Wind power has been extracted and used as an energy source since the 1st century BC, for grain-grinding or pumping water purpose (first known windmill historical reference). At the end of 19th century, after electrical generators appeared, the first modern wind turbine was built, converting energy into electricity. [2] This technology has not been extensively developed until late 1960s, when the environmental consequences of the industrial development came up. The mid-1970s Oil Crises gave a further push to find alternative energy resources: the so called sustainable energy.

The interest in renewable energy is increasing during the last decades, pushed also by European objectives as 20-20-20 by 2020. This agreement prescribes a 20% reduction in greenhouse gases emissions, a 20% increase in the consumed energy coming from renewable resources and a 20% improvement of the energy efficiency to be accomplished by the year 2020. In this scenario wind energy could be a big resource for a renewable energy mix. Moreover, on the economical aspect, it has to be considered that wind power reduces the exposure of our economies to fossil fuel price volatility. [11]

The world has reached on June, 2014 a total capacity of about 337 GW installed wind power. Only in Europe between 2000 and 2013 more than 100 GW of capacity was added. [12]

The latest trend in wind turbines is well described by the sentence *the bigger, the better*, which

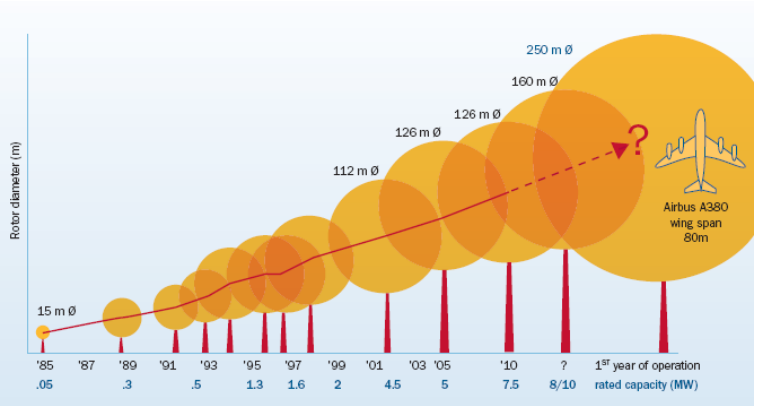

Figure 1.1: Trend in wind turbines size and capacity during the last decades

means that the turbines are increasing in size (tower height and rotor diameter) in order to have bigger capacity and to guarantee lowest installation and maintenance costs per MW installed. Bigger diameters allow a greater amount of available wind energy, at the meantime taller turbines benefit from higher flow velocities. Figure 1.1 is explicative of this trend. Off shore installations can benefit even more from high capacity machines. Lower infrastructures costs for foundation and sub-sea transmissions make larger rotors more competitive. Despite this, increasing the size, wake interference effects become a major issue.

Wind power suffers of high investment costs: stakeholders as investors, financiers or policy makers are highly responsive in predicting the future energy extraction from a wind farm. There are two main issues: predict the wind for a given location and knowing how much energy the turbines can extract for a certain wind speed. Wind forecasts features are out of the scope of the thesis; while for the knowledge of the power production of a turbine or a wind farm, predictions of rotor performances and wake-rotor interferences need to be made with the smallest error range. For this reason full scale and model experiments are promoted, as well as modeling.

1.2 Wind farm

The trend for wind energy is in arranging wind turbines in cluster. The main interest is in maximizing the energy extraction from a given land, additionally facilities required in a wind farm decrease in costs if the turbines are quite close. Installation and maintenance costs decrease for a wind farm with respect to the same extracted energy from turbines positioned far away from each other, especially when it comes to offshore facilities. Despite this, turbines cannot be located too close **one another**. As further described the wake behind a rotor is affecting the

available energy in the wind. A turbine that is positioned inline of another one, with respect to the wind direction, will suffer of the velocity deficit and the turbulence induced by the first.

The minimum distance of approximately 10D is necessary to fully recover the wake flow to the velocity freestream condition, while even higher distances could be recorded as regards the turbulence intensity recovery [13]. However, due to the dimension of the given land and the infrastructural cost the economical optimum is often reached for smaller downstream separations. Modern wind farms are usually spaced around 7-8D in the main wind direction, and even closer in cross wind direction [14, 15]. Additionally to the optimization of power production and cost-effectiveness, structural loads need to be highlighted. The wake is characterized also by an increase of turbulence level that could be responsible for fatigue issues. Peculiar excitation frequency should be considered for structural integrity of blades and tower.

For this reason wake issues increase. The importance of understanding and estimating wake rotor interaction is evident.

The minimization of array losses is possible only after a good insight on the wake issue; and this is still not reached. Experiments and numerical simulation can be used together to obtain the best results. Experiments on full scale wind turbines are suffering of unknown freestream conditions, lack of a systematic data bank and above all they are very costly and time consuming. Numerical simulations are instead very flexible, less expensive and faster, but they need to be validated as they relies on approximations. In this scenario wind tunnel experiments fit. Even if they are limited in terms of scaling to the real wind turbines, they can be used for models validation and can provide innovative insights into the physics of the problem.

1.3 Motivation and outline of the thesis

The main objectives of the thesis can be summed up as:

- improve the insight in the physics of wind turbine rotor-wake interaction, by experiments on the 2-turbines array.
- create a benchmark for calibrating numerical models, in which all boundary conditions are well described and documented, so are the results.
- study different parameters affecting the wind farm power output, prioritizing the overall efficiency instead of the single turbine.

- find a criteria for optimizing the total power production for this peculiar wind farm, consisting of a row of 2 inline machines

The experimental investigation, carried on during the present thesis, consists of power and thrust performances measurements, as well as wake characterization in different configurations. The parameters that have been considered while analysing the turbine array are: the downstream separation distance between wind turbines, the tip speed ratio for both machines, and the turbulence level in the incoming wind.

Three downstream distances are examined: 3D, 5D and 9D. In all cases the turbine are positioned inline.

As regards the tip speed ratio, both turbines values are varied over a quite wide range crossing the optimum value. The usual operating mode of a real machine is to set the pitch angle, the tip speed ratio and the yaw angle in order to extract as much energy as possible from the inflow wind of each turbine. It means that every wind turbine operates with the maximum power coefficient for lower than rated wind speed. However, in a wind farm, this operating mode is not optimum in terms of overall efficiency because of wake effects induced by each row of turbines on the downwind ones. It might be possible to find a different strategy for maximizing the wind farm efficiency. In recent studies as [16, 17, 18, 19, 20] the possibility of varying the tip speed ratio from the optimum point is analysed. Other parameters could be varied at this purpose such as the pitch angle of the rotor blades, the yaw angle of the turbine and the lateral shift considering the wind direction, but they will not be analysed during the present work.

The last parameter investigated is the inflow condition, two different cases are studied: a low turbulence level, typical of a wind tunnel test section, and a high monitored turbulence level, built through the interposition of a meshed grid at the inlet of the test section. It is able to generate an homogeneous and isotropic turbulence [21], and it is characterized by 10% of turbulence intensity on the first rotor plane. When analysing wind turbine performances in a wind tunnel, one of the major limitations is represented by the low turbulence incoming flow. In real life operations a turbine works in the atmospheric boundary layer, which is typically characterised by a turbulence intensity of the order of 10-15%. Slightly smaller values can be observed in offshore conditions. Turbulence intensity strongly affects both wind turbine performances and wake development, modifying the wake-rotor interactions for a row of machines. For this reason in the current thesis work, one of the investigated parameter is the dependency on turbulence background level.

Chapter 2

Aerodynamics of wind turbines

The second chapter of the present thesis deals with some basics on wind turbine aerodynamics. The purpose is to give an overview of the phenomena described in the following.

2.1 Definitions

This section summarizes some of the main parameters used to describe the operation of a wind turbine.

The rotational velocity of the main shaft is usually adimensionalized as the *tip speed ratio*. It represents the ratio between the tangential velocity of the blade tip and the free-stream (reference) velocity as stated in the following:

$$TSR = \lambda = \frac{\omega R}{U_\infty} \tag{2.1}$$

where R is the rotor tip radius [m], ω the rotational velocity (in [rad/s]) and U_∞ the undisturbed free stream velocity, upstream from the rotor [m/s].

The local speed ratio along the blade id calculated using the radius r instead of tip radius R:

$$\lambda_r(r) = \frac{\omega r}{U_\infty} \tag{2.2}$$

The main parameters used for describing turbine performances are the *power coefficient* C_P and

the *thrust coefficient* C_T. They are conventionally defined as:

$$C_P = \frac{Power}{\frac{1}{2}\rho {U_\infty}^3 A_d} \tag{2.3}$$

$$C_T = \frac{Thrust}{\frac{1}{2}\rho {U_\infty}^2 A_d} \tag{2.4}$$

where A_d is the rotor swept area, so $\frac{1}{2}\rho {U_\infty}^3 A_d$ is the wind total power crossing the rotor section, and $\frac{1}{2}\rho {U_\infty}^2 A_d$ a dynamic reference force. It will just be reminded that the torque acts in the tangential direction, that is perpendicular to the wind. The power is calculated multiplying the generated torque by the rotational speed ω. The thrust is the force acting in the axial direction, thus in the air flow orientation.

2.2 Rotor aerodynamic theory

2.2.1 Momentum theory and actuator disk concept

A wind turbine is extracting kinetic energy from the wind, so the flow slowed down when passing through the rotor, converting wind energy into the main shaft rotation. The simplest model describing this phenomenon is the ideal actuator disk model and it is generally attributed to Betz (1926). It can be used to determine:

- The ideal power available for being extracted by a wind rotor.
- The thrust on the ideal rotor.
- The effect of the flow after passing through the rotor (wake).

For a detailed description of the method see [2, 1] , just a brief introduction will be given here.

In this model it is considered just the energy extraction process, without any focus on the design of the turbine. The main flow assumptions are: steady, inviscid, incompressible and irrotational. Moreover only axial forces act on the turbine. A stream tube is setted as control volume, as in Figure 2.1. Assuming no air passing throw the lateral walls of the stream tube and neglecting air density changes ($Ma < 0.3$ that under normal air condition means $U_\infty < 100$ m/s) the mass

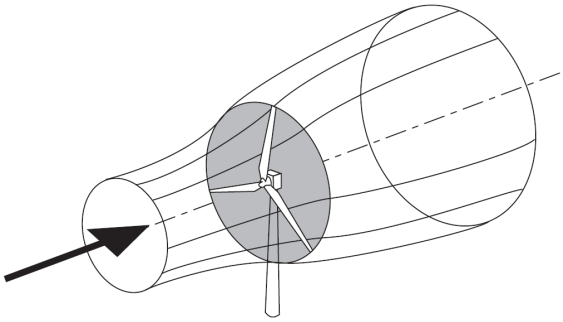

Figure 2.1: Stream tube [1]

continuity equation can be written:

$$\rho A_\infty U_\infty = \rho A_d U_d = \rho A_w U_w \tag{2.5}$$

The subscript ∞ refers to the upstream undisturbed flow, d to the rotor plane and w to condition in the far wake as in Figure 2.2. It is possible to see the velocity trend at different downstream positions, as well as the step change in pressure on the rotor plane which is the reason of the energy extraction process. The static pressure increases from its upstream undisturbed value (p_∞) to p_d^+, before dropping suddenly on the rotor plane. This pressure difference ($p_d^+ - p_d^-$) is associated to the axial force exerted on the disk. Then the pressure gradually recovers in the wake to the free stream value p_∞.

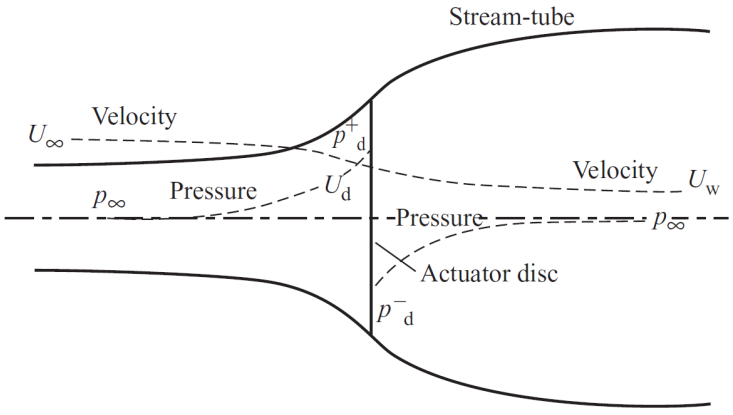

Figure 2.2: Actuator disk model [1]

This model introduces the axial flow induction factor a, defined as the ratio between the streamwise velocity reduction (the difference between the undisturbed flow and the flow at the rotor

plane) and the free stream velocity as in Equation 2.6.

$$a = 1 - \frac{U_d}{U_\infty} \tag{2.6}$$

Defined the *power coefficient* C_P and the *thrust coefficient* C_T as in Section 2.1; it can be demonstrated that the power and the thrust coefficients can be expressed as a function of the axial induction factor by:

$$C_P = 4a(1-a)^2 \tag{2.7}$$

$$C_T = 4a(1-a) \tag{2.8}$$

The air after passing the rotor cannot be reduced to zero for mass continuity, thus there is a limit in power coefficient even for an ideal, loss-free system. By differentiating Equation 2.7 with respect to a, it can be found that the maximum achievable power coefficient ($C_{P,max}$) is $\frac{16}{27}$ and it is called *Betz limit*. This limit does not take into account any kind of losses that are present in a real case, especially the energy loss in the wake rotation, in viscous friction and by the finite number of blades. So this is an upper conservative limit that no real machine can exceed.

At optimal C_P, the thrust coefficient C_T is equal to $\frac{8}{9}$. Note that, as the velocity is decreasing behind the turbine, for mass conservation $A_w > A_d$ leading to the expansion of the wake. The higher C_T, the larger the expansion.

2.2.2 Rotary disk theory

When passing over the blade, airflow induces forces on it producing blades rotation. According to the Newtonian laws, equal and contrary forces are exerted by the rotor on the flow, resulting in a flow rotation in the wake in the rotor's opposite direction. The rotor imparts to the flow a rotational component of velocity, increasing its rotational kinetic energy that is a certain source of energy loss [2]. It means that the efficiency of a real turbine is quite far from the Betz limit, where no wake rotation is assumed. This limit is commonly referred as *Glauert's limit*, considering Glauert's work [22].

For a complete discussion of the theory refers to [2], here it will just be underlined the dependency of the $C_{P,max}$ from the TSR, for future comparisons. Defined the tip speed ratio as in Equation 2.1, in Figure 2.3 the Glauert's maximum power coefficient is plotted against the Betz limit. It can be noticed that the losses due to wake rotational effects are reduced as the tip speed ratio gets higher.

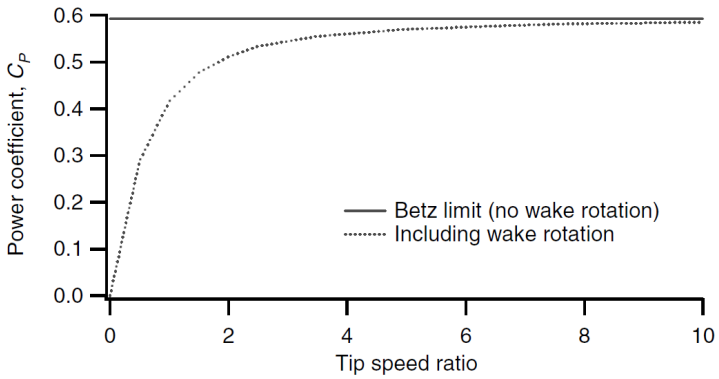

Figure 2.3: Power coefficient: Glauert's limit [2]

2.2.3 Blade element theory and Blade element momentum theory (BEM)

In the previous theories the geometry of rotor blades is not considered, but to be able to calculate the efficiency of a real rotor it is needed to couple the aerodynamic characteristics of the airfoil with the momentum theory previously analysed.

The Blade element theory is the mathematical process, involving dividing a blade into several small parts, between different radii (as in Figure 2.4). Each element is considered totally independent from the others and the forces on each element are calculated from lift and drag coefficient of the airfoil. After the forces are determined on each element, they have to be integrated along the blade and over one rotor evolution.

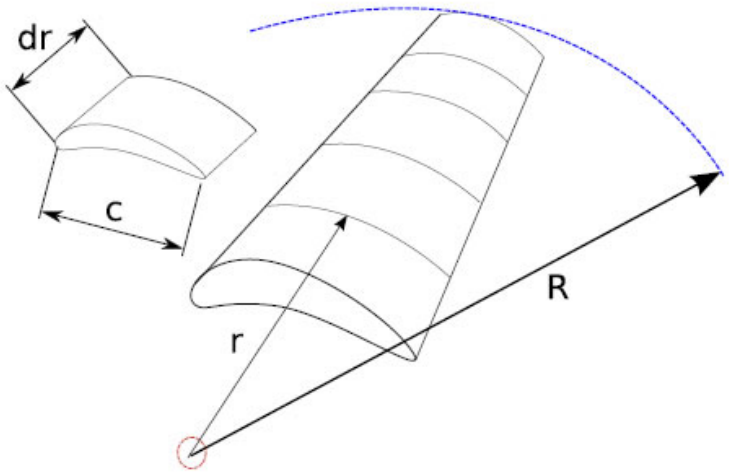

Figure 2.4: Blade element

The Blade element momentum theory combines both blade element theory and momentum theory. It differs from the momentum theory because the forces are produced by the blade instead of an actuator disc. The BEM theory (fully described in much of the literature [2, 1, 23, 3]) is mainly used to analyse the performance of wind turbine blades in steady state conditions.

Assuming that the airfoil theory is also valid for a wing element of limited length, the BEM method requires to divide the finite blade in an infinite number of blade elements and calculate the forces acting on each blade element. These forces match the ones coming from a flow annulus, derived by the momentum theory.

Few assumptions have to be taken into account. The following has to be assumed:

- The wind speed and direction has to be constant, so the flow around the blades will behave in a so-called steady state situation.
- There has to be a uniform wind speed over the whole turbine rotor, so the wind shear due to the boundary layer-effects of the terrain is neglected.
- There is no flow in the radial direction of the blade, so each blade element is totally independent of the others.
- The blades have a perfect stiffness and does not flex or bend.
- The forces on the rotor sections can be calculated by the 2D characteristics of the blade airfoil.

Because of these assumptions, a lot of factors are not taken into account. Nevertheless, by using this simple method one can be able to give good a first estimation of the average performance of the turbine. After the forces are calculated on all infinitesimal elements, they are summed up to get the total forces on the rotor. Referring to the relative velocity on the airfoil, infinitesimal lift and drag can be calculated, and then the resultant forces acting on each blade element can be decomposed along the axial and the rotational direction, respectively thrust and torque forces.

For applying this method C_l and C_d airfoil coefficients have to be known.

The major weaknesses in basic BEM are [24]:

tip losses A flow around the blade tip due to pressure differences is not take into account, but a correction factor can be applied (for example Prandtl's one) [22]

Wind shear The incoming flow is stationary by assumption, varying the wind with height, the variations appear to the individual blade element as highly unsteady.

Turbulence Small scale turbulence creates different wind speed in different points on the blade and this factor cannot be considered.

Dynamic inflow All temporal variations cannot be studied.

2.3 Wake aerodynamics

The wake behind a wind turbine is the result of interactions between incoming flow and turbine's blades. Wake fundamental aspects of a wake are momentum deficit and increased level of turbulence as it has already been investigated by [25]. Moving far downstream of rotor plane, the characteristics of the wake heavily changes due to multiple parameters. The evolution of the wake features have inspired researchers to divide the wake region in different parts. A widely shared classification led to distinct 2 areas:

1. Near wake
2. Far wake

A schematic representation of these areas is shown in Figure 2.5. In the following sections a review of these characteristics is presented.

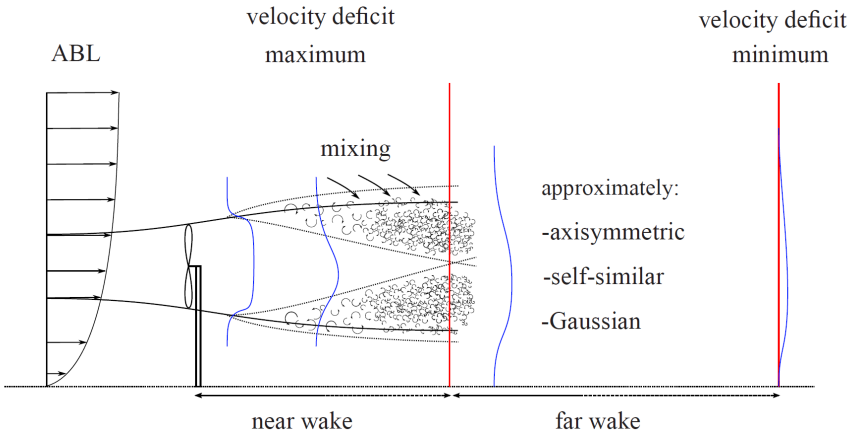

Figure 2.5: Wind turbine wake schematization [3].

2.3.1 Near wake

Vermeer et al. [25] consider the near wake as the area just behind the rotor where the properties of the rotor can be recognized. In this area, rotor characteristics such as number of blades,

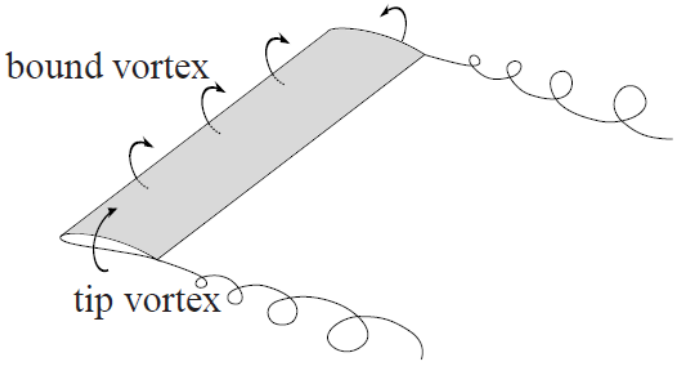

Figure 2.6: Tip and Bound vortices [3].

blade aerodynamics, 3D effects, tip and root vortices are distinguishable. Due to this aspects, near wake researches are focused on performance and power extraction mechanisms, trying to relate physical aspects in the wake to blade's aerodynamic features. The extension of this area is not well defined, the length is highly dependent on several parameters that make it varying from time to time. Generally a length up to 1D downstream the rotor plane is established in a full-scale turbine case. The near wake extension is mainly dependent on the background turbulence level. Lower the turbulence, longer the near wake region. In off-shore wind turbines, because of the lower turbulence with respect to on-shore situations, longer extensions are found. For the same reason, wind tunnel experiments, characterized by a very low turbulence inflow, present the longest near wake [26].

In order to understand the flow characteristics in the wake some 3D aerodynamic key-concepts are called to mind. Considering a wing, it can be represented as a finite length structure with airfoil cross-section. In order to generate lift over it, a pressure difference between the lower and upper surfaces needs to be created. As it is a finite length structure, at the tip the pressure difference is unbalanced; air flows around the tip from higher to lower pressure side; therefore, at the wing extremities, tip-vortices are generated. The lift generated over the wing can be attributed to a distributed bound vortex via Kutta-Joukowski law: $L = \rho V \Delta\Gamma$. Bound vortex and tip vortex form a horseshoe vortex. As depicted in Figure 2.6, the two tips vortices have the same intensity but opposite sign so they are in balance.

It can be demonstrated that the vortex system generated by a finite wing induce a down-wash velocity. When calculating the wing performances, this effect is considered by reducing the geometric angle of attack. For a deeper insight in the finite wing theory refers to [27].

A wind turbine blade is a "rotating wing" so tip vortices at the blade tip and root vortices at the hub are shed.

As previously explained, wing tip vortices have opposite rotating direction each other, similarly in a wind turbine blade, root and tip vortex rotate in the opposite direction.

Considering a three blade turbine rotating counter-clockwise when seen from upstream as in Figure 2.7, tip vortices will produce a spiral that is rotating in the opposite direction. Respecting the Newtonian laws, the rotor imparts to the wake a torque equal and contrary to that one exerted by the fluid on the rotor.

The wake structure in the near wake region is influenced by the distribution of the bound circulation along the blade and so it depends on the rotor performances.

In a design condition, the lift distribution over the blade can be considered approximately constant. According to Kutta-Joukowski law, even if the circulation $\Gamma(r)$ is constant, close to tip and root, a strong gradient established, leading the lift to zero value and resulting in the vortex generation. Out of the design condition, in addition to tip and root vortex, other vortexes can be originated so that the lift and circulation distribution are not constant anymore along the blade. Corresponding to a circulation gradient, a vortex sheds into the wake [14, 4]. Furthermore the velocity induced by the vortex system affects the blades local inflow conditions, thus the aerodynamic forces over the blade can not be calculated by using the geometric angle of attack: corrections need to be applied.

These phenomena are visible into the near wake region so, studying the flow in this region, useful information can be extracted about the rotor blade functioning.

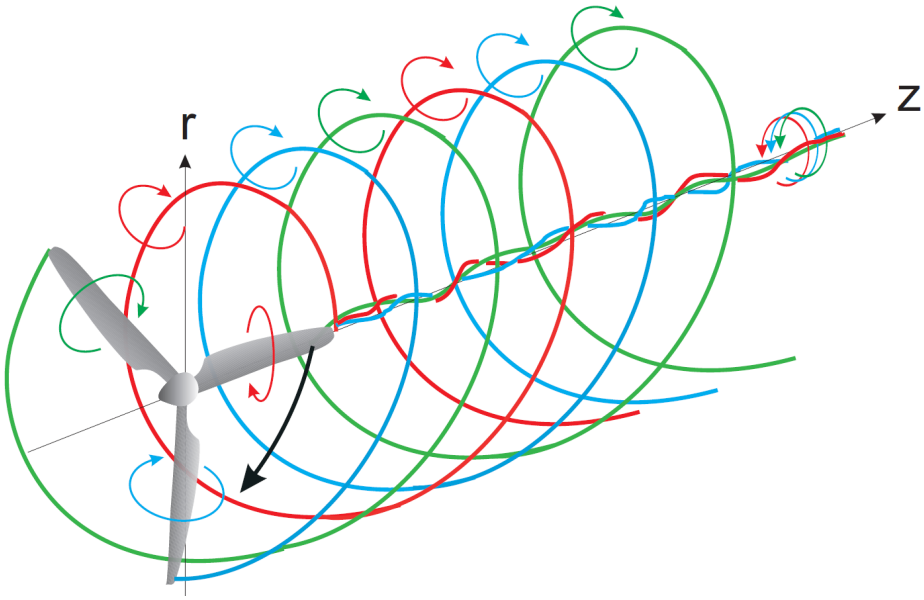

Figure 2.7: Turbine blade's vortices [4].

2.3.2 Far wake

The far wake region, as Varmeer et al. [25] describe, starts when the shear layer of the near wake reaches the wake axis; it was found that a good approximation is to consider the beginning of this region between 2 to 5 diameters downstream the rotor plane. Different features characterize the far wake region compared to the near wake ones. Peculiar velocity deficit profiles and turbulence intensity distributions distinguish this region.

The wake is considered completely developed, so an axisymmetric behaviour and absence of streamwise pressure gradient $\left(\frac{\partial P}{\partial x} = 0\right)$ can be assumed (refer to Figure 2.2). Velocity deficit and turbulence intensity result in a self-similar (Gaussian) distribution in the cross-section. In reality those assumptions are too strict. Observations have demonstrate that the point of maximum velocity deficit is below the turbine axis and the point of maximum turbulence intensity above it, as it is pointed out in [28]. For this reason, the ground presence and the ambient shear flow have to be taken into account to better describe the far wake behaviour.

The velocity deficit recovery is more rapid than the decay of turbulence intensity. As argued in [13] turbulence intensity is still noticeable after 15D while velocity deficit is usually almost negligible. The wake recovery is highly dependent on background turbulence level. Higher is the turbulence in the free flow, faster is the wake recovery because of the greater momentum fed into the wake by the turbulence itself. For this reason, wind tunnel experiments on model turbines with low background turbulence show a larger distance for a full wake recovery. According to this theory, several experiments [14, 29] show that velocity deficit and turbulence intensity are not restored to the free stream values at 15D downstream the rotor.

In this region, efforts are focused on analyzing wind turbine interferences when arranged in cluster by defining wake models, wake interferences features and turbulence models.

2.4 Characteristic curves of a wind turbine

When describing turbine performances, it is convenient to express them by means of non-dimensional parameters, obtaining dimensionless curves characteristics of the turbine. C_P-λ and C_T-λ curves are the most important.

The C_P-λ curve is the usual method of presenting the power performance of a wind turbine. In Figure 2.8 an example of a performance curve for a modern wind turbine is depicted.

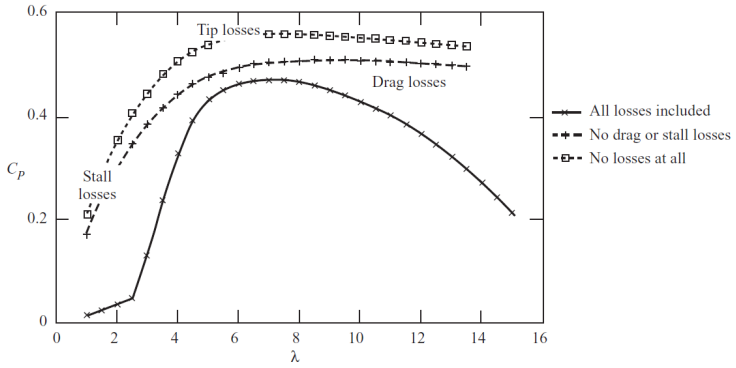

Figure 2.8: Wind turbine C_P curves [1]

Comparing it to Figure 2.3 in which the Betz limit and the Glauert's corrected curve are reproduced, it has to be underlined that several corrective factors have to be considered. Modern three blades, horizontal axis wind turbines usually reach a maximum C_P value of around 0.45 to 0.50 [2] which is significantly below the Betz limit. These differences are due to several aerodynamics but also mechanical (bearings and gearbox) and electrical-conversion losses.

The real C_P curve features a maximum point at a certain tip speed ratio λ for which the ideal flow conditions are achieved in every section of the blade; it means that the optimal angle of attack occurs leading to the maximum airfoil performances. This is usually the design operating configuration.

At lower than the design tip speed ratio λ, negative angles of attack in the inner sections of the blade causes aerodynamic stall. This segment of the curve is usually referred as "stalled region" [30]. Decreasing the tip speed ratio, the stall will affect a bigger part of the blade, until the whole blade is stalled and there is no power production.

At higher than design tip speed ratios the power is still increasing, but the power coefficient is not. The angles of attack on the airfoils get bigger, thus the flow is separated in a sector of the blade profile and causes a considerable amount of drag which decrease the efficiency of the wind turbine [1].

Raising the tip speed ratio, the inner part of the blade starts acting as a propeller, energizing the fluid, while the outermost part is still extracting energy from the wind. When the amount of energy imparted to the flow and extracted are in balance, the C_P reaches the zero value. This operating point is called "run-away" as it would be the working condition for a wind turbine that is not connected to an electrical generator but is left free to rotate.

The other characterizing curve for a wind turbine rotor is the C_T-λ. The C_T parameter is very important for the construction of the rotor support and the structural design of the turbine tower. [1]. The thrust coefficient continuously grows with increasing tip speed ratio. An example of the thrust curve is depicted in Figure 2.9. In the transition zone, from the stalled region to the optimal tip speed ratio, a smaller gradient can be observed ($\lambda \approx 4$ in Figure 2.9) because the not-stalled regions present a smaller drag. After reaching the optimal tip speed ratio the slope is quite constant.

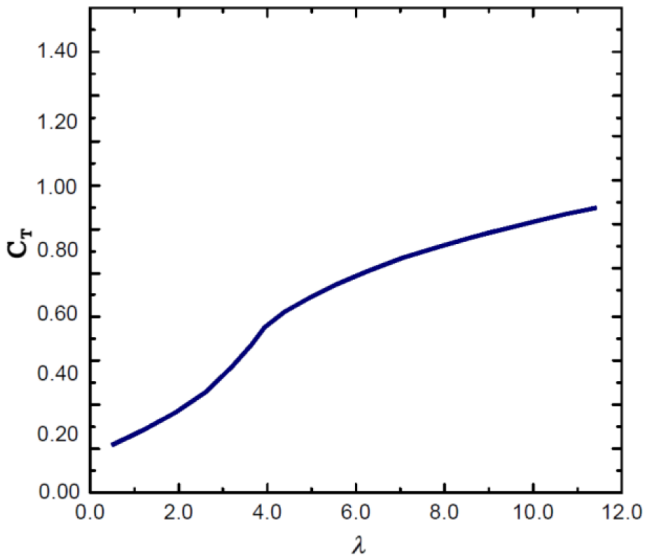

Figure 2.9: Wind turbine C_T curve example [5]

Chapter 3

Experimental Setup and Methodology

In this chapter, a description of experimental facility, instruments and model turbines are introduced, then the methodology used to elaborate the experimental data are shown and explained.

3.1 Wind tunnel

The experimental study is performed in the main wind tunnel at the Department of Energy and Process Engineering at NTNU (Trondheim). It is a closed-loop wind tunnel as it is shown in Figure 3.1. The driving fan can achieve a maximum power of $P = 220$ kW which leads to a maximum wind speed of $U_\infty \approx 30$ m/s in condition of empty tunnel. After passing through the fan, the air is canalized in the upper part of the tunnel, where several grids and honey combs are used to decrease the turbulence level; then the test section inlet contraction is used to speed up the flow before entering the test section. The latter is 2.71 m wide and 11.14 m long and it has a flexible roof that has been adjusted to have a zero pressure gradient along the test section at a speed of $U_\infty \approx 14$ m/s. The tunnel heights are shown in Table 3.1.

X (m)	Height (m)
0.000	1.801
1.281	1.801
5.621	1.813
8.435	1.842
11.150	1.851

Table 3.1: Wind tunnel test section heights

Section 4.1 will be spend defining the main flow characteristics in the wind tunnel.

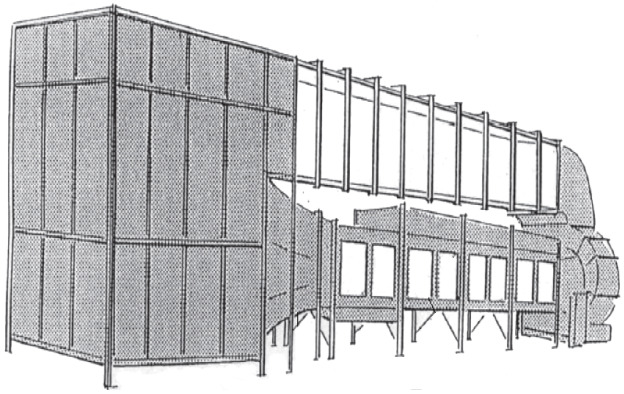

Figure 3.1: NTNU wind tunnel [6]

Inside the test section an automatic traverse mechanism is installed. It enables the accurate positioning of measurement instruments, as well as the movement while experiments are running. The position of the probe can be controlled by a computer in three-dimensions using a dedicated LabVIEW® software.

3.2 Model wind turbines

Two model wind turbines are used for the present study, they are equipped with the same set of 3 blades, but present some differences in the tower and hub. The model and blade geometry was completely designed at NTNU and it is fully described in [8]. Only the main features will be shown here.

3.2.1 Airfoil

The rotor was designed with three blades using the NREL S826 airfoil (shown in Figure 3.2) throughout the span.

This is a 14 % thickness profile, designed by NREL for being used close to the tip of full scale wind turbines [31]. It is studied to be optimal at $Re = 2 \cdot 10^6$, in this condition it gives a high lift (C_L= 1.42), a gentle stall (due to a separation ramp close to the trailing edge on the suction side) and it is quite insensitive to roughness. This insensitivity is due to an early transition to turbulence on the suction side; this aspect is one of the reason why this profile was chosen, in fact the early transition ought to also reduce Re dependency behaviour and this is a good feature as it will be used in a model scale in which the Re number is usually much lower than in a full scale wind turbine.

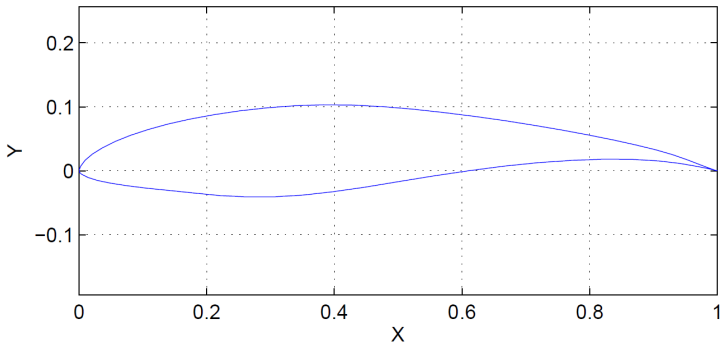

Figure 3.2: Blade profile: airfoil NREL S826

The airfoil NREL S826 was tested for Reynolds numbers between Re= 10^6 and Re= $3 \cdot 10^6$ by Somers [31] , and from Re= $4 \cdot 10^4$ to Re= $1.2 \cdot 10^5$ by Sarmast [7] (results are shown in Figure 3.3). The results obtained for lower Reynolds numbers are comparable with the high Reynolds starting from $1 \cdot 10^5$, below this value airfoil performances are quite different and present hysteresis in the lift and drag curve, both in the pre-stall and post-stall regions. However, approaching Re=10^5, the airfoil characteristics tend to the ones at high Reynolds numbers (10^6) and this is a beneficial behaviour in terms of scaling the experiment (see Section 3.2.3).

The Reynolds dependency is connected with separation phenomena. According to [8, 32, 33], this effect can be related to a laminar separation bubble near the blade leading edge on the suction side. This argumentation is supported by data on airfoil coefficients presented in Figure 3.3. The different behaviours at low Reynolds numbers clearly respect the creation of a separation bubble.

3.2.2 Models description

The turbine models used in this study have a slightly different geometry, even if they are equipped with the same set of blades. All dimensions are presented in Figure 3.4(a) and 3.4(b). It is possible to see that turbine T1 presents a bigger hub, which results in having larger rotor diameter (D_1= 0.944 m) than turbine T2 (D_2= 0.894 m).

Both turbines has a 0.37 kW motor, controlled via a SIEMENS®Micromaster 440 frequency converter, which is able to finely adjust the rotational speed of the turbines. The rotor can operate up to 3 000 rpm, the converter allowed power to be consumed from or to be supplied to the motor. When the turbine is producing power, it is dissipated in a 300 W electrical heater.

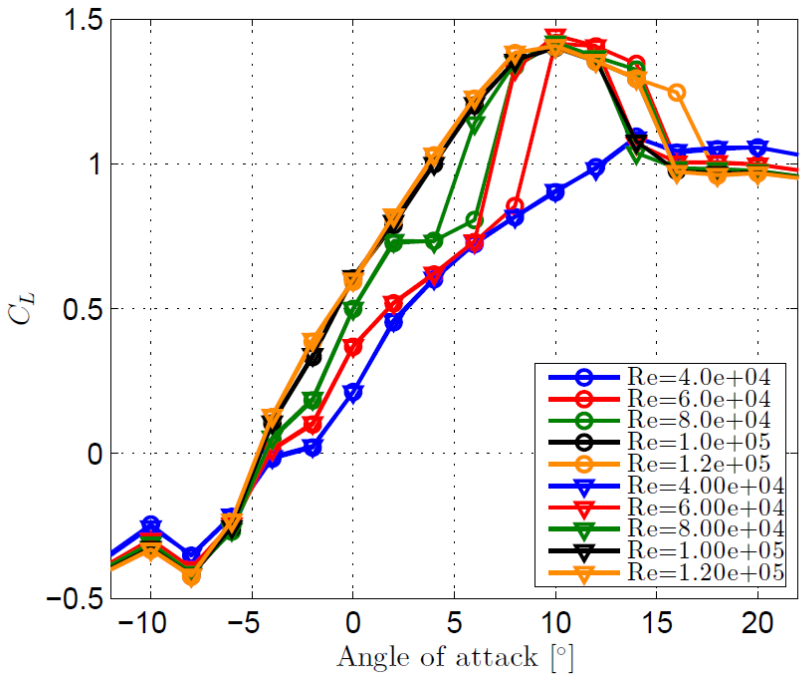

Figure 3.3: Lift coefficient of airfoil NREL S826 tested at low Reynolds numbers [7]

Blockage

Analysing the performances and wakes of a turbine in a closed test section the effect of the blockage has to be considered as it can increase the calculated performances as well as disturb the wake expansion (see Section 2.3). The velocity tends to rise in the tunnel as a consequence of the reduction of the available section for the undisturbed flow around the turbine.

The solid blockage for the turbine model T1 (the bigger one) inside the NTNU wind tunnel is 14.2%. It represents the ratio between the rotor swept area ($\frac{\pi}{4}D_1^2$) and the cross section of the wind tunnel. Some older experimental results [25, 34] suggest not to exceed 10% when analysing turbine performances in a closed test section, even if our value is slightly bigger it is not considered an issue as in numerical simulation it can be taken into account adding test section walls.

Another aspect of the blockage that has to be discussed regards the wake expansion. The interference of the wind tunnel floor can be approximated with the one of the ground in a full scale turbine, as the tower height is quite respected considering the scaling factor. Walls interference can be compared to the one presents in a real wind farm from other turbines on the sides. The main problem regards the roof of the tunnel that let not the wake expand freely in that direction and considerably deform the shape of the wake. It has to be remembered that as a test case, all these factors can be taken into account in a simulation, so it will not be further discussed.

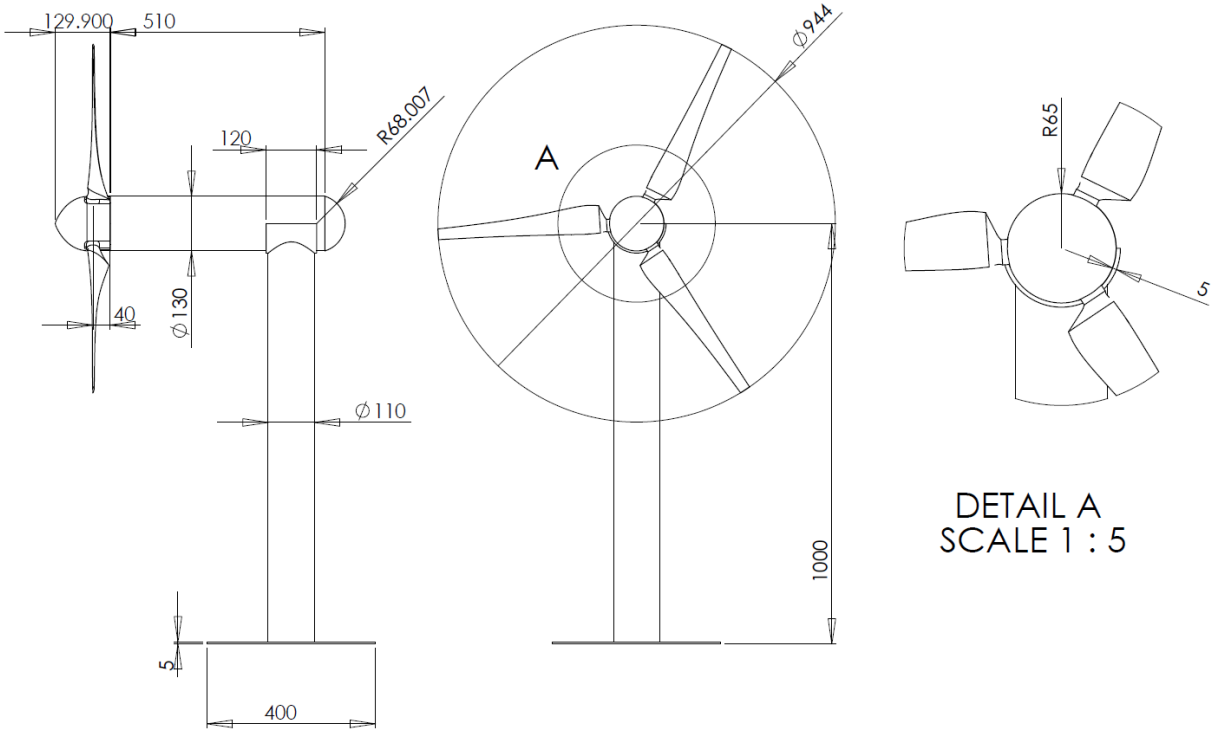

(a) First turbine (T1) geometry

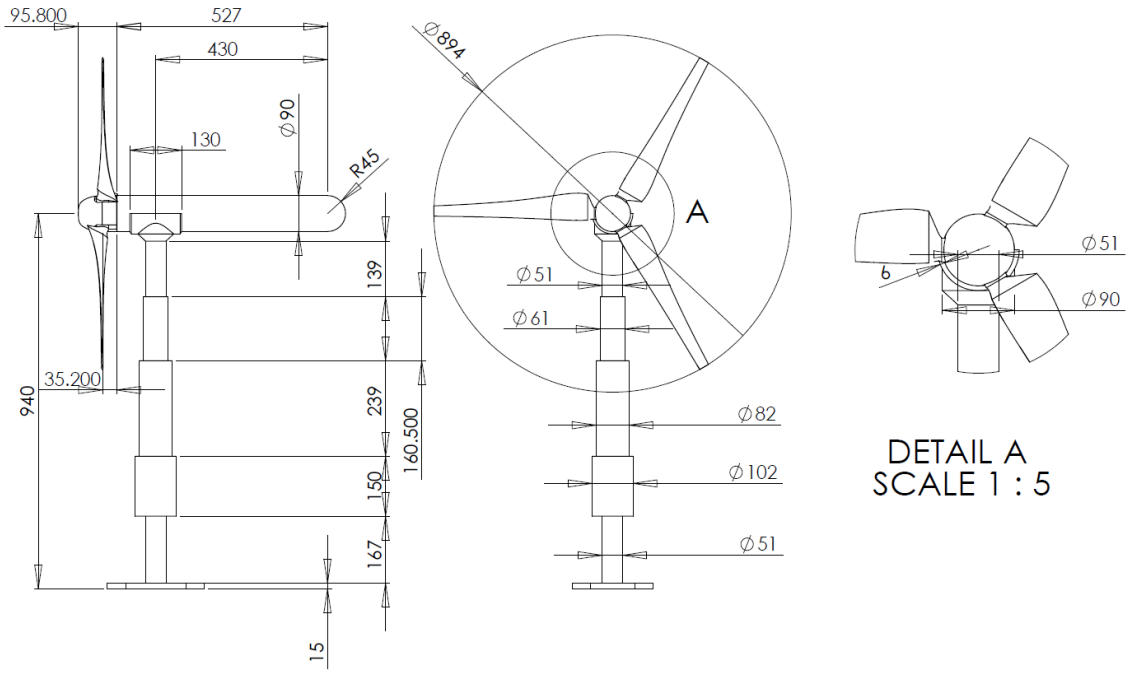

(b) Second turbine (T2) geometry

Figure 3.4: Turbines geometry

3.2.3 Rotor and blades design

During the blades design process the TSR was set to 6 and the nominal angle of attack to 7 ° for an undisturbed inlet velocity (U_∞) of 10 m/s. As it was designed to be a challenging test case the tip is sharply cut, to generate strong tip vortices, and the transition region between the cylindrical part and the innermost airfoil is a linear ramp. The chord length is bigger (≈ 3 times) than what is in a full scale wind turbine (considering a scaling factor of 1:100) in order to increase the Reynolds number in the model turbine; this aspect is also beneficial in terms of manufacturing the blade, permitting higher accuracy. This choice will give a smaller value for the aspect ratio, increasing three dimensional flow effects as well as the strength of tip and root vortices compared to an ideal chord distribution. All these factors will raise the difficulties as a test case for numerical modellers. The twist angle distribution is quite strong due to the high rotational speed at which it is supposed to operate to reproduce TSR= 6 (considering $U_\infty \approx 10$ m/s and its radius).

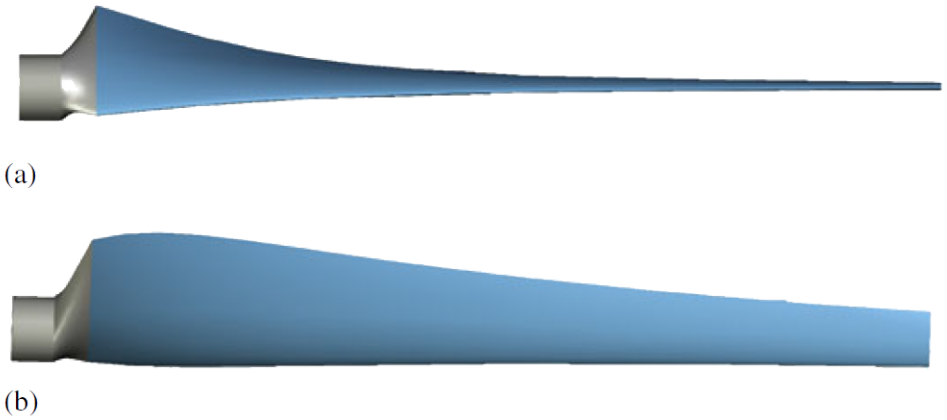

Figure 3.5: Model blade. (a) Azimuthal projection (b) Streamwise projection [8]

Scaling

Even if the present study is not thought to be scaled to a full scale turbine but to be compared with simulation of the same setup, the scaling issue is going to be briefly discussed to present a limitation of wind tunnel experiments.

The model turbines presents a geometry scaling factor of about 1:100 but the problem of scaling is much bigger when talking about wind generator as there are a lot of conditions to reproduce. The most important are:

- The TSR has to be matched with a full scale turbine.
- The Reynolds number at which the airfoil is working has to be reproduced.
- The inlet flow velocity should be the same.

Considering the same wind free stream velocity but a much smaller radius the TSR is reproduced increasing the rotational speed. This is a compromise as the high rotational speed induces 3D effects on the airfoil, improving its performances by delaying stall, that would not be present in a full scale turbine. The bigger problem is represented by the Reynolds number because it is much smaller in a model. The local Reynolds number based on the blade tip speed and tip chord is $Re_{c,tip} \approx 10^5$ while for a real one this parameter is at least one order of magnitude higher. In this case the airfoil is chosen to reduce the Reynolds dependency but it is always present and the effect on turbine performances will be further discussed in Section 4.2.1.

3.3 Instruments description

All instruments used during different sets of measurements are described in this section.

Barometer

The ambient pressure is acquired through a mercury barometer produced by Lambrecht. It consists in a mercury column calibrated in the unit of mmHg that has to be manually read. The instrument resolution is 0.1 mmHg.

Thermocouple

The temperature in the wind tunnel is constantly monitored through a thermocouple placed inside the test section, in order to take into account air density variations due to temperature changes. It is also used during hot wire measurements for temperature correction.

The thermocouple is a K type (Chromel/Alumel). The analogue voltage from the thermocouple is sent to a National Instruments NI 9211 thermocouple board and converted into temperature.

Differential manometer

A differential manual manometer is used, after being tilted it has a resolution of 1 Pa. The manometer is calibrated so that from the alcohol column is possible to directly read the differential pressure in Pa. It was used to check all pressure transducers calibration factors before starting each measurement campaign.

Pressure transducer

Two in-house assembled pressure transducers are used. Both of them have a pressure capacity range of 10 inches of water ($\approx$ 2200 Pa), covering all the measurements range.

For the calibration of the instrument refers to Section 3.4.

Static Pitot probe

A Pitot probe is installed inside the test section to calculate the velocity of the flow. The pressure difference (between the static pressure and dynamic one) is measured thanks to a pressure transducer (see section 3.3) and then converted into velocity of the flow through Equation 3.1, derived from Bernoulli's Equation.

$$U_{\infty,pitot} = \sqrt{\frac{2 \times (p_{tot} - p_{stat})}{\rho}} \tag{3.1}$$

This instrument measures the velocity of the flow in the position in which is installed. Pitot probe has a low frequency response (compared to the frequency of turbulent events) so it is not suitable for measurements in a turbulent flow. In case of high turbulence, also the velocity mean value measured by the Pitot probe can be affected and it is needed to be corrected by the α factor as in Equation 3.2 [35]. To avoid a decrease in accuracy because the α factor is dependent by turbulence length scale, the Pitot probe is not used as reference when turbulence intensity is significant, instead the inlet nozzle pressure difference is considered.

$$U_{\infty,pitot} = \sqrt{\frac{2 \times (p_{tot} - p_{stat})}{\rho} - \alpha \cdot \overline{(u')^2}} \tag{3.2}$$

Inlet nozzle

Before entering the test section air is passing through a contraction (Figure 3.1), which is used as a nozzle to measure the inlet velocity.

Pressure taps are distributed over the biggest and the smallest section perimeters, allowing to record a differential pressure between them. Measuring the differential pressure between p_1 and p_2 (respectively pressure in the first position and in the second) and knowing the area ratio between A_1 and A_2, from Bernoulli equation it is possible to calculate the bulk velocity as in Equation 3.4.

$$\frac{A_2}{A_1} = \frac{1}{4.36} \tag{3.3}$$

$$U_{\infty,bulk} = \sqrt{\frac{2(p_1 - p_2)}{\rho\left(1 - \left(\frac{A_2}{A_1}\right)^2\right)}} \tag{3.4}$$

This instrument is used to calculate the reference velocity when measurements with a GRID at the inlet test section are performed. The grid is positioned after the second set of holes. For taking into account the pressure drops of the contraction itself and on the downstream GRID an empirical correction factor is found (see Section 3.8). The reference velocity will be calculated as in Equation 3.5.

$$U_\infty = U_{\infty,bulk} \times 0.84 \tag{3.5}$$

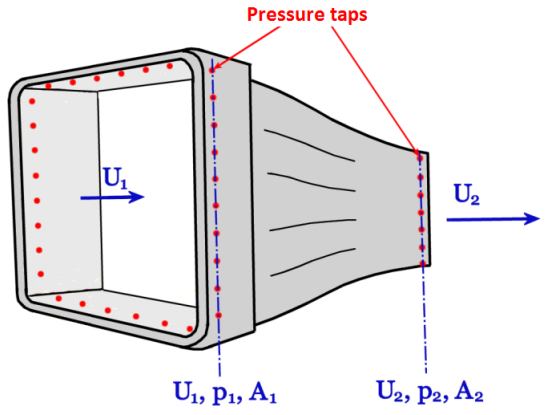

Figure 3.6: Sketch of the inlet nozzle.

Hot wire anemometer

The instrument operation principle is to obtain the flow velocity by evaluating the convective heat transfer from an heated wire to the cold fluid. A single hot wire probe is shown in Figure 3.7, the sensor consists of a very thin tungsten wire (length ≈3 mm and diameter of 5 μm) connected with two prongs. An electronic circuit (CTA: constant temperature anemometer) heats the wire up and keeps constant its temperature by regulating the supplied current in a proportional way to the velocity change; a correlation between these two variables can be found.

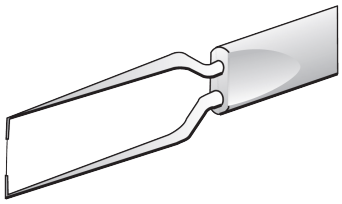

Figure 3.7: Hot wire probe [9]

The main features of this instrument that makes it suitable for these experiments are its high temporal and spatial resolution: it can measure fluctuations of very high frequency and eddies down to the order of mm*s*. For these reasons it is used for measuring the velocity and the turbulence intensity in the wake of the turbine and in all situations with a high turbulence intensity.

The instrument functioning is described more in details. The measuring chain is sketched in Figure 3.8. The probe is installed in the tunnel where the velocity has to be measured, then it is connected to the Anemometer in which a CTA circuit and a signal conditioner are present. The signal, after being conditioned, is connected to the A/D Board for being digitally converted and acquired by a computer.

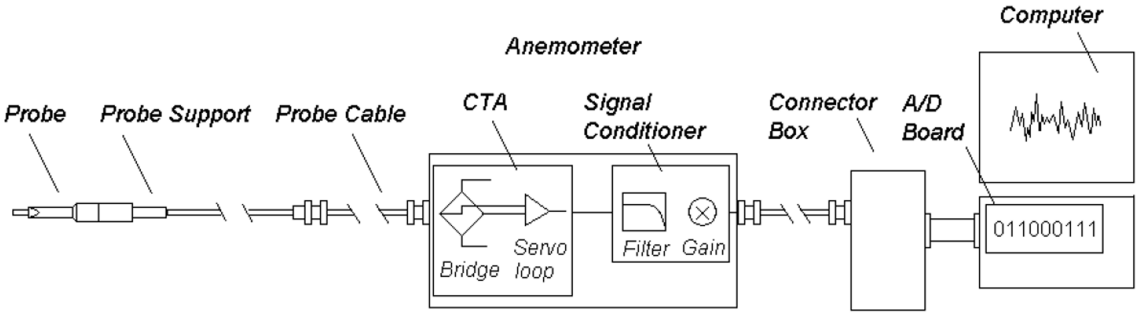

Figure 3.8: Typical constant temperature anemometer (CTA) measuring chain [9]

The probe used during the measurements is made up of a single wire and it is positioned so that

the streamwise component (mean velocity and fluctuations) could be measured. The CTA circuit contains a Wheatstone bridge as depicted in Figure 3.9. R_w is the hot wire probe resistance, which is connected to one arm of the bridge. The wire is heated up exploiting Joule's effect. When the quantity of heat loss varies, due to the flow velocity variations, more current has to be supplied by the circuit, in order to keep the wire temperature constant.

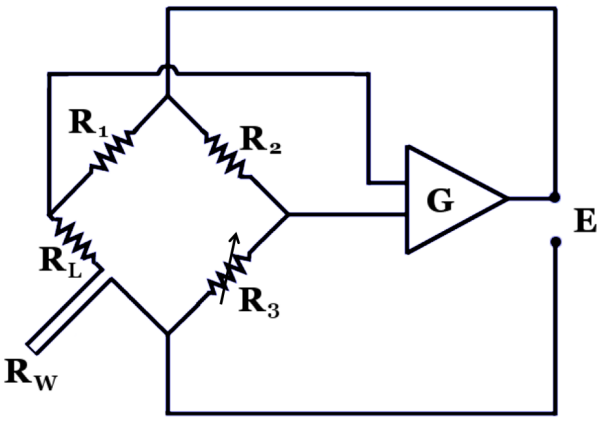

Figure 3.9: Wheatstone bridge of constant temperature anemometer

The system voltage output is amplified by an operational amplifier (G), so it is used as a feedback to maintain the wire temperature constant [36]. The result is that the voltage difference E represents the heat transfer so that the flow velocity can be evaluated. The wire temperature can be chosen varying the resistance R_3 in the circuit.

The high gain of the servo loop amplifier, combined with the sensor low thermal inertia, give a very high frequency response. The effective frequency that could be detected by the equipment installed is always tested as described in Section 3.4.

The main issues connected with hot wires probes are related to directional and flow temperature sensitivity.

The instrument is sensitive both to flow velocity and direction; using a single wire, as in our case, only one velocity component can be detected. It has to be considered the three dimensional flow can affect the measure of the streamwise velocity. Considering the implicit three-dimensionality of the flow field in a wake of a wind turbine it has already been tested using LDV technique [14] the influence of other flow directions in the measurements and it results that they are included in the accuracy range of the hot wire (see Section 3.9).

The second problem regarding hot wire measurements is connected to its temperature sensitivity. Changing the temperature at which the flow is investing the wire the bridge voltage E will change for the same setted velocity. "A 1K change gives an error of approx. 2% in velocity" [9].

During data analysis this limit can be reduced using a temperature correction for the voltage, for this reason the temperature in the tunnel is always monitored via a thermocouple placed close to the hot wire.

For the calibration of the instrument refers to Section 3.4.

Torque transducer

Inside both turbines nacelles a torque transducer HBM® T20WN is installed (see Figure 3.10)

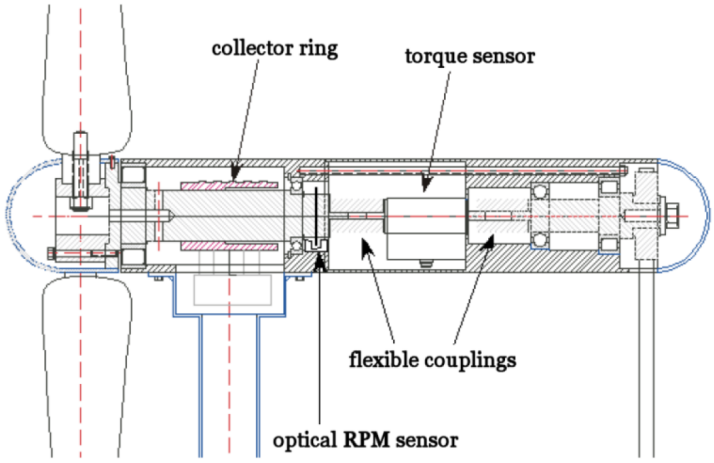

Figure 3.10: Cross section of T2 nacelle.

The nominal maximum torque that can be measured is ±5 Nm for T1 and ±2 Nm for T2. It is converted into a signal of ±10 V in both cases, so the calibration coefficients are respectively 0.5 Nm/V and 0.2 Nm/V. The characteristic tolerance of the instrument is ±0.2% of the voltage measured and the output signal for a zero torque is ±0.2 V.

RPM sensor

The two model wind turbines are also equipped with an optical RPM sensor inside the hub casing (see Figure 3.10). A metallic disc with a small hole is fixed to the rotor axis, peaks in voltage are registered by the sensor for each blade rotation and send to the NI®acquisition system. The time between two peaks is measured and averaged over the whole acquisition period, obtaining the RPM value.

Aerodynamic balance

A six-component force balance, produced by Carl Schenck AG, is mounted below the tunnel floor. A turbine is mounted on the balance and the thrust force is measured. During this thesis project no yaw misalignment is tested, so just the force in the axial direction is acquired.

3.4 Instruments calibration

Pressure transducer calibration

Before performing each set of measurements, the calibration coefficient of the two pressure transducers are checked using a manual manometer (see section 3.3). For the calibration procedure the manual manometer and the pressure transducer are connected in parallel. Different inputs are given and always both the alcohol column [Pa] and the voltage [V] are acquired. Figure 3.11 shows an example of the calibration curve found for one of the pressure transducers. All pressure transducers used during measurements are checked many times during the whole experimental period.

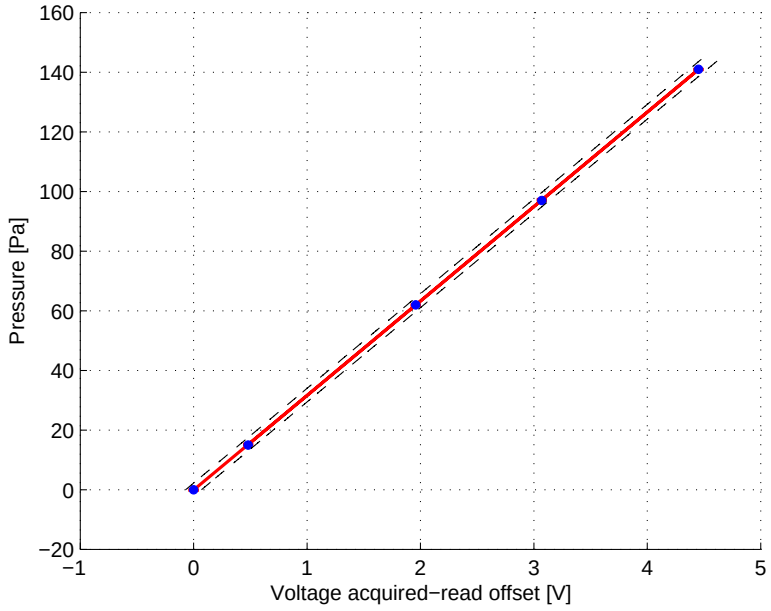

Figure 3.11: Typical pressure transducer calibration curve.

Hot wire calibration

The probe is calibrated against a standard Pitot tube, positioned 50 mm on one side, in free stream condition. Before every measurement session calibration procedure is executed. A 4^{th} order polynomial is used to fit the calibration curve, relating the acquired voltage to the measured Pitot velocity. The anemometer output is corrected for temperature variations before calculating the regression curve. A typical calibration curve is plotted in Figure 3.12. The RMS of the deviation of the measured points from the regression curve is calculated and always results in a magnitude order of 10^{-3}. The temperature correction is performed by a in-house programmed MATLAB® routine.

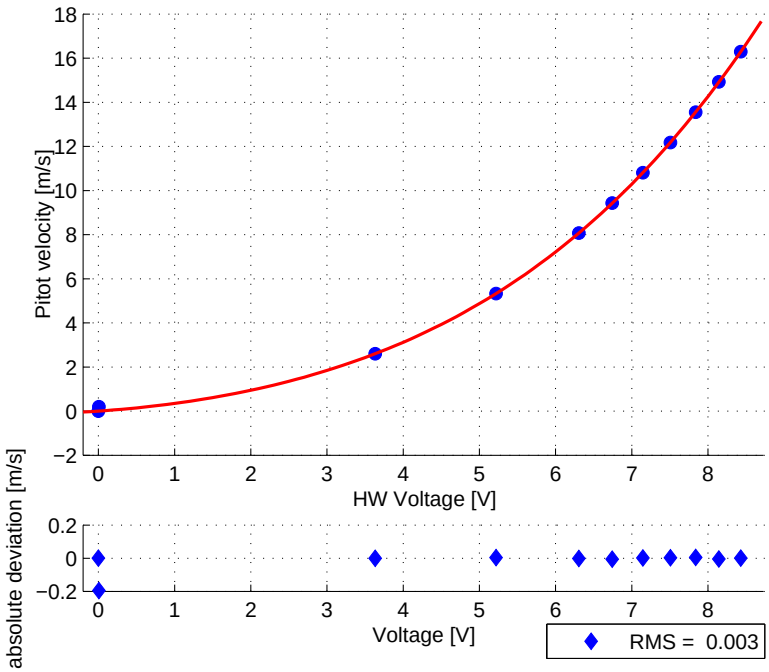

Figure 3.12: Typical Hot Wire calibration curve.

A square wave test (according to [9]) is performed to check the frequency response and it always results in values no lower that 10 kHz. As it is considered an upper limit, the highest acquisition frequency is always 5 kHz (half of the square wave test not to add accuracy uncertainties as suggested in [9]).

Torque sensor calibration

Both torque sensors calibration coefficients are checked before each set of measurements, here it will just be reported an exemplary process of calibration curve testing.

The rear part of the shaft is blocked and a constant torque on the front part is exerted putting a reference weight at a fixed distance from the centre. This process is repeated varying the weights and the voltage is acquired. The linear dependency between the torque [Nm] and the voltage [V] is found so the calibration coefficient and its tolerance checked. In Figure 3.13 an example is shown. The blue dots are the acquired points. The red line is the evaluation of the linear regression and error bars represent the deviation of the measurement points from the regression line. The black dashed lines are the limit of accuracy of the instrument. As all points are inside the area between the black dashed lines, the instrument calibration is verified.

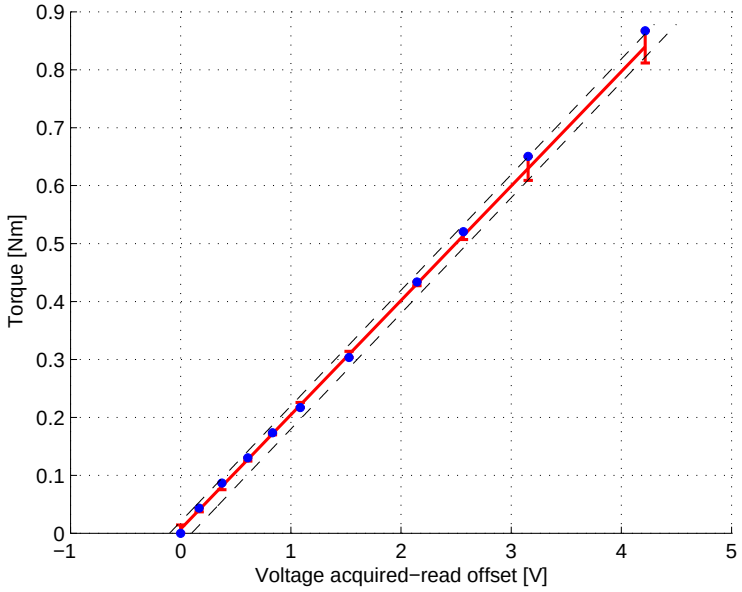

Figure 3.13: Typical torque transducer calibration curve.

Aerodynamic balance calibration

The process of calibration is similar to one of the torque sensor, defined weights are putted onto an hanging device, creating note force values. A linear dependency is found by regression of acquired data. Figure 3.14 shows the calibration regression line.

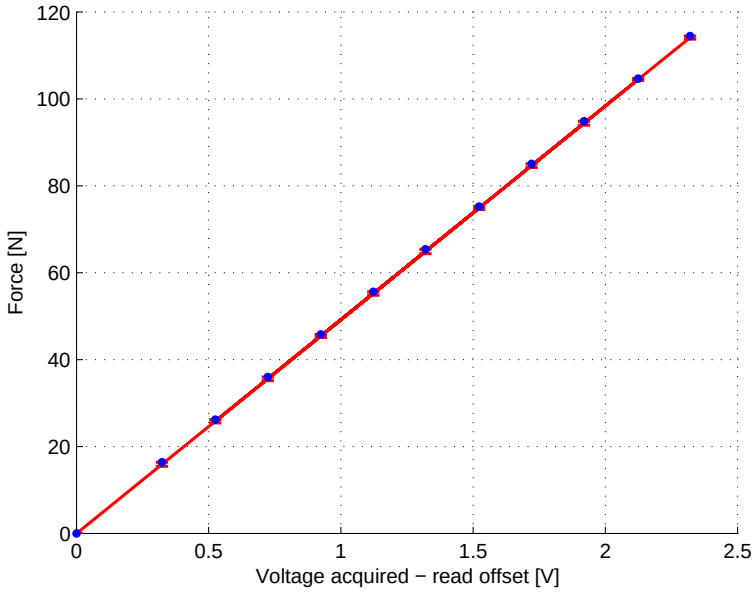

Figure 3.14: Typical aerodynamic balance calibration curve.

3.5 Data acquisition and Control systems

The data acquisition system (DAQ) used during experiments is a NATIONAL INSTRUMENTS ®NI 9215 data acquisition board. The analog signals are treated by amplifiers circuits before acquisition, in order to reduce the discretization errors. The acquisition and control software is programmed in LabVIEW®, the interface unable both a real time signal monitoring as well as an acquisition window, which make it possible to save data into ASCII-formatted text files.

For each set of measurements the acquisition frequency and the number of samples could be set. For performances measurements the sampling frequency is set to 2 000 Hz and the number of samples to 60 000, resulting in a 30 s sampling time.

When sampling the signal for hot wire measurements an higher frequency is used. A low pass filter setted at 2 500 Hz is applied and then the signal is sampled at 5 000 Hz. A sampling time of 40s lead to collect 200 000 samples. These conditions allow spectra analysis respecting Shannon-Nyquist sampling theorem [37]. During hot wire measurements time series of all points are recorded in order to be able to reconstruct the signal with all its turbulent fluctuations properly.

3.6 Measurement campaign

For the thesis purpose two different classes of measurements are performed: wind turbine performances curves and wake assessments. Various settings are tested.

Firstly a characterization of the inlet flow field in two different configurations (low and high turbulence background level) is performed using a Pitot tube and a hot wire probe. For the empty tunnel it must be ensured a uniform mean velocity profile and a low turbulence background level on the future rotor swept area. The expansion of the boundary layer along the tunnel is investigated too. When mounting the grid (described in Section 4.1.2) the turbulence level on the rotor plane and the decay along the tunnel is analysed, as well as the uniformity of the flow velocity. In both cases a power spectral density analysis is performed for testing the flow frequency regularity.

Thereafter, C_P and C_T curves are measured independently for both model turbines for a number of different wind tunnel inlet speeds (U_∞) in both inflow configurations. All experiments are taken with the single turbine at 2D from the inlet test section. Fixed U_∞, thrust and torque on the shaft are recorded ranging the tip speed ratio (indeed the rotational velocity) from $\lambda = 1$ to the runaway point. The main reasons are having working reference points for further comparisons and ensuring regular operating features of wind turbine blades. Wake measurements on a horizontal line at hub height behind turbine T1 are performed at three axial stations (3D, 5D and 9D) downstream the turbine, for different TSR. The goal is to have an overview of the inlet flow conditions for the second turbine

Subsequently both wind turbines are installed in the tunnel and the parametric study of power output and thrust is carried out. The first wind turbine is fixed below the wind tunnel floor on a support at 2D from the inlet, while the second turbine is positioned over the aerodynamic balance, to allow thrust measurements, in three different axial stations: 3D, 5D and 9D from the first rotor plane. All experiments are repeated for the two different flow conditions: low and high turbulence. In each configuration a matrix ranging the tip speed ratios of both turbines is made.

3.7 Data processing

Evaluation of Power ant Thrust curves

The performances of a wind turbine are usually described in terms of power and thrust curves (for details refer to Section 2.4). The torque on the shaft T and the thrust force F_T are measured together with the reference inflow velocity U_∞ and the rotational speed ω. The power generated by the turbine can be calculated as: $Power = \omega T$. Then the tip speed ratio λ, C_P and C_T can be derived using respectively Equations 2.1, 2.3 and 2.4 to obtain the performances curves.

Evaluation of flow measurements

The flow field is measured using the hot wire probe, when the evaluation of velocity deficit and turbulence intensity is required.

The velocity deficit is defined as the ratio between the mean velocity in a defined position $\overline{U}$ and the freestream reference velocity U_∞ as in Equation 3.6. It results to be a non-dimensional parameter [-] describing the momentum loss in the wake.

$$Velocity\ deficit = \frac{\overline{U}}{U_\infty} \tag{3.6}$$

The reference velocity is calculated according to Section 3.8, while the mean velocity is obtained averaging the N instantaneous values recorded U_i as in Equation 3.7.

$$\overline{U} = \frac{1}{N}\sum_{i=1}^{N} U_i \tag{3.7}$$

When calculating the velocity from hot wire output voltage a temperature correction is necessary as the bridge voltage E is very sensitive to fluid temperature. "A 1 K change gives an error of approx. 2% in velocity" [9]. Before converting the acquired voltage E into velocity, a correction factor is applied according to [9], so that the corrected voltage E_{corr} is calculated. The temperature changes in air never exceeds the suggested range of ±5 °C.

$$E_{corr} = \left(\frac{T_w - T_0}{T_w - T_a}\right)^{0.5} \cdot E \tag{3.8}$$

The turbulence that the rotor promoted on the flow requires a statistical analysis of the signal

acquired from the hot wire because of its random nature. Figure 3.15 shows an example of a recorded velocity signal $U(t)$ in a turbulent flow.

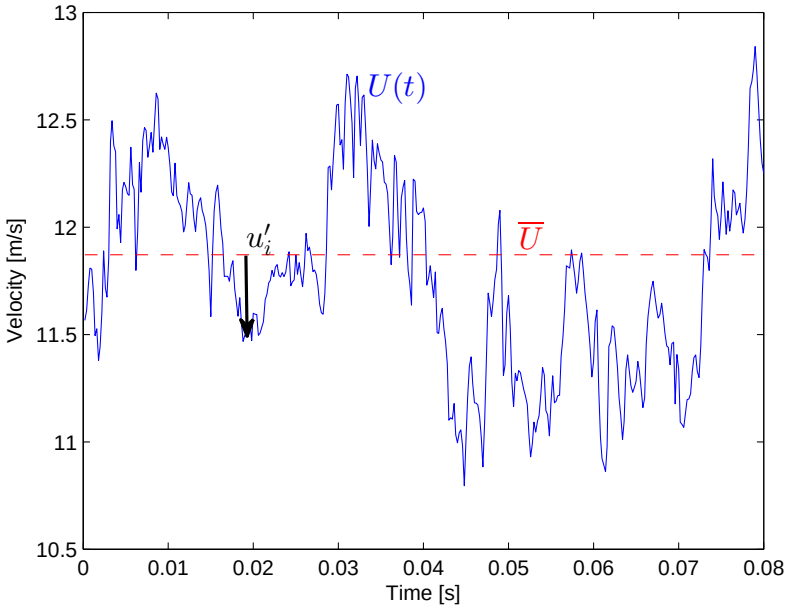

Figure 3.15: Example of an acquired velocity signal in a turbulent flow.

The actual velocity U_i can be split up into 2 parts: the local mean velocity $\overline{U}$ and the fluctuation u_i':

$$U_i = \overline{U} + u_i' \tag{3.9}$$

The turbulent fluctuation u' is defined as the standard deviation of velocity (statistical second order moment) as in Equation:

$$u' = \sqrt{\frac{1}{N-1}\sum_{i=1}^{N}(U_i - \overline{U})^2} = \sqrt{\frac{1}{N-1}\sum_{i=1}^{N}(u_i')^2} \tag{3.10}$$

Therefore the turbulence intensity TI [%] can be calculated as the ratio of the turbulent fluctuation u' and the local mean velocity $\overline{U}$:

$$TI[\%] = \frac{u'}{\overline{U}} * 100 \tag{3.11}$$

As already mentioned, spectral analysis provides information about how the energy is distributed with respect to frequency. In latter analysis the power spectral density is calculated using the discrete Fourier transformed, windowed with a Hann function. A window length of 3 125 samples,

with an overlap of 1 500 (≈ 50%) is used as a compromise between quality of results, calculation efficiency and smoothness of the signal. It results in a frequency resolution of 1.6 Hz. Figure 3.16 shows the comparison between a full DFT calculation (Discrete Fourier Transformed) and two overlapping methods of a signal recorded in the turbine T1 wake.

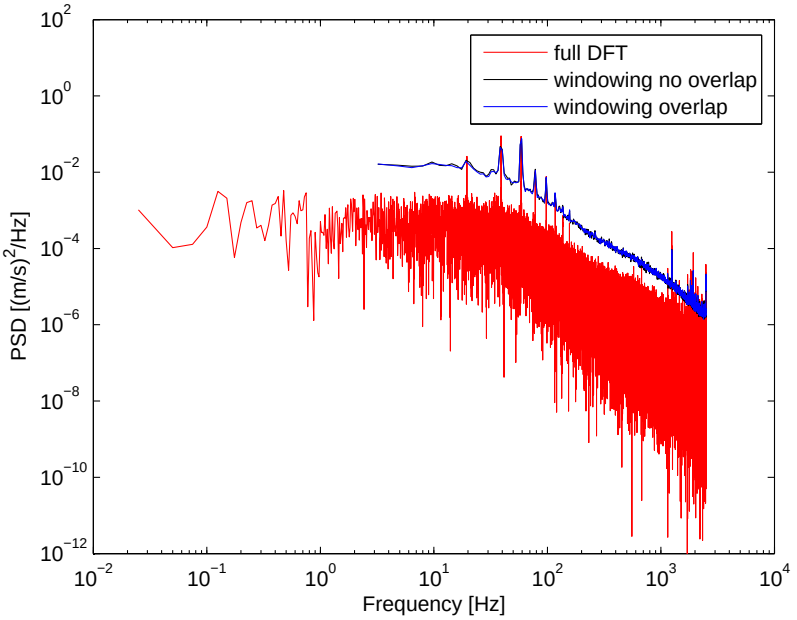

Figure 3.16: Comparison between three different methods of power spectral density calculation.

3.8 Reference velocity

The reference velocity has to be chosen and clearly described in order to have a set of measurements that could be compared with numerical tests. It is decided to consider two different instruments as reference in the two incoming flow conditions. When the tunnel is empty a Pitot probe is used, while when the grid is mounted the inlet nozzle is preferred because of its characteristics.

During experiments in the empty tunnel, the reference position of the Pitot probe has to be chosen. The reference velocity should not be affected both by the turbine induction and by wind tunnel walls, as it is supposed to be the undisturbed inflow velocity. Different velocity measurements are taken in all the positions marked in the sketch in Figure 3.17 while the turbine is running. The reference position is taken as a compromise between avoiding the influence of the wind tunnel walls and the turbine induction. After considering the results and the accuracy of the instrument, the position marked with the big red circle is chosen. It is located at the same height of the turbine hub.

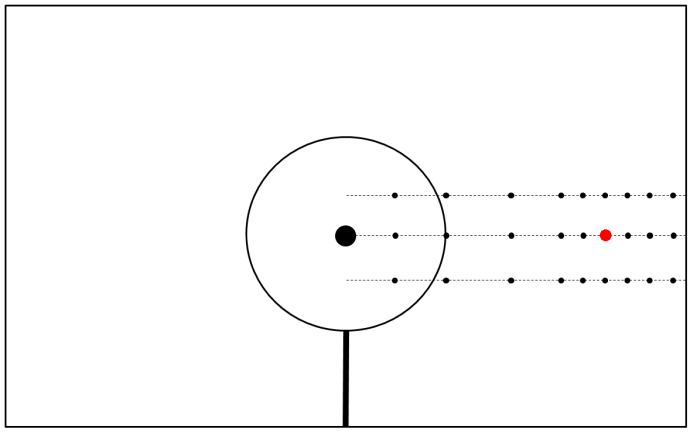

Figure 3.17: Position of the reference Pitot probe: front view of wind tunnel section.

When running experiments with the grid, due to the high turbulence induced, the inlet contraction system is used to set the reference velocity. Anyway, because of its characteristic (see 3.3) an experimental correction factor has to be applied, taking into account for pressure losses over the grid.

Several velocity measurements are taken both in a vertical line in the centre of the tunnel and in a horizontal line at the hub height using hot wire anemometer. Also the velocity from the contraction is registered. By the average of these results the experimental correction factor is found to be 0.84 for an incoming flow of roughly 11.5 m/s.

3.9 Measurement accuracy

The accuracy of the whole measurement chain is calculated according to [37]. The calibration accuracy of instruments is taken into account considering a 95% confidence interval. The total uncertainties is obtained via the RSS (root of the sum of the square) method and combined via the formula [38]:

$$\omega_R = \left(\sum_{i=1}^{n} \left[\omega_{x_i} \frac{\partial R}{\partial x_i} \right]^2 \right) \tag{3.12}$$

where R is the variable, function of the parameters x_i. Therefore the accuracy of the resulting reference velocity, thrust, torque and hot wire velocity can be estimated.

The air density is corrected for ambient pressure at the beginning of each experiment, but the error induced on the results is considered negligible. The air humidity is not taking into account. The main issue could be on hot wire heat transfer, however, according to [9], the influence is very small and thereby negligible.

The reference flow velocity measured with the Pitot probe (U_∞ = 11.5 m/s) results in an accuracy of ±0.1 m/s, i.e. ±1%, while with contraction nozzle (not considering the effect of the empirical correction factor) it is almost double.

As regards the power curves for both turbines, an example is depicted in Figure 3.18. None of the measurements exceed a relative error of ±5% if the runaway point is not considered. The accuracy in tip speed ratio calculation is considered negligible and it is not inserted in the graph as never overtake ±0.5%.

With respect to free stream and wake flow measurements using the hot wire probe, it should be noticed that there are several factors affecting the measurement chain: the probe itself, its installation and calibration, the anemometer circuit and the data acquisition board. There is the possibility of misalignment of the probe with respect to the velocity component that is going to be measured. This source of error is considered negligible as it is not moved between the calibration procedure and the measurements. Drift and noise from the CTA anemometer is ignored too as all the experiments were conducted during a short period of time just after calibration. Post-calibrations are also conduced and data are evaluated using the two polynomial curves. Data exceeding an arbitrary velocity difference of ±0.1 m/s, using the two calibration coefficients, are disregarded. The digital conversion of the analog voltage output can be a source of error, but the influence onto the overall measurement uncertainty is estimated to be very small [9] if an appropriate data acquisition board is used. The chosen sampling frequency and the analogical low-pass filter help on reducing this source of error. According to literature (e.g. [9]), one of the most important source of error in hot wire measurements is the temperature variation in the

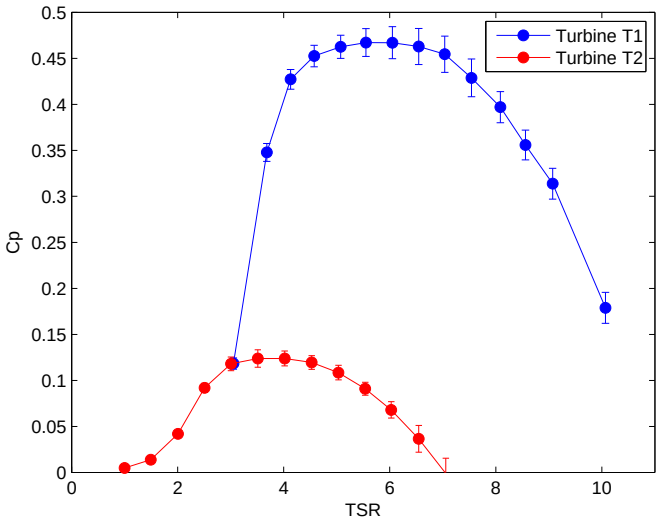

Figure 3.18: Power coefficient curves for the two turbine models running with a downstream separation distance of 3D. The second turbine curve is obtained with the first turbine running at optimum TSR. The errorbars represent the evaluated accuracy.

flow. In this project the signal is temperature-corrected as already described in Section 3.7 so that no additional uncertainties are introduced.

The main source of error for hot wire measurements is assumed to be originated during the calibration process: the hot wire is calibrated against a Pitot tube, connected to a pressure transducer. The pressure transducer calibration is performed using a manual manometer. So the flow velocity depends on a manual reading of an alcohol column. Each of these steps is evaluated and results in a velocity accuracy that never exceeds ± 0.2 m/s, while for turbulence intensity an error estimation of $\pm 0.1\%$ is obtained.

In other studies [14], wake measurements using a single hot wire probe are compared with two-component Laser Doppler Velocimetry showing good agreement. So the tridimensionality intrinsic in a turbine wake does not strongly affects single hot wire measurements.

Chapter 4

Results and discussion

In the present chapter the results of major interest are presented: first the characteristics of the inlet flow are described, then a single turbine is characterized, both in terms of performances and wake to allow comparison with the power output parameter study, presented in the third section.

4.1 Inlet Flow Field characterization

Initially, the flow field in the test section is scanned. A complete characterization of the flow in the wind tunnel has to be accomplished, in order to analyse wind turbine performances and wakes, moreover to supply to numerical modellers the inflow conditions.

In order to check the main features of the flow at the reference wind speed (U_{ref} = 11.5 m/s) some tests are taken. Other studies have been performed before in NTNU wind tunnel, but at different wind speeds [14].

For the present study two inflow conditions are considered: the empty tunnel (low background turbulence) and the flow after a meshed grid (high background turbulence).

4.1.1 Empty tunnel

In the empty tunnel configuration the flow is characterized. In order to check the boundary layer expansion, the velocity is measured at the vertical centreline of the tunnel at different stations along the tunnel. The incoming flow velocity is set at 11.5 m/s at the future hub height $z/R = 0$. This is the reference value used for presenting the results in a dimensionless shape. In Figure 4.1

the outcomes are depicted. The different downstream positions are measured from the inlet test section and the diameter of the first turbine ($D_1 = 900mm$) is used as reference.

The boundary layer growth on the floor is visible along the tunnel.

It has to be underlined that the boundary layer expansion does not affect the measurements as at 7D from the inlet, the flow facing the rotor plane ($-1 < y/R < 1$) is still uniform. In the area where the rotor will be positioned the results spread is confined in the range of $\pm 1\%$. So the flow in the wind tunnel will be considered uniform over the rotor swept area.

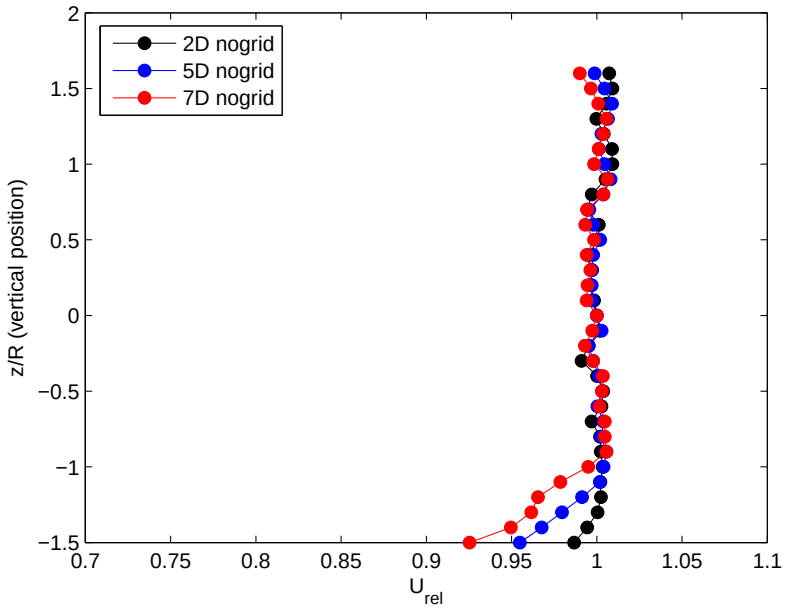

Figure 4.1: Flow mean velocity profiles in the empty tunnel, measured at different downstream positions (2D, 5D and 7D from the inlet), in the vertical centreline. Non-dimensional values are obtained using the value measured at the wind tunnel centre.

At 2D from the inlet, where the first turbine is standing, more tests are carried out (see Section 4.1.3).

The streamwise component of the turbulence intensity (u'/U_m), at 2D downstream from the inlet test section, is measured in an horizontal line at the future hub height. The maximum value recorded is 0.5%. Previous measurements have shown a turbulence level of 0.3% [34, 14] and 1% [5]. Despite the small spread in results, all these measurements present very low turbulence levels as expected in a wind tunnel.

4.1.2 Grid

In order to increase the turbulence level in the tunnel a mesh grid is installed at the test section inlet. A grid is used to obtain a good approximation of decaying homogeneous turbulence [39]. The interest in analysing performances and wakes in a different inflow condition comes from the significance of including turbulence effects in the experimental dataset.

The grid mesh size is $M = 0.240$ m and the mesh shape is depicted in Figure 4.2.

Figure 4.2: Mesh grid installed at the inlet test section. The turbine is not installed during these measurements

Passing through the grid, the turbulent kinetic energy (TKE) increases; as there are no turbulence sources along the tunnel, the TKE decays moving far from the grid. The measured turbulence intensity distribution is shown in Figure 4.3. So the mean turbulence intensity and its deviation are derived:

- At 2D from the grid (future turbine location) it is found $(10 \pm 0.3)\%$.
- At 5D it is $(5.2 \pm 0.4)\%$.
- At 7D it is $(4.4 \pm 0.4)\%$.

These mean values are in good agreement with the turbulence decay law after a grid in a wind tunnel [39].

The mean velocity is not totally independent on the spanwise coordinates. As depicted in Figure 4.4, at the three different downstream positions the flow seems to accelerate both at the top

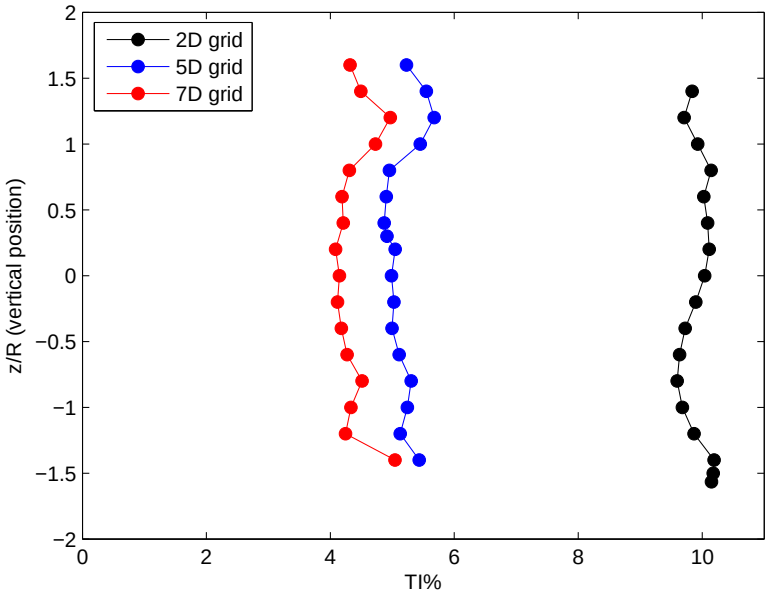

Figure 4.3: Turbulence intensity [%] in the flow after the grid at different downstream positions (2D, 5D and 7D from the inlet), measured in the vertical centreline of the tunnel.

and at the bottom of the tunnel. Nevertheless considering the future rotor position ($-1 < z/R < 1$) the flow can be considered uniform with a deviation from the centre line that never exceeds $\pm 0.2\%$.

4.1.3 Flows comparison at 2D from the inlet

After the first analysis of the flow along the tunnel is completed, it is decided to deeper investigate the flow characteristics at 2D from the inlet, where the first turbine will be installed. In this position, a turbulence intensity and mean velocity scans are accomplished at the same height where the turbine hub will be placed.

The mean velocity is adimensionalized with the value obtained at the tunnel centreline ($y/R = 0$). In Figure 4.5 the two different inflow conditions are compared.

Considering the empty tunnel a slight increase can be pointed out for $y/R > 0.5$, however it is found to be smaller than 5%, so it is not considered affecting the measurements significantly. In the range $-1 < z/R < 0.5$, the velocity is uniform within $\pm 0.5\%$. The results are in good agreement with previous tests, for example in [8] the flow uniformity across the test section was $\pm 0.27\%$.

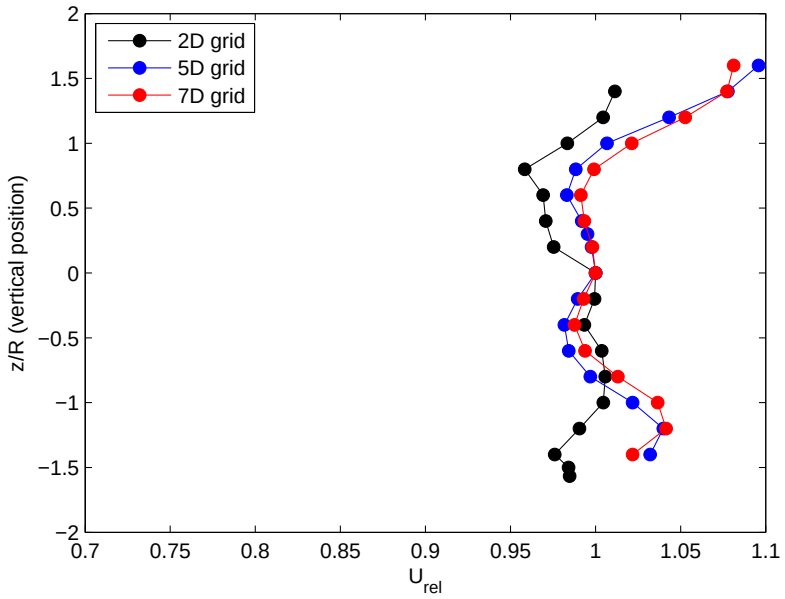

Figure 4.4: Flow mean velocity profiles after the grid, measured at different downstream positions (2D, 5D and 7D from the inlet), in the vertical centreline of the tunnel. Non-dimensional values are obtained using the value measured at the wind tunnel centre.

Regarding the flow after the grid, a stronger variation for the mean velocity depending on the spanwise coordinates is noticeable. At 1.8 m far from the grid, the stream has not totally recovered and flattened. Nevertheless the deviation from the mean value does not exceed ±4%, so it is considered acceptable for the following measurements.

4.1.4 Power Spectral Density

The spectrum of the incoming flow is analysed, determining how the turbulent kinetic energy is distributed among the eddies of different sizes.

During the set of measurements formerly described, the velocity is acquired and recorded as time series from the hot wire. In post-processing, a spectrum analysis is performed to check the incoming flow regularity in frequency. For each point, the Power Spectral Density is calculated implementing the discrete Fourier transformed in a MATLAB®script.

A turbulence spectrum, for each point of the 2D horizontal velocity scan, is elaborated for the empty tunnel configuration. In Figure 4.6, three particular spectra, at y/R = 0;1.5;1, are represented; moreover the average of the 25 spectra is plotted ("mean spectrum"). The spectrum does not vary significantly in different positions of the test section and does not present peaks

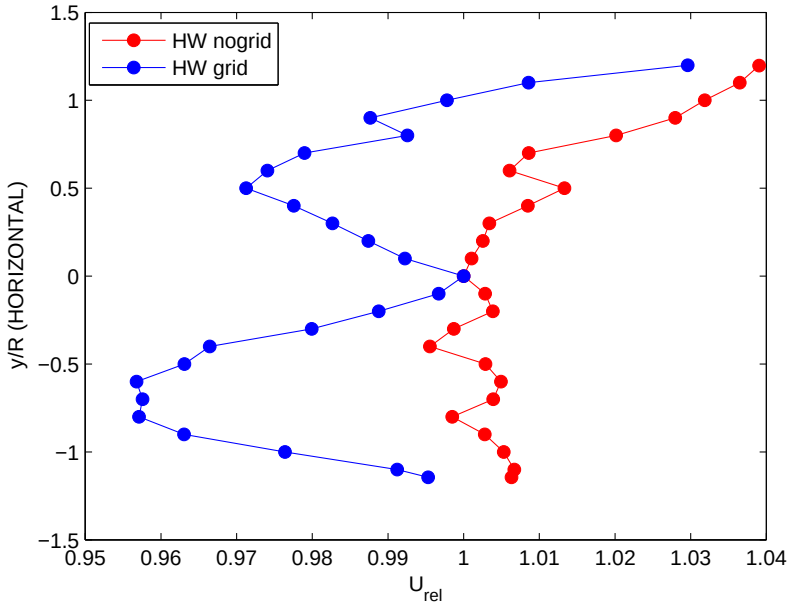

Figure 4.5: Flow mean velocity profiles, measured at 2D from the inlet, on a horizontal line, at future hub height. Comparison between the 2 different incoming flows. Non-dimensional values are obtained using the value measured at the wind tunnel centre.

for particular frequencies, as expected.

The same analysis is performed with the grid positioned at the test section inlet and the resulting spectra in Figure 4.7 are obtained. No variations are recorded varying the location of the measurement point. Furthermore the turbulence does not present peaks in frequency, meaning that after 2D, time and length scale of the grid typical eddies have been dissipated. It means that after 2D, time and length scale of the grid typical eddies have been dissipated and the turbulence in the flow does not present peaks in frequency peculiar frequencies of the grid

The black dotted line (in Figure 4.6 and 4.7) represents the Kolmogorov "$-5/3$" spectrum. It is the trend of the energy cascade in the inertial subrange. In the grid case (Figure 4.7) between 10^2 and 10^3 Hz, the tendency perfectly match the theory.

It has to be underlined that the magnitude of the PSD in the grid configuration is double with respect to the empty tunnel case. This is the effect of higher turbulence level introduced by the grid.

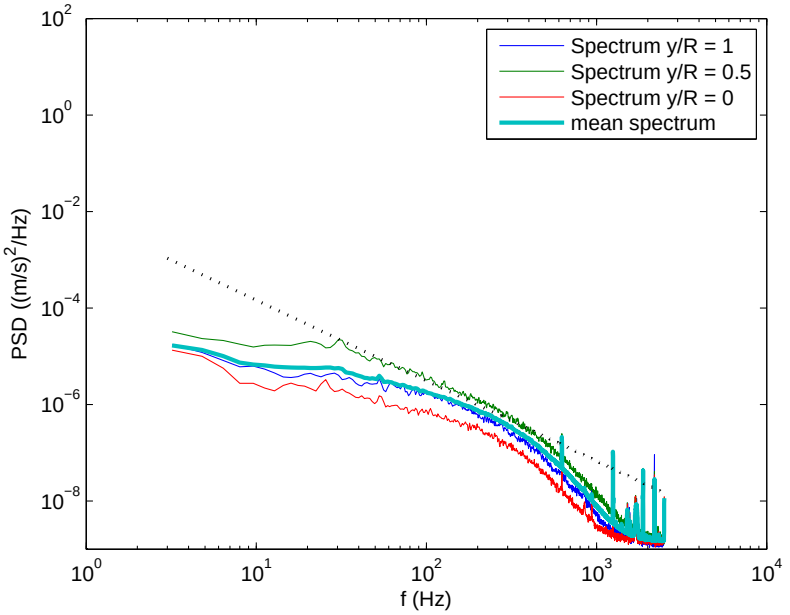

Figure 4.6: Power Spectral Density of the flow in the empty tunnel.

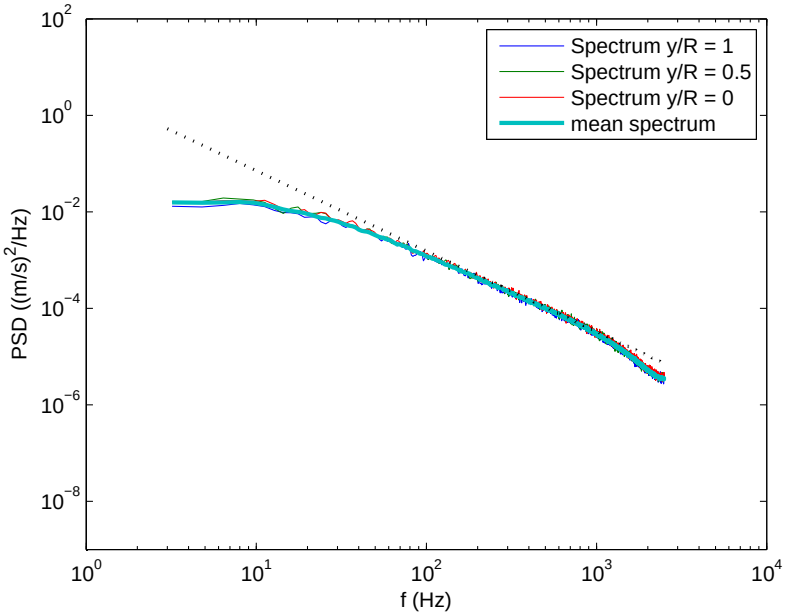

Figure 4.7: Power Spectral Density of the flow in the tunnel after the grid.

4.2 Single turbine

Several studies of performances and wakes behind a single turbine have been performed in previous projects at NTNU [8, 14, 32] However, in the present work, some boundary conditions are different, as incoming flow characteristics and reference velocity. For this reason and for having a term of comparison when analysing an array of two wind turbines, some basic performance and wake experiments are carried out.

The different models (T1 and T2) are tested for performances in two different incoming flow conditions: low and high background turbulence levels. Afterwards, wake measurements in an horizontal line are performed behind T1 in order to define the incoming flow experienced by the second turbine.

The experiments are carried out with a single turbine standing alone in the tunnel, at 2D from the inlet on the aerodynamic balance. The turbine is located in the centre of the tunnel section, the hub centreline is at (826 ± 1) mm of height. All the dimensions are reported in Figure 4.8. The downstream positions represent the distances at which the horizontal line scanning of the wake is performed, defining the locations of the future second turbine of the array.

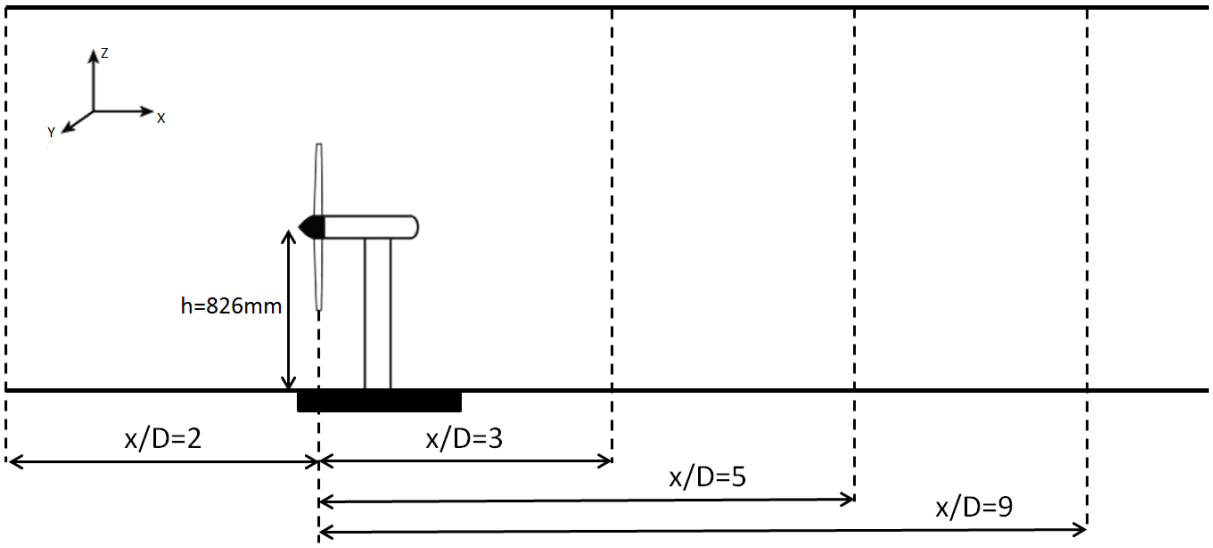

Figure 4.8: Experimental setup for a single turbine.

4.2.1 Power output and thrust

The power coefficient curves of the two model turbines, varying the tip speed ratio λ and the free stream velocity U_∞, are depicted in Figure 4.9. The C_P is obtained with a low background

turbulence level. The first turbine (T1) curves are illustrated in Figure 4.9(a). The C_P is recorded for six inflow wind speeds, from U_∞ = 8.7 m/s to U_∞ = 11.7 m/s, while for the second turbine (T2), the six velocities cover a range between U_∞ = 8 m/s and U_∞ = 12 m/s (Figure 4.9(b)). In Figures 4.9(c) and 4.9(d) a magnified view is shown.

Considering the first turbine (4.9(a)), differences in C_P curves are getting smaller starting from U_∞ = 10.9 m/s. However, the maximum point of the 10.9 m/s curve is slightly smaller than the others and the curve presents a flatness on top. Starting from 11.4 m/s this behaviour tends to disappear. One of the purpose of the array investigations is to find the optimum point of the "wind farm", so a flatness on the power curve is not considered acceptable and a reference wind speed of 11.5 m/s is chosen.

For the following array analysis, it has to be pointed out that the maximum C_P value for turbine T1 in low turbulence flow is C_P = 0.47 at λ = 6 for the chosen reference velocity. The runaway tip speed ratio is λ = 11.4. C_P values are found in agreement with results presented in similar studies [14, 40].

The distinct drops in C_P around the design tip speed ratio (λ = 6) are the effect of a Reynolds dependent behaviour of the airfoil (see Section 3.2). Because of that, at low wind speed the torque generated by the blades decreases. This effect is shown up to 10.9 m/s, lowering in intensity, increasing the reference velocity.

The same attitude can be observed for turbine T2 (Figure 4.9(b)). However, the magnitude of these effects is actually lower: at U_∞ = 8 m/s the bump is less deep than the one of turbine T1 at U_∞ = 8.7 m/s (Figures 4.9(d) and 4.9(c)).

The blade design is carried out considering the hub diameter of turbine T2. On the other hand Turbine T1 has a slightly bigger hub diameter, affecting the aerodynamic of the blade. Therefore the maximum C_P value of turbine T2 is higher than the turbine T1, resulting in a C_P = 0.48 obtained at λ close to 6 and U_∞ = 11.5 m/s. This value is slightly bigger ($\approx$ 5%) than what found by Krogstad et al. [8] for the same tip speed ratio. Even if the boundary conditions were quite similar, the difference is probably due to the reference velocity as in that case it was used the pressure drop across the contraction corrected by an empirical factor (n.a.), while for the present work a pitot probe is used (Section 3.8). For the same reason, velocity independent power curves were found from $\approx$ 9.5 m/s, while in the present study (in agreement with [14, 32, 33, 5, 41]) $\approx$ 10 m/s need to be reached to avoid this dependency for T2.

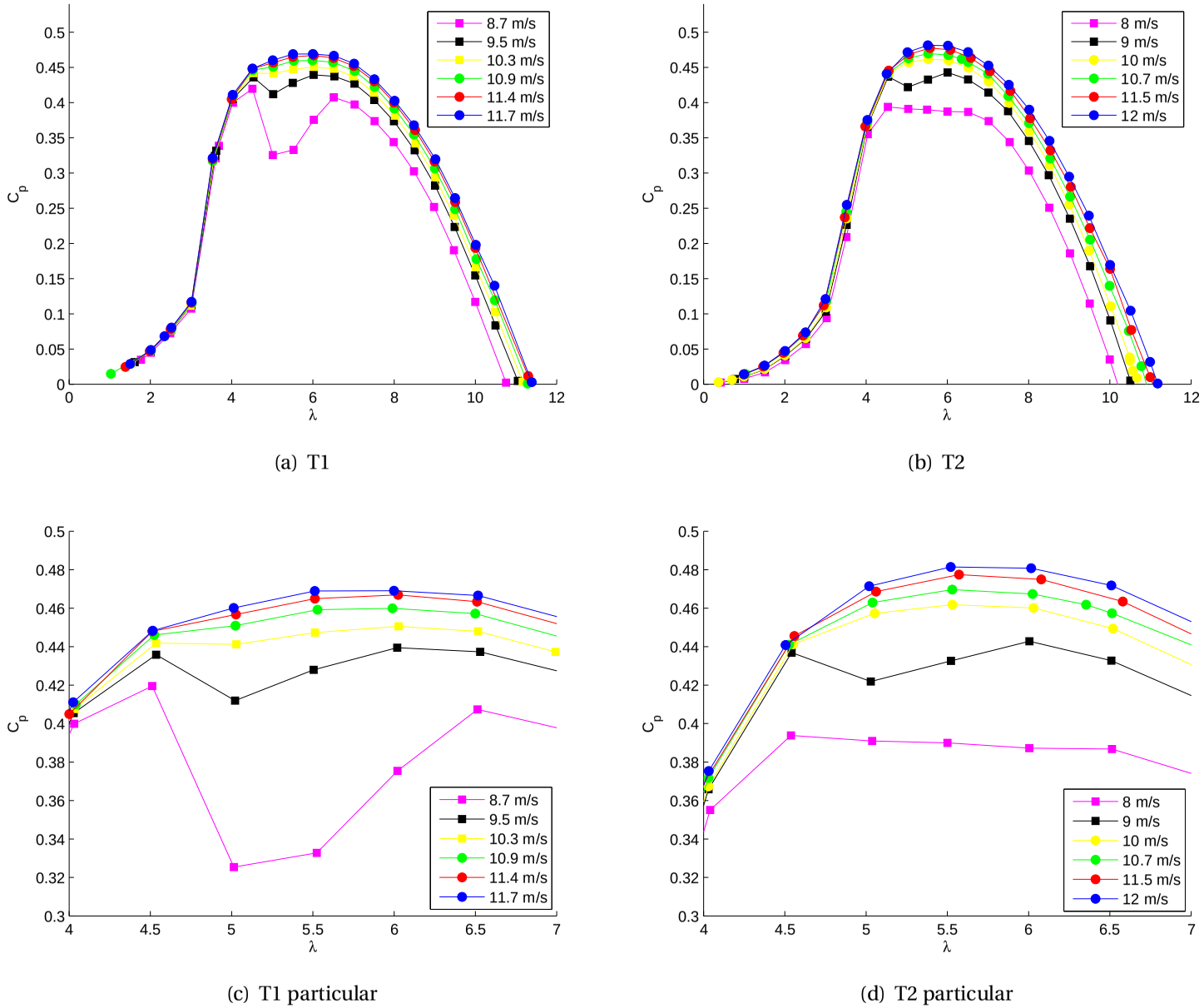

(a) T1

(b) T2

(c) T1 particular

(d) T2 particular

Figure 4.9: Power curves of the two model turbines in low turbulence flow. Comparison between different incoming wind speeds.

Power coefficient curves are also recorded in a high background turbulence level flow (10% on the rotor plane) for the 2 turbines (Figures 4.10 and 4.11). Investigations at different wind speeds have shown a lighter Reynolds dependency behaviour (as expected). The turbulent flow, hitting the blades, prevents the laminar bubble formation over the airfoils. Nevertheless lower the wind speed, lower the C_P values.
In this case maximum C_P values (at $U_\infty = 11.5$ m/s) are measured at $\lambda = 6$ and they are $C_P = 0.48$ for turbine T1 and $Cp = 0.50$ for turbine T2.

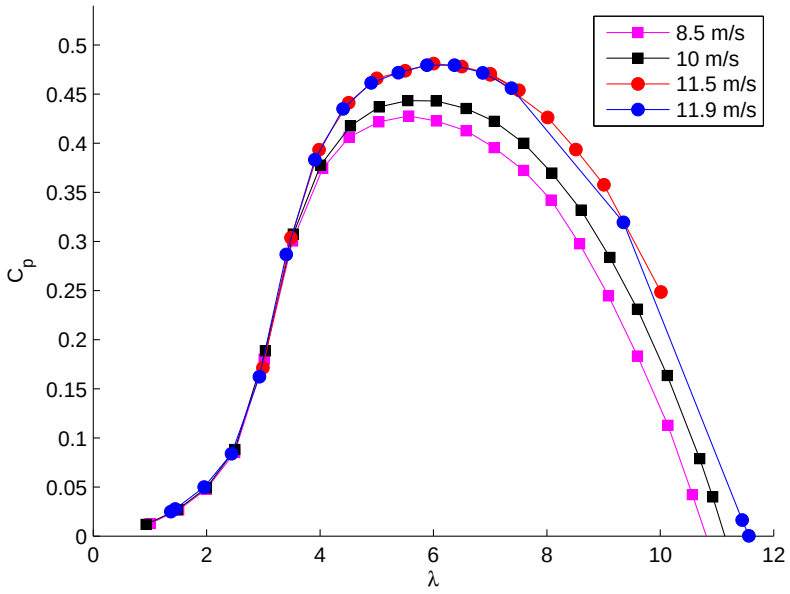

Figure 4.10: Power curves of the first model turbine in high turbulence flow. Comparison between different incoming wind speeds.

Results show a slightly increase in the power curve when analysing the performances in a high turbulent flow. One of the reason may be found in the airfoil behaviour, which seems showing better performances with a high turbulence level, especially for turbine T1. The result slightly diverge with what found by Mikkelsen [21], but some boundary conditions are different, as well as the reference velocity method that is used in the two different cases. As the differences in peak power performances are widely insight the accuracy of the instruments, it will not be further discussed.

The following Table 4.1 can be derived, summing up the maximum power coefficient that each turbine can reach with the two inflow conditions. These values will be used as reference for considerations on the array efficiency.

The thrust coefficient is investigated too. As regards T1 thrust, it is checked to be in agreement

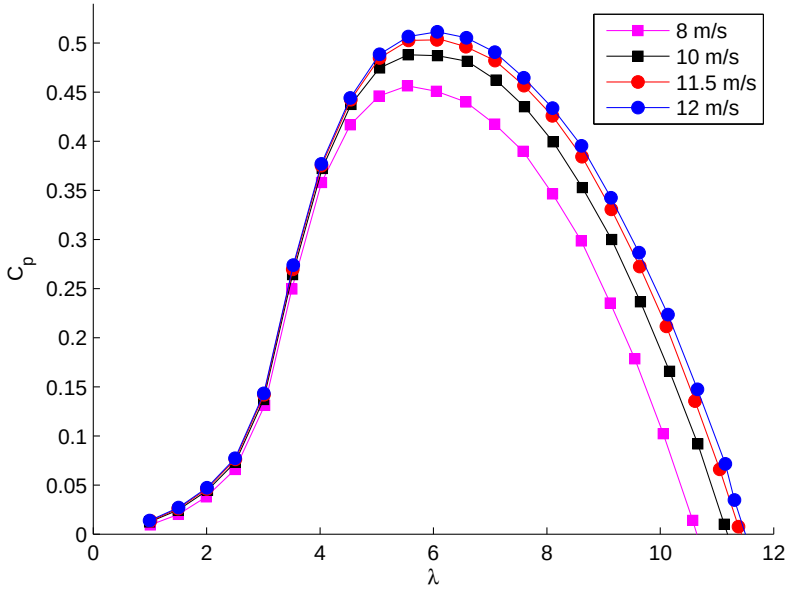

Figure 4.11: Power curves of the second model turbine in high turbulence flow. Comparison between different incoming wind speeds.

	C_P T1 [-]	C_P T2 [-]
low turbulence (empty)	0.47	0.48
high turbulence (grid)	0.48	0.50

Table 4.1: T1 and T2 Maximum Power coefficient $C_{P,max}$ in stand alone configuration for the two incoming flow conditions.

with previous results (e.g. [34]) for the incoming reference velocity; however an intensive study is not carried out as this parameter does not vary in the different array configurations. Conversely, T2 thrust is recorded over a wide range of inlet wind speeds in order to have a term of comparison for the following studies.

The thrust curves for turbine T2 are presented in Figure 4.12. On the left side the results obtained with a low turbulence level on the incoming flow are shown. Hardly any difference can be found varying the inlet wind speed. A small deviation can be observed for the 8 m/s curve between $\lambda = 5$ and $\lambda = 7$. Due to the Reynolds number dependency, a much lighter effect is present on thrust curves, comparing it with power curves. On the right side high turbulence thrust curves are depicted. At low tip speed ratios the different velocities curves are totally congruent, while approaching runaway points a certain spread in results is present. It has to be underlined that high turbulence background level heavily affects the thrust coefficients of the turbine, leading to stronger loads on the tower.

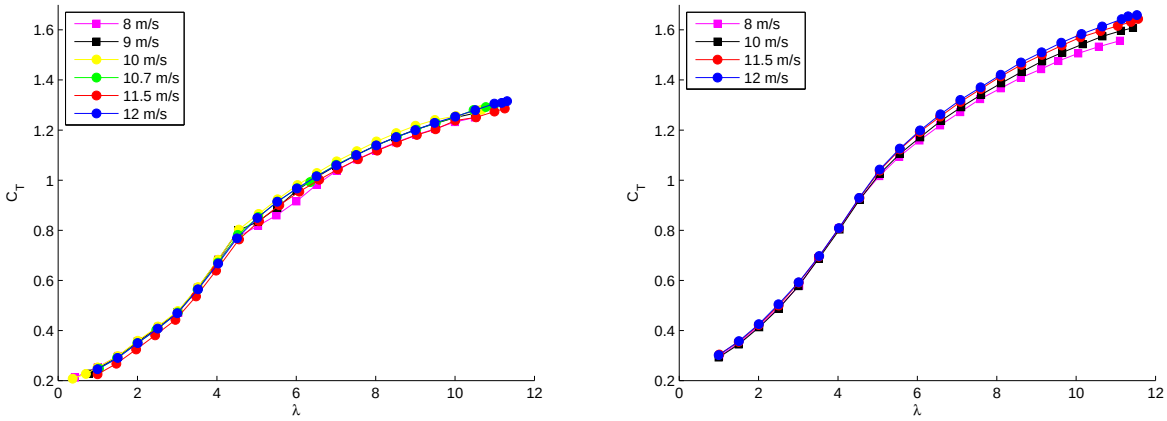

(a) empty tunnel

(b) grid

Figure 4.12: Thrust curves for T2: Comparison between different incoming wind speeds and considering the two incoming flow conditions.

According to Betz theory, the thrust coefficient of a wind rotor can reach a maximum value of 1. In this case the models are installed in a closed test section, so they are affected by blockage, speeding up the flow. This effect leads to a higher thrust coefficient, as the reference speed is lower than the actual velocity felt by the rotor. Moreover thrust measurement is not the result of the axial decomposition of blade loads, but it is taking into account the whole turbine (tower and hub included). Measurements of the turbine thrust with no blades reveals a coefficient of $C_T \approx 0.1$. However, more than 50% of the tower height is hidden by the rotating blades, so it is decided not to subtract this value from the total C_T measured.

4.2.2 Wake of a single turbine

The object of this project is to analyse turbine wake effects on the performances a second turbine located downstream. Hence a preliminary study of a single turbine wake is carried out. Horizontal wakes are recorded at the hub height of the turbine, velocity deficit and turbulence intensity are analysed in several configurations: at different distances behind the turbine (3D, 5D and 9D), with the turbine running at TSR = 4, 5 and 6, both in a low background turbulence level and in a high background turbulence level (10% over the rotor plane).

The velocity deficit in the wake depends on momentum deficit behind the rotor, thus on the thrust coefficient (C_T). In Figure 4.13, velocity deficit curves are shown, measured at 3 different downstream positions in a low background turbulence level. On the X-axes local velocity is adimensionalized by the free stream velocity (U_{ref}); on the Y-axes the radius relative position is represented. The turbine is running at TSR=6 so that C_T of the turbine is constant. Moving downstream from the rotor plane, velocity deficit recovers as momentum is fed into the wake through the shear layer. Meanwhile, momentum feeding produces the radial expansion of the wake. In a full scale turbine, flow velocity reaches the incoming free stream value radially outside the wake; in wind tunnel experiments this velocity is found higher than the freestream value because of blockage effect. The flow inside the wake presents a lower value than U_∞, according to the mass conservation, a higher value is achieved outside.

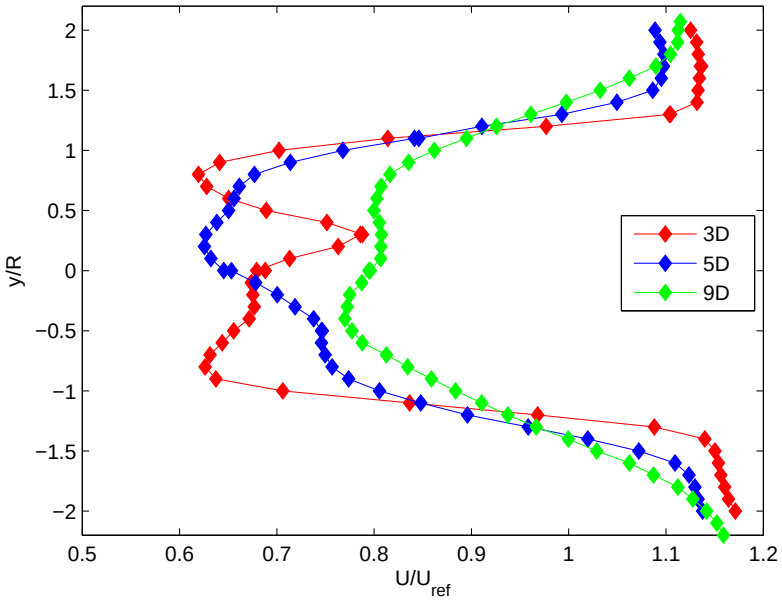

Figure 4.13: Horizontal velocity deficit profiles at 3D, 5D and 9D distance behind the turbine working at optimum TSR ($\lambda = 6$) in a low background turbulence level flow.

As it is noticeable from Figure 4.13 the flow velocity outside the wake reaches even 15% higher values then the incoming free stream velocity (e.g. 3D distance). Similar results are obtained in [34, 40]. The wake limits are well defined by a constant velocity profile (even if the value is higher than U_{ref}). At 3D the transition region between the wake and the free stream is abrupt while for 9D it is more gradual according with the physical phenomenon.

In Figure 4.14 turbulence intensity curves are shown, measured at 3 different downstream positions in a low background turbulence level. On the X-axes the turbulence intensity [%] is represented, while on Y-axes the radius relative position is kept.

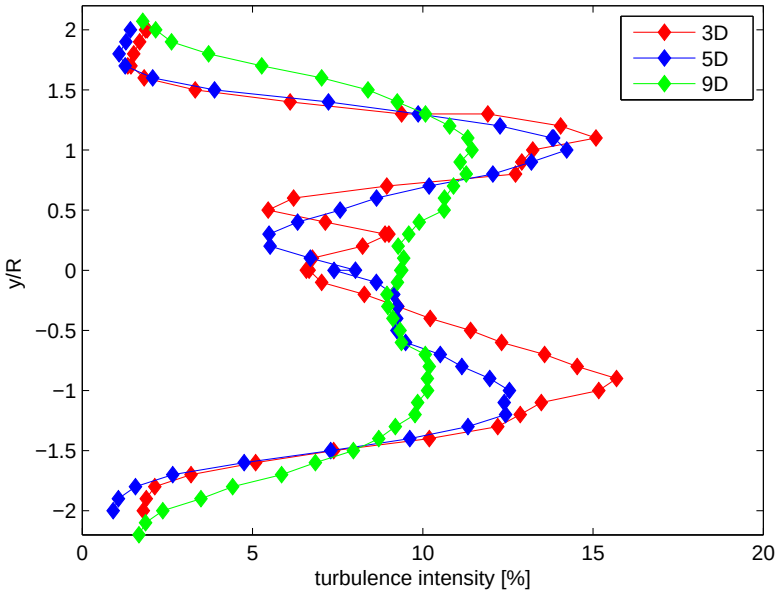

Figure 4.14: Horizontal turbulence intensity profiles at 3D, 5D and 9D distance behind the turbine working at optimum TSR ($\lambda = 6$) in a low background turbulence level flow.

As described in Section 2.3 the wake region can be divided in 2 areas: the first where the characteristics of the rotor can be recognized (Near wake), the second where the flow is considered completely developed, axisymmetric and with absence of streamwise pressure gradient (Far wake). For a full scale turbine, as explained in [25], the transition between near and far wake can be evaluated from 2D to 5D downstream the rotor, depending on the background turbulence level. In wind tunnel experiments, it happens further downstream as described in [26]. In Figure 4.13 and in Figure 4.14 the transition between these 2 areas can be detected. In 4.13 a smoothness in the velocity profile is detectable increasing the downstream distance, even if at 9D the Gaussian shape is not assumed. So the full transition to far wake is not ended. In Figure 4.14 the rotor characteristics are visible at 3D and 5D by the presence of distinct peaks.

Those peaks reveal the tip vortex and the nacelle, typical of the near wake region, while at 9D tip vortex pair up and break down into turbulence by increasing the turbulence level in the wake. For these reasons it can be affirmed that transition to far wake is occurring at higher distance from the rotor with respect to full scale cases.

In Figure 4.15 and Figure 4.16 velocity deficit and turbulence intensity are shown in the same configuration but in a high background turbulence level (10% on the rotor plane).

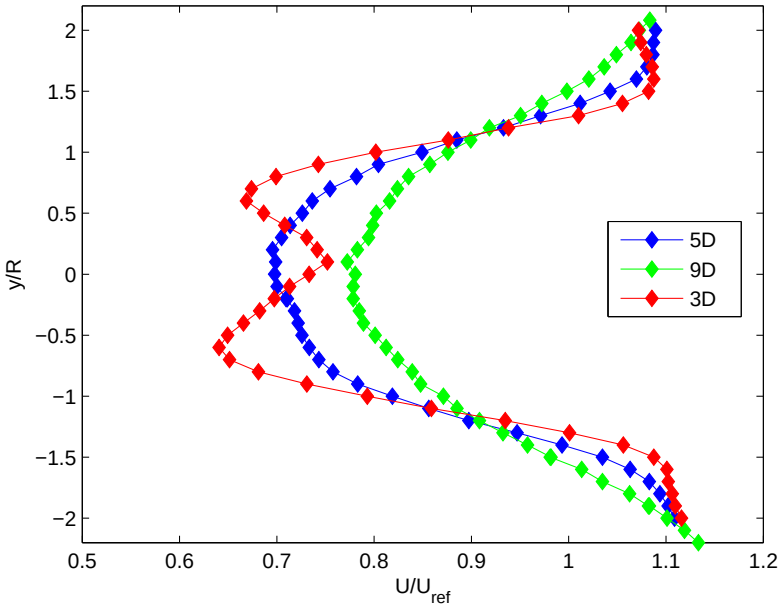

Figure 4.15: Horizontal velocity deficit profiles at 3D, 5D and 9D distance behind the turbine working at optimum TSR ($\lambda = 6$) in a high background turbulence level flow (10% on the rotor plane).

The velocity deficit curves start to show axisymmetric characteristics already at 5D downstream the rotor plane (Figure 4.15), while at 3D the rotor footprint is still evident; it means that the transition from near to far wake is completed between 3D to 5D. Conversely in the low background turbulence level case still at 9D the axisymmetry does not appear, as clear from Figure 4.13. Thus, the turbulence induced by the grid accelerates the near-far wake transition, in terms of velocity deficit profile, because of a stronger mixing phenomenon in the flow.

The turbulence intensity curves, in Figure 4.16, show that turbulence peaks are less deep and abrupt with respect to the low background turbulence case. Anyway peaks are still visible at 5D, even if the transition to far wake is completed. As already explained in Section 2.3 this is due to the different recovery rate between turbulence intensity and velocity deficit to the unobstructed levels.

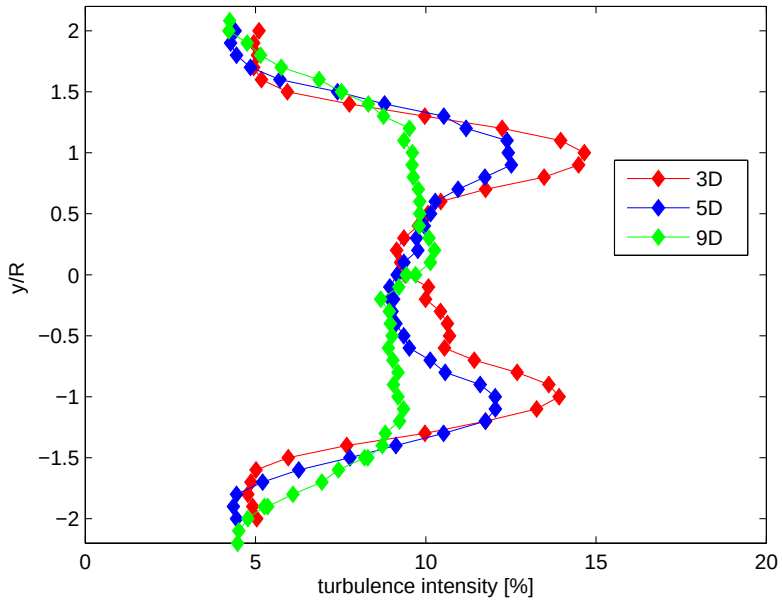

Figure 4.16: Horizontal turbulence intensity profiles at 3D, 5D and 9D distance behind the turbine working at optimum TSR ($\lambda = 6$) in a high background turbulence level flow (10% on the rotor plane).

It has to be considered that the turbulence levels depicted in Figure 4.16 took into account the overall turbulence intensity level so, when compared with Figure 4.14, the peaks generated by the turbine in case of high turbulence background level are lower then the peaks in case of low turbulence background level.

The operating tip speed ratios of the turbine have a decisive impact on the wake evolution. Tip speed ratios are affecting the aerodynamics of the blade: varying the rotational speed of the rotor, the actual angle of attack along the blade is modified, so each blade section works in a different configuration. As described in [34], at much higher then optimum TSR, the outer blade sections tend to work at almost null angle of attack. At the same time, the inner sections generate negative lift and feed momentum into the wake. The result is an high turbulence intensity along the centre line. These phenomena are noticeable in the wake characteristics.

In Figure 4.17 these effects are shown by representing velocity deficit and turbulence intensity in the wakes at a given distance from the rotor, at different TSR. In Figures 4.17(a) and 4.17(b) velocity deficit and turbulence intensity are measured at 3D distance from T1 rotor plane. In Figures 4.17(c) and 4.17(d) and in Figures 4.17(e) and 4.17(f) respectively 5D and 9D velocity deficit and turbulence intensity are illustrated.

Focusing on Figures 4.17(a), 4.17(c), 4.17(e), at a given downstream location (e.g. 3D) the radial

transit position between wake and undisturbed flow is constant, so no TSR dependency on radial expansion can be deduced. This validates the engineering wake models that fix the wake rate growth parameter to a constant value in order to describe the expansion itself; this parameter is modelled only depending on the flow turbulence background level [42, 43, 44, 45, 46].

From Figure 4.17(a), being the flow in the near wake region, the characteristics of the rotor is highly evident. Varying the TSR, rotor turbine sections work in different ways, directly influencing the velocity deficit. Even if the variation in tip speed ratios is quite small ($5 \leqslant TSR \leqslant 7$), velocity deficit curves differ particularly in the inner part ($y/R \approx 0$). This is even more clear in Figure 4.17(b) where big variations in turbulence intensity are registered in the same TSR range. In Figures 4.17(c) and 4.17(e) variations in the inner wake areas are no longer visible due to the higher distances from the rotor plane.

At 5D distance (Figure 4.17(c)), differences in velocity deficit are found very small varying the TSR so, velocity deficit curve for $TSR = 4$ is given. The variations between TSR 5 and 6 curves are smaller than between TSR 4 and 5: this is due to the rotor functioning. At $TSR = 4$ lower energy is extracted, so higher velocity is reached in the wake. After $TSR = 4$ the C_P and the C_T are strongly rising (Figures 4.9(a) and 4.12(a)). Close to the design point ($TSR = 6$) C_P and C_T variations are smaller resulting in similar velocity deficit profiles behind the rotor. At $TSR = 4$ less energy is extracted so higher velocity is reached in the wake.

A general feature that is detectable, comparing the off-design working conditions, is about the turbulence intensity strength. Increasing the TSR of the turbine, the turbulence intensity in the wakes increases, since higher thrusts on the turbine induces strongest mean velocity gradients. This is visible in Figures 4.17(b), 4.17(d) and 4.17(f) where both tip peaks and the overall level are monotonically increasing with the TSR.

Finally, at 9D behind the rotor plane, (Figures 4.17(e) and 4.17(f)) almost no difference is encountered with TSR variations.

Similar considerations can be worked out also for a single turbine in an high background turbulence flow. In Figure 4.18 wake measurements from the grid configuration are drawn varying TSR and distances. In each of the Figures 4.17(a), 4.17(c) and 4.17(e) no appreciable difference is seen induced by TSR variation; the high turbulence level introduced by the grid induces an high mixing, smoothing the velocity deficit. The same consideration applies to the streamwise turbulence intensity (Figures 4.17(b), 4.17(d) and 4.17(f)). Only a small TSR dependency can be detected 3D after the turbine (4.17(b)) as a overall increase in the turbulence intensity rising the TSR, but similar profiles are shown.

The TSR dependency in the analysed range ($5 \leqslant \lambda_1 \leqslant 7$) is found not to be very strong in all the study cases. This is expected not to widely affect the T2 performances. As no big differences are present in the T2 incoming flow, not very far behaviour are awaited in T2 power performances while working in array. This analysis will be held in next Section (4.3). However, it has to be taken into account that the wake measurements are performed on an horizontal line, so they are representative of the flow, but do not fully describe flow asymmetries and three-dimensionality. This is a limit for comparison with the power performances, but still a good insight can be achieved with the actual measurements.

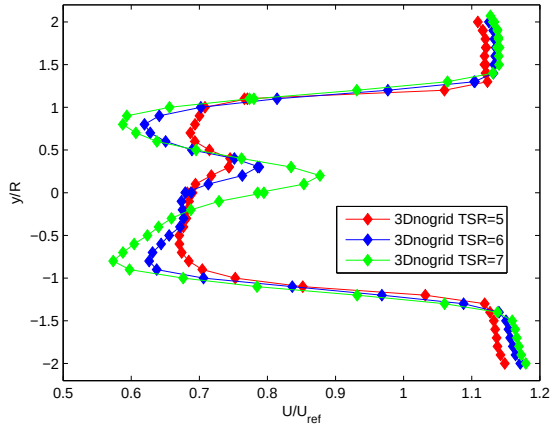

(a) Velocity deficit, 3D from the rotor.

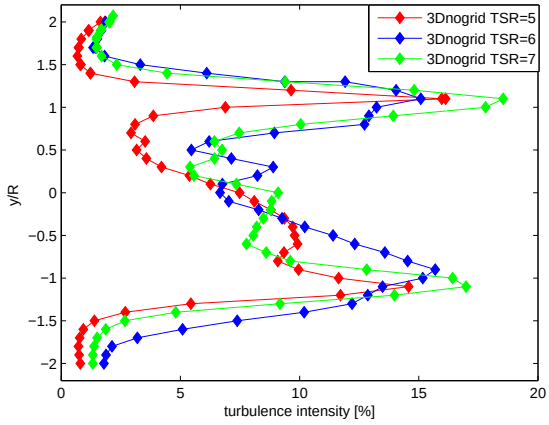

(b) Turbulence intensity, 3D from the rotor.

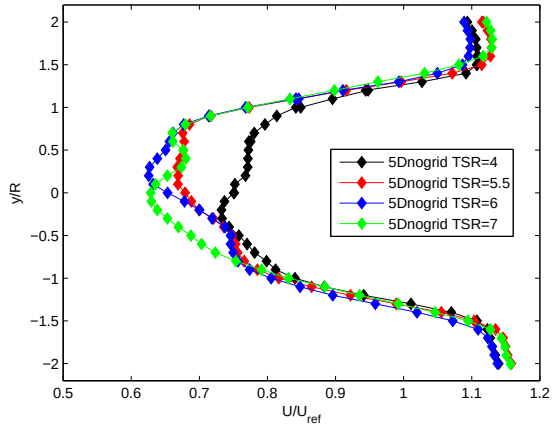

(c) Velocity deficit, 5D from the rotor.

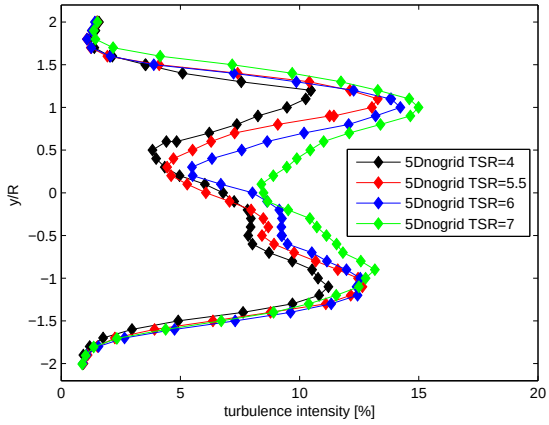

(d) Turbulence intensity, 5D from the rotor.

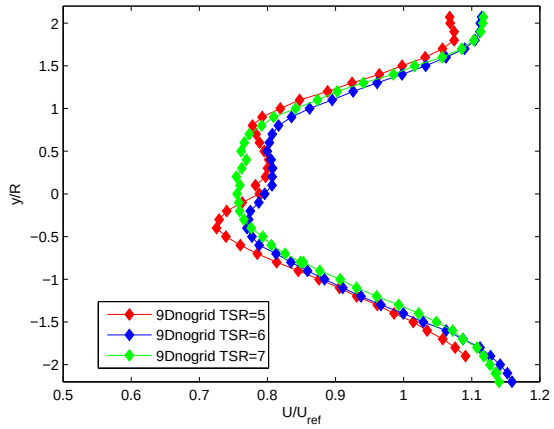

(e) Velocity deficit, 9D from the rotor.

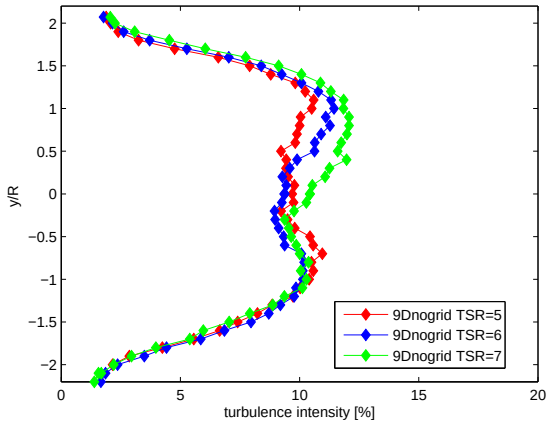

(f) Turbulence intensity, 9D from the rotor.

Figure 4.17: Horizontal velocity deficit and turbulence intensity profiles at 3D, 5D and 9D distance behind the turbine working at different TSR ($\lambda = 5,6,7$) in a low background turbulence level flow .

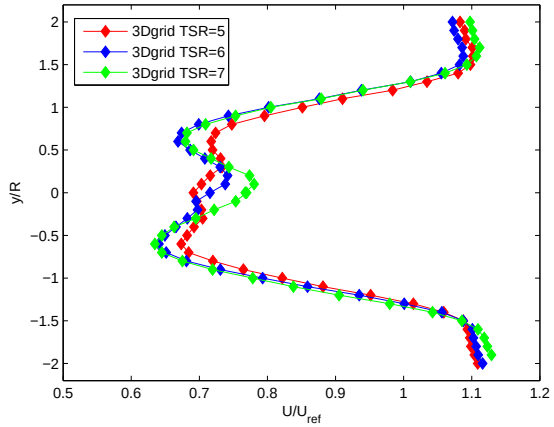

(a) Velocity deficit, 3D from the rotor.

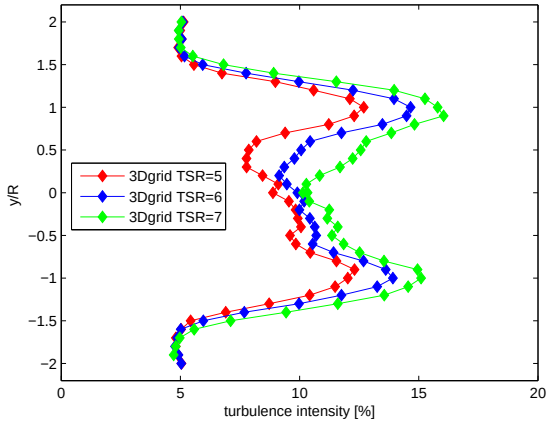

(b) Turbulence intensity, 3D from the rotor.

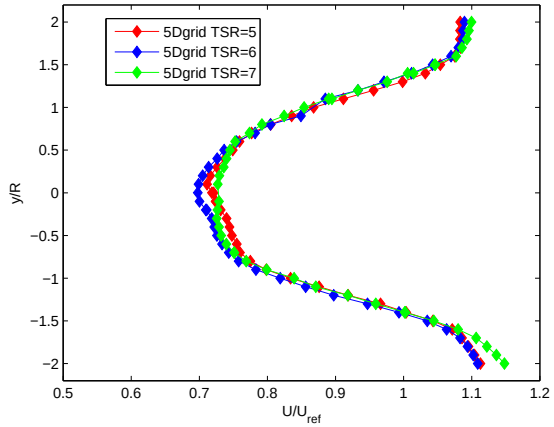

(c) Velocity deficit, 5D from the rotor.

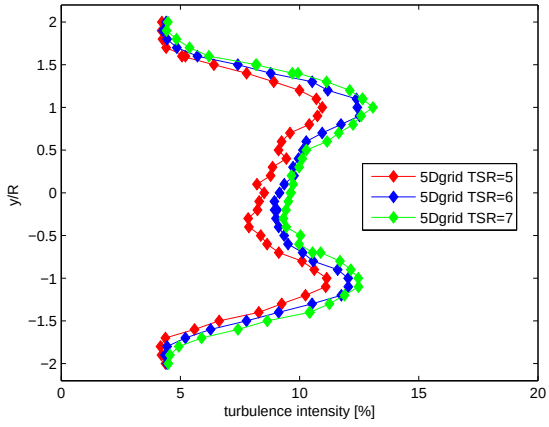

(d) Turbulence intensity, 5D from the rotor.

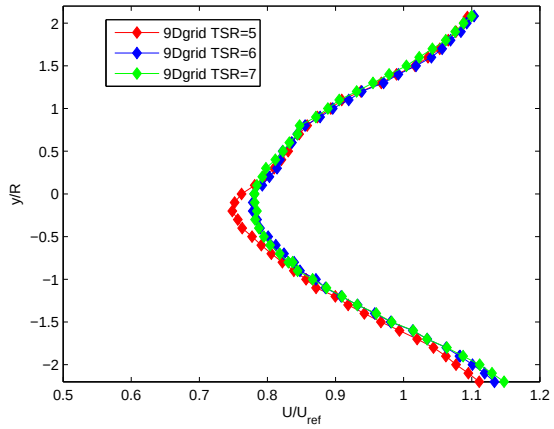

(e) Velocity deficit, 9D from the rotor.

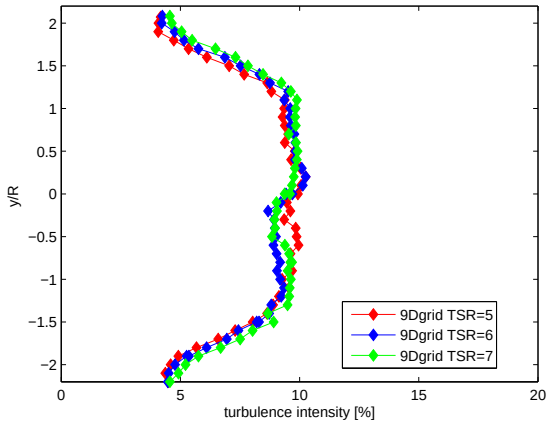

(f) Turbulence intensity, 9D from the rotor.

Figure 4.18: Horizontal velocity deficit and turbulence intensity profiles at 3D, 5D and 9D distance behind the turbine working at different TSR ($\lambda = 5, 6, 7$) in a high background turbulence level flow (10% on the rotor plane) .

4.3 Array configuration

In this section it is described the array power output performed with the second turbine (T2) working in the wake of T1. The experimental setup consists of the two turbines distributed along the tunnel as in Figure 4.19. The distance between the turbines is varied. The two models are aligned in the centre of the test section and the hub height is set to 826 mm from the floor, for both turbines. Experiments are run under both flow conditions.

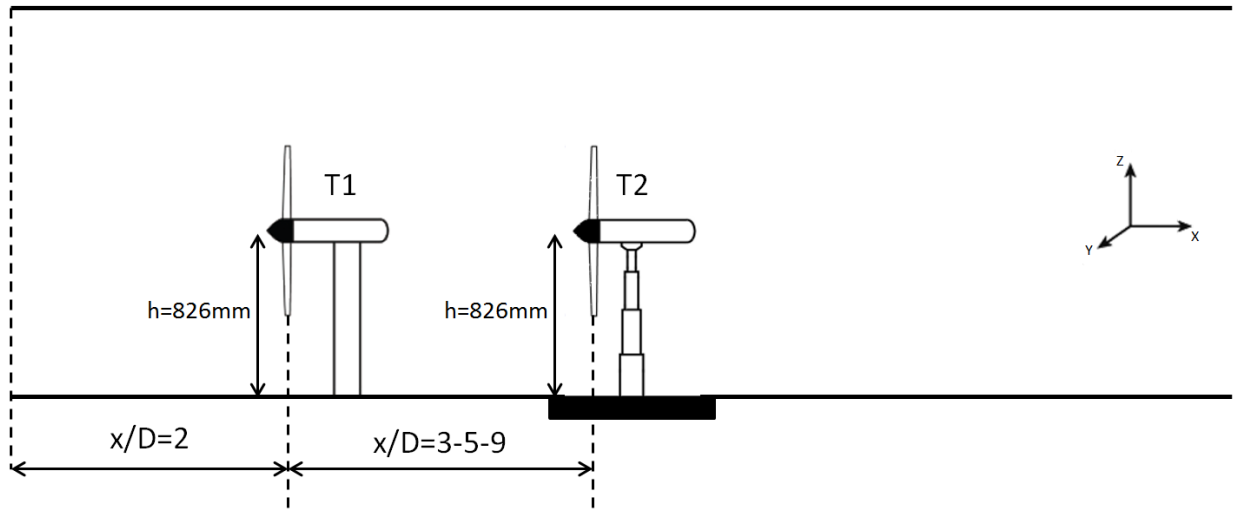

Figure 4.19: Experimental setup for the array of 2 turbines

4.3.1 Parametric study of power output

When two turbines are aligned, the wake of the upstream machine is the inlet flow to the second one. The downstream turbine feels therefore a complex inflow, characterized by lower averaged velocity, high turbulence intensity, non-uniform neither symmetric velocity profile and non isotropic turbulence (refer to wind turbine wake features, already described in Chapter 2).

The power output parametric study of the wind farm arranged in the tunnel consists in the variation of:

TSR The tip speed ratio of both turbines is ranged. The first turbine is regulated at a fix TSR while a complete C_P curve for the second turbine is obtained. It results in a matrix of TSR of both turbines. λ_1 varies from 3 to 10 and λ_2 from 1 to 7 (adding the runaway point), the matrix is shown in Figure 4.20. A total number of 196 measured points (14x14) is obtained.

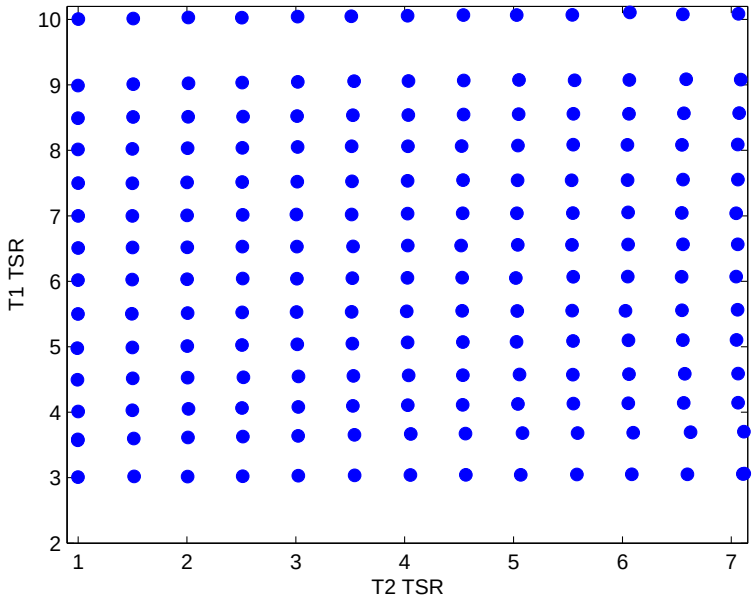

Figure 4.20: Example of input TSR.

Inflow turbulence Another parameter used is the turbulence background level. All experiments are performed under two different incoming flows: high and low background turbulence level. The inflow conditions are deeply analysed in the former Section (4.1).

Downstream distance The second model is positioned at three downstream distances from the first turbine: 3D, 5D and 9D (considering the second turbine diameter $D = 894mm$ as reference).

Varying these parameters, 6 analysis configurations are defined as described in Table 4.2. For each configuration the TSR matrix is carried out.

NAME	Downstream distance	Turbulence level
A	3D	low (empty tunnel)
B	5D	low (empty tunnel)
C	9D	low (empty tunnel)
D	3D	high (grid)
E	5D	high (grid)
F	9D	high (grid)

Table 4.2: Summary of the different array configurations.

It is checked, for confirmation of results quality, that the power coefficient curves of the first turbine match what presented in Section 4.2. The turbine T2 is not affecting power performances

of T1, accordingly, the differences are always widely inside the instruments accuracy. In latter section these results will be presented.

It is decided to describe in this Chapter all the results coming from an exemplifying configuration (A), while, all the outcomes from the 6 different configurations are fully accessible in Appendix A. Moreover a detailed comparison is presented in the following, emphasizing differences and similarity in terms of power production.

It is reminded to the reader that the reference velocity is set to 11.5 m/s.

4.3.2 Array performances for configuration A: 3D downstream separation distance and low background turbulence level

The two turbines performances and the thrust of the second turbine are recorded for fixed inflow condition (low turbulence) and downstream distance (3D).

In Figure 4.21 the power coefficient of the second turbine is depicted for different tip speed ratios of both turbines. On the left side a surface fitting all the recorded data (blue dots) shows the C_P trend for the second turbine (on Z-axis). The X-axis represents λ_2, while Y-axis λ_1. On the right side a selection of data is illustrated to highlight more clearly the results. Sectioning on a plane parallel to X-Z for a defined λ_1 value (Y) the curves are obtained.

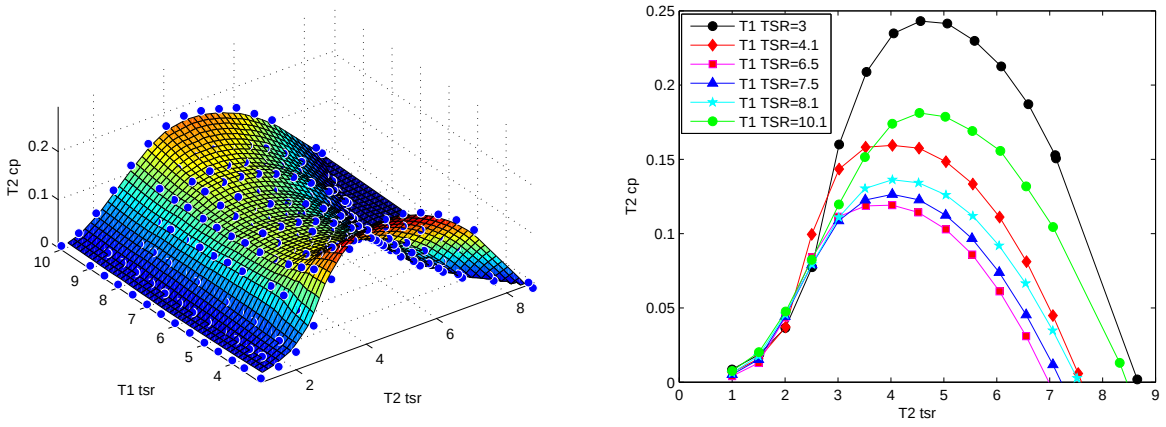

(a) C_P T2 surface

(b) C_P T2 selection of results

Figure 4.21: Second turbine T2 power coefficient curves. T2 operating in T1 wake (Configuration A: 3D downstream distance and low turbulence background level).

Several considerations require to be shown. The power coefficient presents very small values if compared with the result achieved when T2 stands alone in the test section. If running alone,

the maximum C_P recorded is 0.48, while in this configuration it is ranging from 0.12 to 0.24, depending on T1 operating point. One of the reason is that both turbines are using the same reference velocity: actually the incoming flow to the second turbine presents a smaller averaged velocity because T2 is in T1 wake. Moreover the incoming flow is by no means constant on the rotor swept area. Refer to Section 4.2.2 for the detailed description of T1 wake. The T2 power curves are shown in Figure 4.22 in two different cases: when running alone and when running behind T1 working at its optimum ($\lambda_1 = 6$). A shift towards smaller values in tip speed ratios is visible. It is an effect of using the same reference velocity for the two turbines as the tip speed ratio is calculated on it (Equation 2.1).

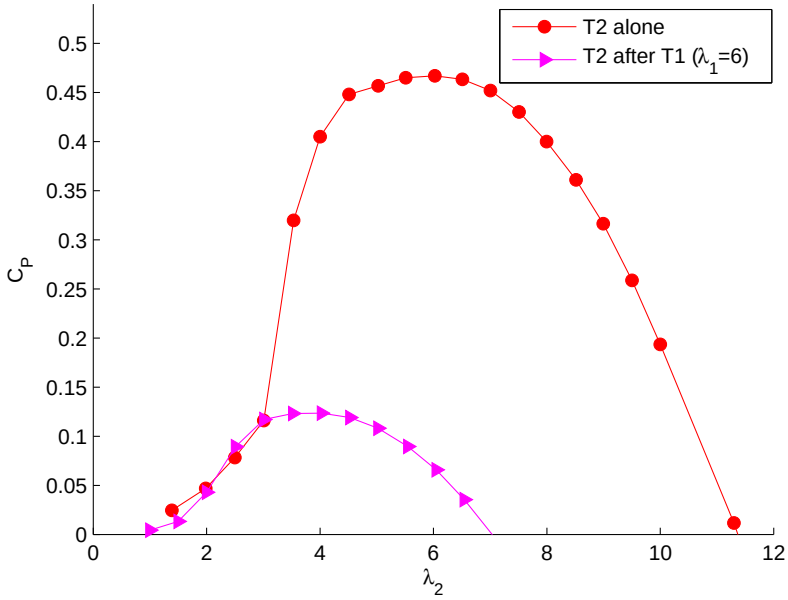

Figure 4.22: T2 power performances in 2 conditions: running alone and after T1 at its optimum working point ($\lambda_1 = 6$).

The second turbine performances depend on the TSR of the first machine. As the first turbine is close to the optimal point ($\lambda = 6$), it extracts as much energy as possible from the wind so that there is not much left behind for the second turbine. On the other hand, when the first turbine is running at λ far from the optimum, more energy is available for the second turbine. This behaviour is clear on the surface plot (Figure 4.21(a)). It can be noticed an asymmetry in the attitude of recovering T2 performances while T1 moves away from the optimum working λ. When λ_1 is smaller than 6, higher C_P could be reached compared with cases of $\lambda_1 > 6$. This behaviour suggests that tip speed ratios are better decreased than increased from the optimum value, if one wants to guarantee more energy for the downstream turbine, varying this parameter.

Another aspect to analyse is the absence of non-uniformities in power curves which can be re-

lated to laminar effects (Reynolds dependency). An approximated inlet velocity is of the magnitude of 8 m/s, so this effect should be visible; however the turbulence induced by the upstream turbine and the asymmetries in the flow have the same effect of the grid in terms of smoothing the power curves.

After analysing the power coefficient curves of the downstream turbines, thoughts on the array efficiency can be assess. For each configuration $\lambda_1 - \lambda_2$ the power coefficients are summed and divided for the sum of the maximum that the two turbines would be able to reach as standalone (Table 4.1), so the array efficiency (E [%]) is obtain (Equation 4.1). $E = 100\%$ would be obtained if T2 were not affected by T1 wake.

$$E = \frac{C_{P,T1} + C_{P,T2}}{C_{P,T1max} + C_{P,T2max}} * 100 \tag{4.1}$$

The array efficiency is exhibited in Figure 4.23. Fitting the measured points (blue dots), a surface is derived (4.23(a)). In Figure 4.23(b) a contour plot of maximum values is extrapolated. It is possible to underline that the maximum is reached running the first turbine at $\lambda_1 \approx 5$, and the second at $\lambda_2 \approx 4$. These values differs from what found in stand alone functioning ($\lambda_1 = \lambda_2 = 6$, Section 4.2).

The relevant aspect is the variation in λ_1 with respect to the stand alone condition in order to get the maximum array efficiency. The operating point of the first turbine needs to be reduced down to 5, so that a bigger amount of energy is left to the downstream turbine. The λ_2 variation is less relevant as the second turbine always works in its actual optimum condition. The tip speed ratio of T2 is highly affected on the decision to use the same reference velocity for the two machines.

For this reason, to resume the tests executed in this configuration (A: 3D downstream separation distance, low background turbulence level), the plot in Figure 4.24 is created depending on λ_1.

With the blue square is described the power coefficient curve for the first turbine and the red dots states for the maximum power coefficient that could be reached by the second turbine (at a given λ_1). This trend line shape highlights what has been described before: moving away from the design λ_1 a bigger amount of energy is available for being extracted by the second turbine, so the T2 C_P raises. The black line is the sum of the power coefficients of both machines, thus it is directly proportional to the array efficiency E defined in Equation 4.1. It is evident that, for a wide range of tip speed ratios, the array efficiency is quite constant.

During the experiments the thrust of the second turbine is recorded too. T2 C_T is depicted in Figure 4.25 varying λ_1.

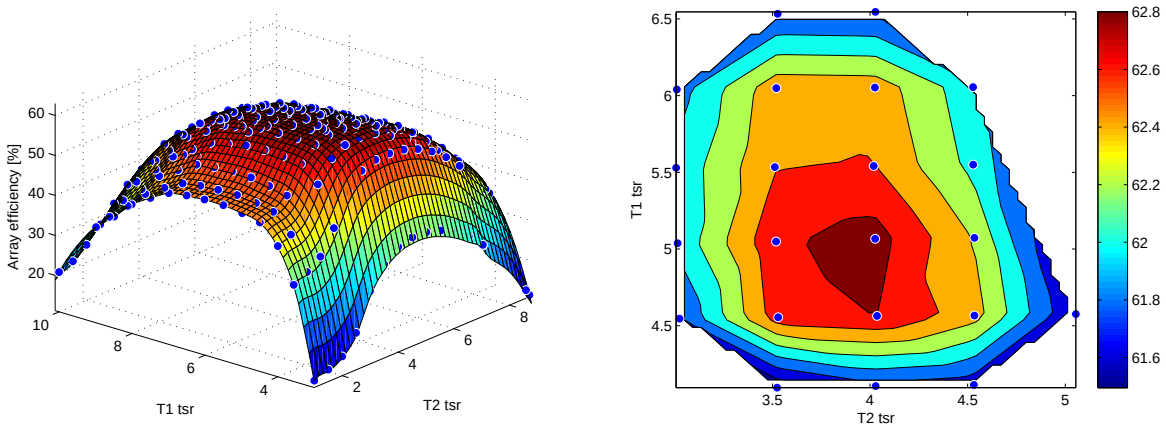

(a) Surface.

(b) Contour plot.

Figure 4.23: Array efficiency (Configuration A: 3D downstream distance and low turbulence background level).

A correspondence between C_P and C_T of the second turbine is visible varying λ_1. Minimum values of C_P corresponds to lower C_T. From $\lambda_1 = 5$ (not shown) to $\lambda_1 = 7.5$ the T2 C_T curves present the smaller values, this is the same range in which the maximum achievable T2 C_P is lower. This behaviour is due to the smaller velocities felt by turbine T2.

The thrust coefficient, as not referred to the actual incoming flow velocity, is not suitable for loads considerations on the tower. As a matter of fact, the T2 C_T presents smaller values than in standalone conditions, while it is known that loads on the tower strongly increase when the turbine is operating in a wake. The high turbulence level in the wake causes the increasing of fatigue loads on the downstream turbine [1, 2]. Nevertheless thrust coefficients are very important for being compared with numerical simulations, so they are recorded and illustrated in the present project.

Similar discussion in terms of general trend could be made for all the 6 configurations analysed. The same graphs will be shown in Appendix A for all the analysed configurations, as a benchmark that could be useful for comparison with numerical simulations.

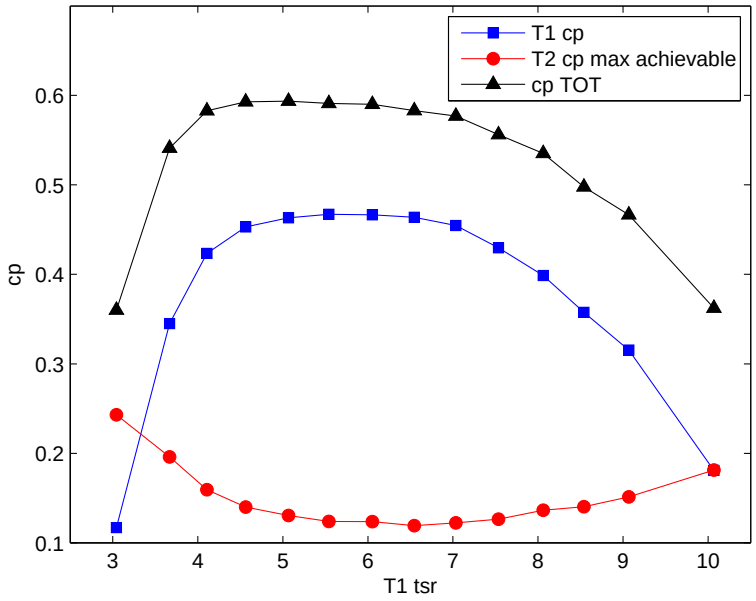

Figure 4.24: Summary of Power performances (Configuration A: 3D downstream distance and low turbulence background level).

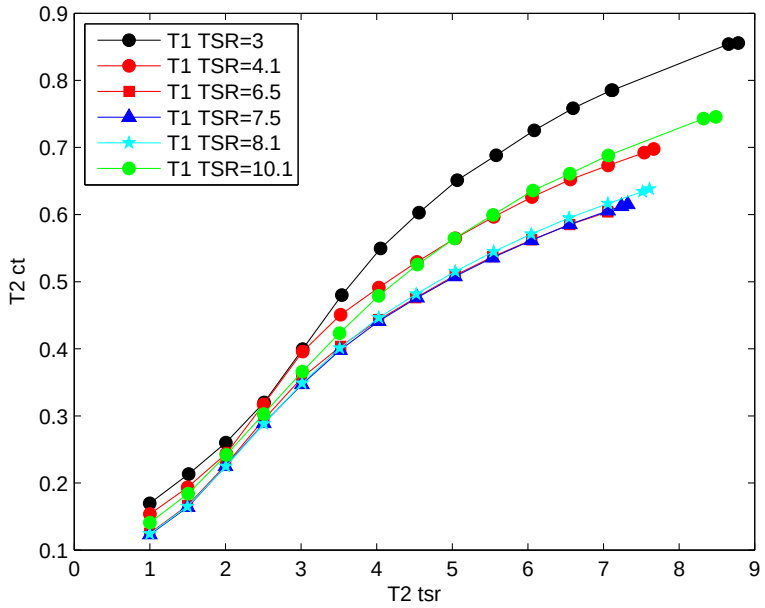

Figure 4.25: Second turbine T2 thrust coefficient curves. T2 operating in T1 wake (Configuration A: 3D downstream distance and low turbulence background level).

4.3.3 Comparison of performances

A comprehensive discussion of the similarities and differences will be held in the following, while, as already mentioned, all the results are available in Appendix A.

First, T1 performances independence in the different configurations will be described. In Figure 4.26 the results are shown. Both in case of low and high turbulence level, the C_P curves, obtained while the second turbine is running at different downstream distances, match quite perfectly the stand alone results. So no dependency of T1 power performances from T2 operation point is demonstrate. The second turbine induction appears negligible already 3D in front of itself, not affecting T1 performances.

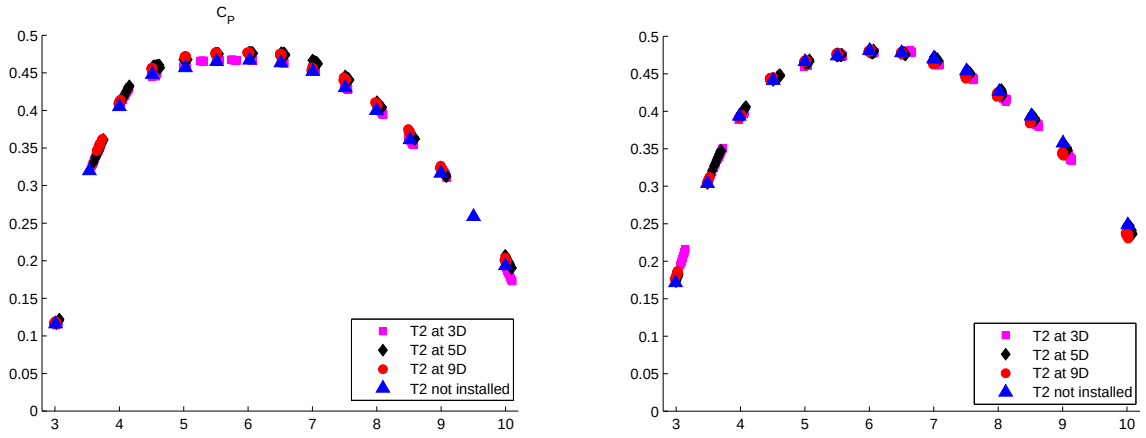

(a) empty (b) grid

Figure 4.26: T1 power performances measured during all experiments. No dependency from T2 operation is shown.

In order to discuss the performances of the second turbine, it is decided to non-dimensionalize the T2 C_P with the value obtained in a standalone condition. Values from Table 4.1 are used. The turbine efficiency will therefore be defined as in Equation 4.2.

$$E_{T2}\,[\%] = \frac{C_P\ wake}{C_P\ standalone} * 100 \tag{4.2}$$

In the following Figure 4.27, it is shown the maximum efficiency that the second turbine can achieve varying the tip speed ratio of the first turbine. First of all, it is possible to observe a shift towards higher values, for bigger rotor distances. In both inflow conditions (Figures (a) and (b)) the blue curve (describing the configurations characterized by 3D distance between rotors) presents the smallest values because the two turbines are quite close to each other. Respectively,

increasing the distance to 5D and 9D, better performances can be achieved. Due to the wake recovery, increasing the distance from the first rotor, more energy is available for the downstream turbine and the efficiency rises as expected.

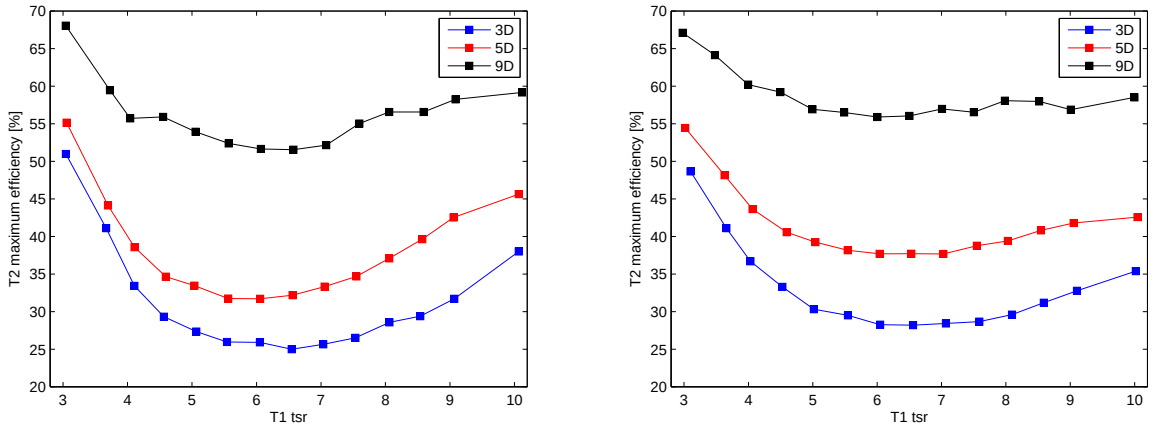

(a) empty (b) grid

Figure 4.27: Maximum T2 efficiency depending on T1 operating point: comparison of all configurations.

An evident difference between the two different incoming flows is in the efficiency values, for a fixed downstream distance. Higher values are reached with the grid positioned at the inlet test section for all input λ_1. This effect is owed to the capability of turbulence to accelerate the wake recovery. As the wake recovery is much faster, higher performances for downstream turbines can be achieved in a high turbulent inflow. This is a positive effect in terms of full scale turbines but should also give an alarm bell when running wind tunnel experiments, pretending them to be an exemplary case for the real world. The grid increases the turbulence from 0.5% to 10% and this unable a turbine efficiency recovery up to 6%.

Another general trend has to be underlined: for all the configurations, the curves have a minimum C_P value for $\lambda_1 \approx 6$ and it increases moving away from the optimum T1 TSR. The reason of this behaviour have already been described in the previous section, but data confirms that the percentage of recovery from the minimum value, varying λ_1, is higher in low turbulence background level.

Comparing $\lambda_1 = 3$ and 9 with respect to $\lambda_1 = 6$, for each configuration the percentage of recovery can be calculated, resulting in an evident bigger value for the low turbulence situation. Figure 4.28 represents the efficiency recovery earlier described. Comparing cases with the same separation distance (i.e. A-D, B-E, C-F) it is evident that the grid limits the recovery with respect to the empty tunnel situation. This should be considered when hypothesis of varying the tip

speed ratio for maximizing wind farm efficiency are tested in the wind tunnel. A high turbulence could significantly affect the magnitude of the second turbine recovery in a bad way. This chart is also very explicative regarding the asymmetry in recovery that we can obtain raising or lowering the tip speed ratio from the optimum point. Clearly a decrease is advisable to allow higher T2 efficiency. It is reminded that the C_T is also important when considering the wake velocity deficit. As it is monotonically increasing with λ_1, this is another aspect suggesting to reduce the tip speed ratio to ensure higher velocities to the second turbine.

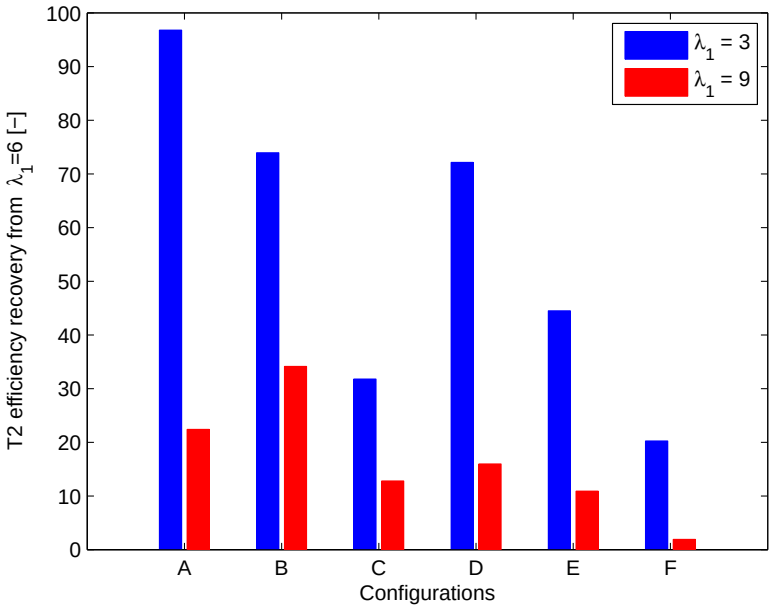

Figure 4.28: T2 efficiency recovery for $\lambda_1 = 3$ and $\lambda_1 = 9$ with respect to $\lambda_1 = 6$

The total array efficiency could be assessed. It is obtained combining both turbines power coefficient as already described in Equation 4.1. The results are depicted in Figure 4.29. For the three distances, at a given λ_1, the maximum T2 C_P achievable is added to T1 C_P, so the array efficiency curve is calculated depending on λ_1. On Figure(a) outcomes from configurations with low turbulence level (A, B and C) are plotted, while in (b) outcomes from high turbulence level incoming flow (D, E and F). The increase in array efficiency with downstream distance is registered. It is worthy of remark that wind tunnel walls highly affect the free expansion of the wake and the velocity deficit recovery. Therefore solid blockage badly influences the T2 power performances.

Focusing on the low turbulent incoming flow, it is observable a quite constant value over a wide range of T1 working points. For λ_1 varying from 4.5 to 6.5, E is constant within ±0.57%. Considering the measurements accuracy, very small differences could be detected for this λ_1 range.

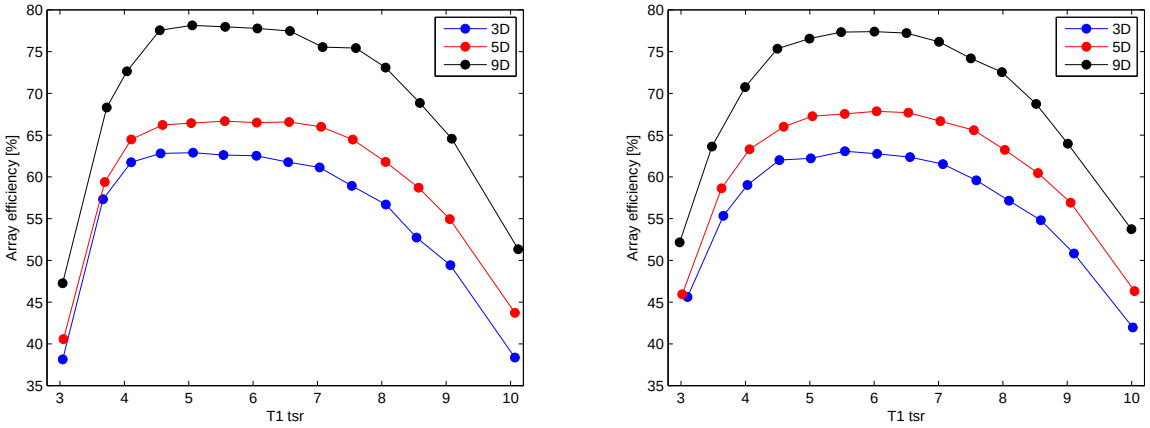

(a) empty (b) grid

Figure 4.29: Maximum array efficiency depending on T1 operating point: comparison of all configurations.

It means that this array of turbines, working in low turbulent flow, could work showing the best performances over a quite wide λ_1 range. Taking a closer look to the results, slightly higher values are reached for $\lambda_1 \in [5,5.5]$ but measurements with better accuracy would have been necessary for these considerations.

Different conclusions could be made in case of high turbulence as the results show a more clear trend. Referring to the same λ_1 range, the array efficiency varies of $\pm 1.05\%$, having a maximum for $\lambda_1 \in [5.5,6]$ and decreasing considerably on both sides.

The necessary second turbine tip speed ratios to obtain the maximum performances are in the range $\lambda_2 \in [4,5]$.

The array efficiency, for a given downstream separation distance, can be compared with respect to the turbulence inflow background level.

It can be pointed out that both in case of 3D and 5D a slightly higher value is reached in case of high turbulence. This is in agreement with the consideration of a faster wake recovery.

A deeper analysis is necessary for the 9D case. As depicted in Figure 4.29 at 9D the array efficiency in the grid configuration is lower than in empty case. This would disprove the registered trend for 3D and 5D separation distances. However the grid effect at 9D after T1 is very low, the predicted turbulence intensity 11D downstream of the grid is evaluated to be $\approx 3\%$ ([39] and Section 4.1.2). T2 inflow conditions in low and high turbulence background level become very similar on T2 rotor, as clear comparing T1 wakes: Figures 4.13 and 4.15 (green lines), as well as Figures 4.14 and 4.16 (green lines). In agreement T2 C_P are similar, so the variation in array

efficiency is due to the different reference T2 C_P used.

In conclusion, Table 4.3 can be devised to summarize the maximum array efficiency that is achievable in each configuration. The necessary operating tip speed ratios are also listed.

Configuration	**Max array efficiency** [%]	$\lambda_1 - \lambda_2$
A	62.8	$5-4$
B	66.5	$5.5-4$
C	78	$5-5$
D	63	$5.5-4$
E	67.5	$6-4.5$
F	77	$6-5$

Table 4.3: Summary of the maximum array efficiency. For each configuration the corresponding tip speed ratios are underlined.

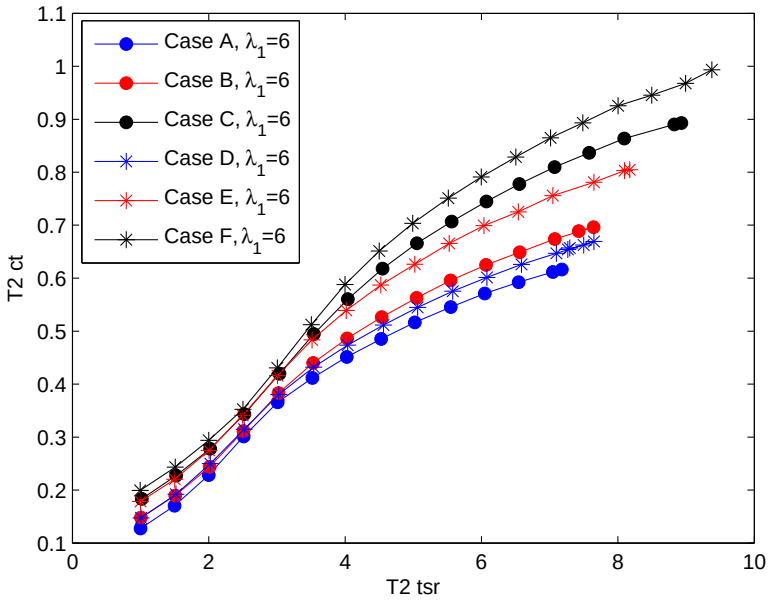

Figure 4.30: T2 thrust coefficients for $\lambda_1 = 6$. Comparison between the different configurations.

As regards T2 thrust coefficient, it can be highlighted that, varying λ_1 in a fixed configuration, C_T is proportional to the T2 maximum achievable power coefficient due to the higher averaged velocity felt by the turbine itself. The different study cases can also be compared. In Figure 4.30 the T2 thrust curves are depicted (the same colour represents the same separation distance, while the same symbols are used for the same inflow condition). T1 tip speed ratio is always set to extract as much energy as possible (i.e. $\lambda_1 = 6$).

Two main trends can be pointed out: the thrust coefficient curve raises both increasing the downstream separation distance and the turbulence inflow background level. Moving further downstream the second turbine (see cases A-B-C and D-E-F) the wake recovery phenomenon allows a higher averaged inflow velocity to T2, causing an amplification in T2 thrust coefficient values; in fact greater C_T values are obtained for bigger distances.

Comparing cases of low and high flow turbulence background level, considering the same separation distance (see cases A-D, B-E and C-F), it is remarkable the increase in C_T values, heightening the turbulence. This effect is achieved through the combination of two factors. The wake recovery is faster in high turbulence case (as already demonstrated in Section 4.2.2), resulting in greater wake averaged velocity for a given downstream distance; moreover the turbulence itself increase the rotor thrust as the single turbine measurements pointed out. The combination of these occurrences results in a much stronger thrust in a high turbulent background level flow.

4.3.4 T1 wake-T2 performance correlation

A wake-rotor interaction can be evaluated by analysing both the velocity deficit in T1 wake at a fixed downstream distance and the C_P curves for T2 operating in that position.

In Figure 4.31(a), the velocity deficit is measured at 3D distance from T1 operating at TSR= 5, 6, 7. As already discussed in Section 4.2.2, in a low background turbulence situation, 3D separation is not enough to allow the transition from near to far wake, so the depicted velocity deficit is representing the near wake area. Thus even small variations in turbine TSR, strongly the affect velocity deficit itself. Consequently, if a second turbine works in this position, its performances will be directly affected by these TSR changes (Figure 4.31(c)). As it is clear from Figure 4.31(a) by increasing the TSR from 5 to 7, velocity deficit peaks become deeper in the region 0.5<y/R<1. Turbine T2, experiencing this flow field, will extract less energy as the rotor sections in the region 0.5<y/R<1 will experience lower velocity. It is called to mind that the outermost part is the most important for power extraction purpose, in fact the first useful blade section is at $y/R \approx 0.2$.

This situation differs from what represented in Figure 4.31(b) and 4.31(d). In 4.31(b) velocity deficit curves are shown behind T1 at 9D distance, in a high turbulence background level. The far wake features are established, resulting in Gaussian velocity deficit profiles, λ_1 independent. Small changes in T1 TSR only marginally affect the C_P curves of a turbine located in this position and this behaviour is clear in Figure 4.31(d).

T1 tip speed ratio variations result to have a different impact on T2 power coefficient curves, depending on T1 wake characteristics. A bigger effort would be required for a deeper understand-

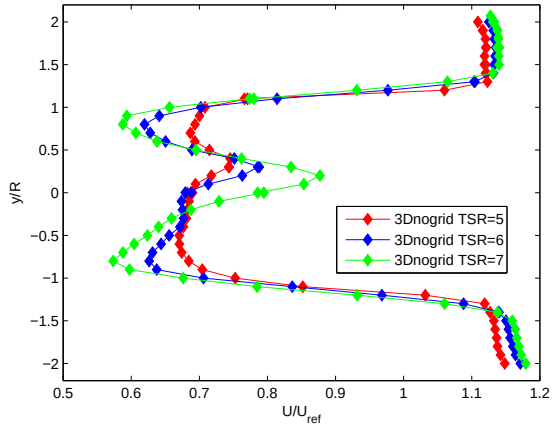

(a) T1 WAKE: 3D distance, low background turbulence

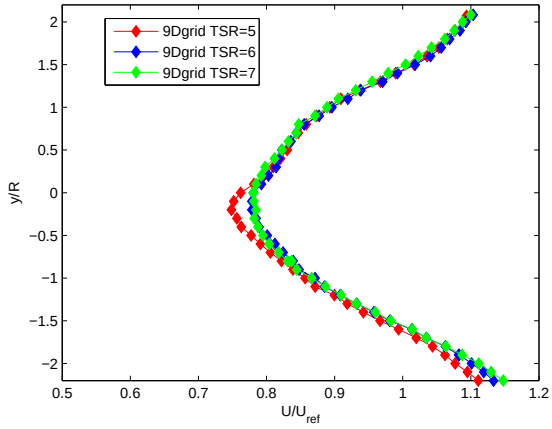

(b) T1 WAKE: 9D distance, high background turbulence

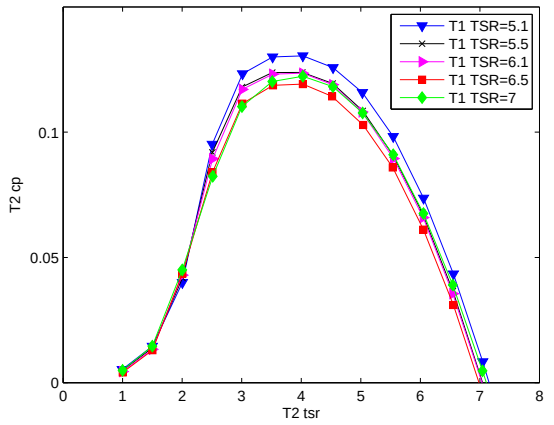

(c) T2 POWER PERFORMANCES:
3D distance, low background turbulence

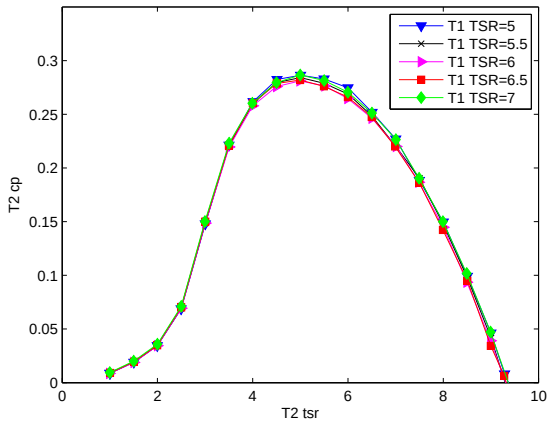

(d) T2 POWER PERFORMANCES:
9D distance, high background turbulence

Figure 4.31: Correlation between T2 incoming flow (T1 wake) and T2 performances.

ing of this interaction, nevertheless a preliminary consideration can be deduced by these experiments: for the tested model turbines, greater the differences in T1 velocity deficit, stronger the effects on T2 power performances.

Chapter 5

Conclusions

In this project, performances and wake measurements downstream a single turbine are performed to asses the different parameters influencing the wake development and structure. Then rotor-wake interaction is evaluated focusing on different parameters affecting the overall power production in a wind farm. The study parameters are: Tip speed ratios of both turbines, separation distance and turbulence level in the incoming flow.

Performances and wake measurements are carried out on stand alone turbines. The rotor aerodynamics of the turbines is tested in two incoming turbulent flow conditions and for several inlet wind speeds. A Re dependency behaviour is observed. In order to avoid this effect, an inlet velocity of 11.5 m/s is setted as reference. The $C_{P,max}$ and the optimum tip speed ratio are recorded for the two flow conditions to have a reference working point necessary for the parameter study in the "wind farm configuration". In a low turbulent background level slightly lower performances are found compared to the results of the high free stream turbulence (10%). At the optimum tip speed ratio ($\lambda = 6$) the maximum C_P values are: 0.47 and 0.48 respectively for turbine T1 and T2 in the low turbulent flow whereas in the high turbulent flow 0.48 and 0.50.

The T1 wake is characterized to analyse its evolution and structure, depending on downstream position, turbine inflow condition and TSR. Velocity deficit and streamwise turbulence intensity are measured on horizontal line at hub height at 3D, 5D and 9D downstream positions. Moving downstream from the rotor plane, velocity deficit recovers as momentum is fed into the wake through the shear layer. Meanwhile, momentum feeding produces the radial expansion of the wake. In a high turbulence background level flow, this effect is much stronger resulting in faster expansion and recovery. It has to be remarked that a free wake expansion is not allowed due to tunnel walls, so these boundary conditions need to be taken into account for modelling this phenomenon. Near-Far wake transition is evaluated in both turbulence level cases underlining

that in the high turbulence case appears earlier due to the higher momentum feeding. The velocity deficit curves in the low turbulence situation does not show a full distinct transition to far wake as, even at 9D, a Gaussian shape is not assumed. Increasing the turbulence level the transition seems to appear much earlier, between 3 to 5D, because of the measured Gaussian velocity deficit curves already at 5D.

Measuring the wake turbulence intensity, tip vortices can be revealed. The magnitude of these peaks is highly dependent on the turbulence background level. At 3D distance, maximum values of TI (15%) are seen, both in case of low and high turbulence level; however it has to be considered that the turbine turbulence generation is different if related to the turbulence background level. Inflow turbulence affects also the wake downstream evolution. Comparing the same downstream positions, the high turbulence level in the flow induces the turbulence intensity peaks to be faster homogenized.

The impact of the turbine operating tip speed ratio on the wake evolution is evaluated. Varying the TSR around the optimum value, the actual angle of attack along the blade is modified, and the effect is detectable on the footprint in the rotor downstream flow. The remarkable conclusions are: the wake expansion is not affected by TSR in both inflow conditions; in near wake region TSR effects are more evident in the inner part of the wake ($y/R \approx 0$). In this area, increasing the TSR, higher velocities are registered because of smaller energy extraction by the inner part of the rotor; turbulence intensity variations are also identified. This behaviour is stronger in low turbulence background level measurements. Regarding the turbulence intensity, increasing the TSR of the turbine, higher values are reached, the reason is in strongest mean velocity gradients achieved.

All the considered parameters are influencing T2 performances as it is working in the T1 wake.

A 2-turbine wind farm is arranged in the tunnel, placing the two models inline in the test section. Focused on obtaining the maximum power output from the array, a parametric study is accomplished, varying the tip speed ratio of both turbines, the separation distance and the turbulence background level in the incoming flow; therefore a benchmark case is obtained.

The array efficiency parameter is introduced (Equation 4.1) to compare the results from the different configurations. The variation of the parameters differently affects the array efficiency.

The downstream separation distance allows to recover the wake velocity deficit, leading to strong variations of the array efficiency. In low turbulent case an increase in efficiency from 3D to 5D of 6.0% is found, and from 3D to 9D of 17.3%. With the grid installed at the inlet, an efficiency recovery of 7.6% is calculated from 3D to 5D, whereas from 3D to 9D is 14.0%. The difference in efficiency recovery is directly connected to the wake evolution along the tunnel. In fact, higher

turbulence induced by the grid accelerates the velocity deficit recovery. Until the grid effect is distinct (5D) the high turbulent case presents a bigger efficiency recovery, whereas it does not appear at 9D as the grid induced turbulence is negligible. Where T1 wakes are very similar (9D), similar efficiency recovery rates are expected, however the values without the grid are bigger because reference power coefficients used are different (Refer to Section 4.3.3 for a complete discussion). In conclusion, the grid can modify the inflow background turbulence level until a certain downstream position ($x/D < 9$); in this region, a general trend of accelerated efficiency recovery is verified.

It is worthy of remark that the grid induced turbulence is decaying along the tunnel, having different effects with respect to the axial stations. This diverge with respect to the real case situation, but the main purpose of wind tunnel experiments is to create a benchmark, in which all boundary conditions are under control and handleable by CFD models.

TSR influence on array performances is accessed too. Varying the tip speed ratio of both turbines, power performance changes can be detected. In order to increase the total power efficiency, T1 TSR can be varied with respect to the stand alone condition. A bigger amount of energy is available for the downstream turbine if λ_1 is not set to optimum. In each configuration, to get the maximum array efficiency, λ_2 has to be set at its actual optimum value ($\lambda_2 \approx 4$). The shift with respect to the stand alone value ($\lambda_2 \approx 6$) depends on the used reference velocity.

A quite constant array efficiency is found over a T1 TSR range: $4.5 \leqslant \lambda_1 \leqslant 6.5$. In low turbulence background level E is constant within $\pm 0.57\%$, while in high turbulent flow E the array efficiency varies of $\pm 1.05\%$. Small differences were expected as the analysed T1 wakes were found not to be strongly dependent on λ_1. A slightly shift towards values smaller than optimum ($\lambda_1 < 6$) seems to show up to obtain the best array efficiency in all configurations: in detail, in low turbulence background level the optimum is achieved for $\lambda_1 \in [5, 5.5]$, while in high turbulence background level for $\lambda_1 \in [5.5, 6]$. However, considering the accuracy range, these differences become very small.

As regards the second turbine thrust coefficient, it can be highlighted that, varying λ_1 in the same configuration, it is proportional to the T2 maximum achievable power coefficient because of the averaged velocity felt by the turbine itself. For a fixed λ_1, the thrust of the second turbine is found to be dependent on turbines separation distance and flow turbulence characteristics. It can be pointed out that the thrust coefficient curve raises both increasing the downstream separation distance and the turbulence inflow background level.

The parametric study points out a strong array efficiency dependency on turbine separation distance and inflow turbulence level. As regards the TSR effect on the array efficiency, it is found

to be small around the optimum point. The relevance is still essential in wind farm optimization, even if in the present wind tunnel study slight variations are found. The parametric study suggests to obtain the maximum array efficiency by an accurate management of the different parameters.

It is worthy of remark that the results on the array efficiency optimization are relative to this peculiar 2-turbines wind farm arranged in the tunnel. Data and considerations can not be directly applied to real cases, but they can still give a good insight on the problem, likewise they can be used as a fully controlled experiment to compare with numerical simulations.

The main goal of creating a benchmark for being compared with numerical simulations has been achieved. An improvement of the insight in the physics of wind turbine rotor-wake interaction has been pursued.

5.1 Limitations

The major limitations found during the present thesis work are following described.

The high solid blockage (14.2%) produces performances modifications in wind tunnel experiments when compared with real case situations and it also affects the wake evolution. However, this effect is not an issue for numerical simulation comparison.

Misalignment inaccuracies of the two turbine rotor axis are not deeply evaluated, while they could interfere in the rotor wake interaction process.

The blades pitch angle is set to zero for all the measurements, anyway some inaccuracies should have been considered as the rotor assembly is designed to be manual.

5.2 Future work

The parametric study can be implemented by increasing the number of parameters. In the current project, the array power output optimization is carried out varying both turbines tip speed ratio, the downstream separation distance and the turbulence background level.

More parameters could be introduced such as yaw angle, blade pitch angle and different incoming flow conditions.

Yawing the turbines the wake evolution will be deflected, so the wake-rotor interaction is modified. This effect results in a different array power output and could be a challenge for modellers.

Pitching the blades will also affect turbine performances and wake structure, adding a possibility for individual turbine control in the perspective of the optimization of the wind farm power output. Therefore it is important that simulation models are calibrated for this parameter.

Different incoming flows can be tested, non uniform flows can be particularly interesting as they would be challenging both in inlet flow simulation and in flow-rotor interaction.

Appendix A

Array configurations: full results

A.1 Configuration A: Empty tunnel, 3D

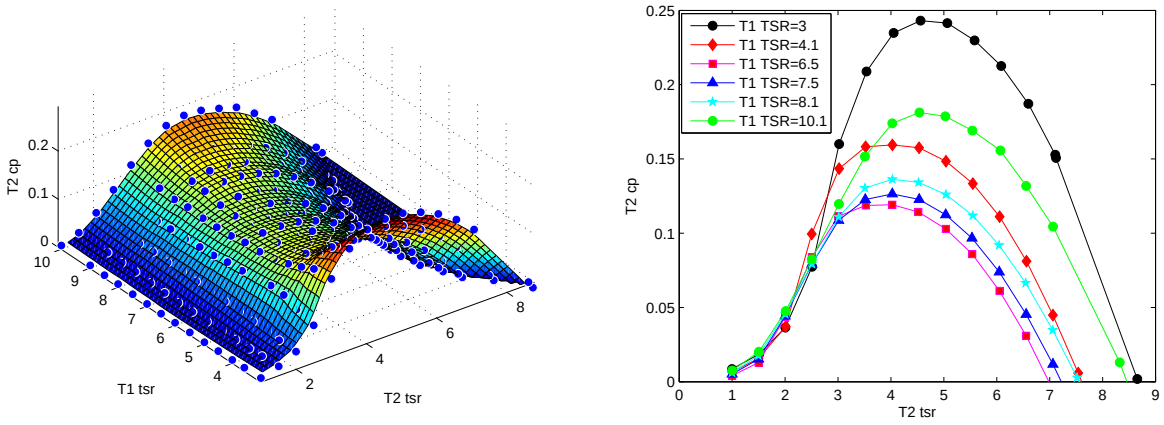

(a) Cp T2 surface

(b) Cp T2 selection of results

Figure A.1: Second turbine T2 power coefficient curves. T2 operating in T1 wake (Configuration A: 3D downstream distance and low turbulence background level).

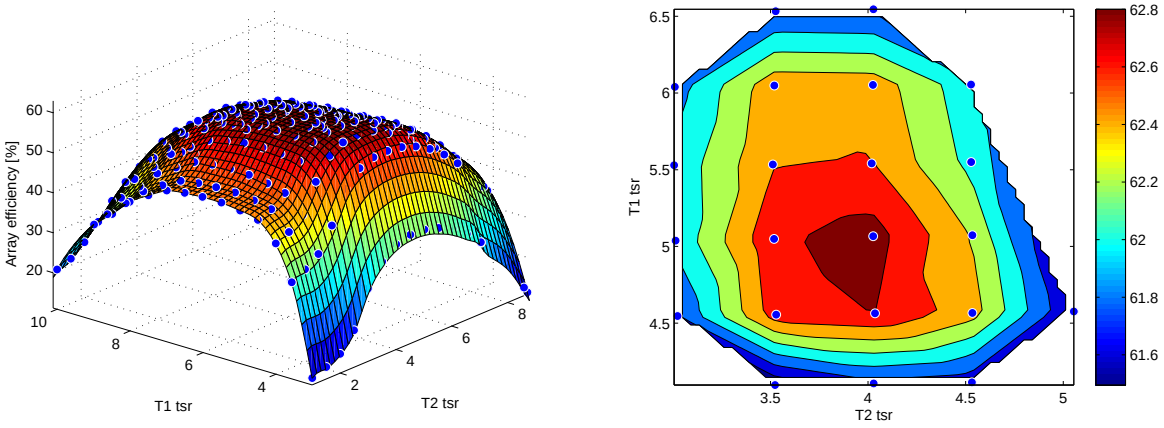

(a) Surface.

(b) Contour plot.

Figure A.2: Array efficiency (Configuration A: 3D downstream distance and low turbulence background level).

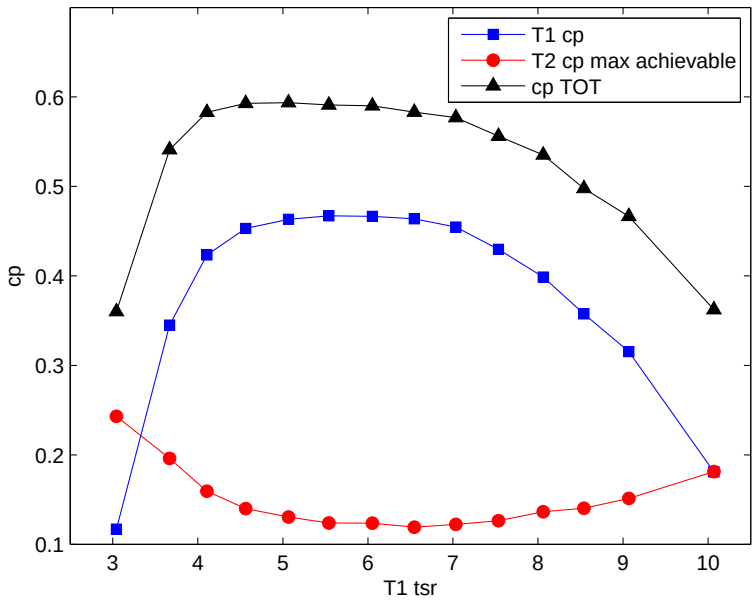

Figure A.3: Summary of Power performances (Configuration A: 3D downstream distance and low turbulence background level).

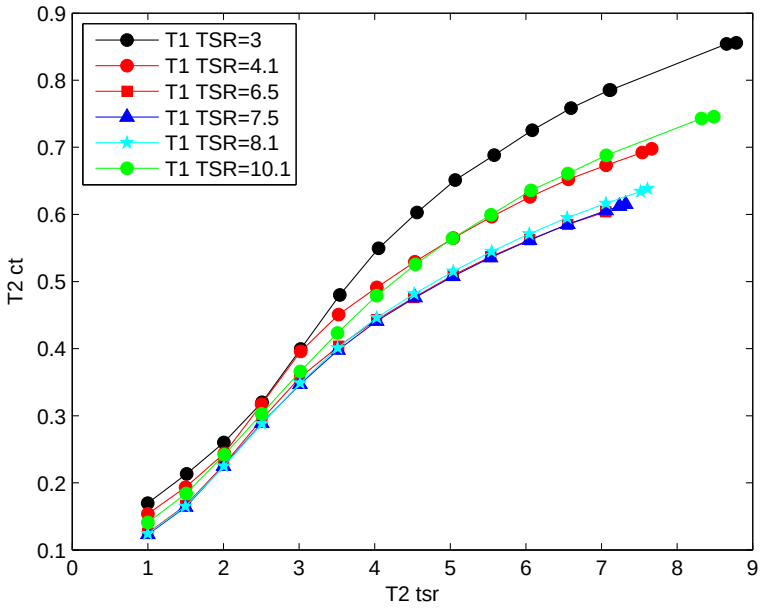

Figure A.4: Second turbine T2 thrust coefficient curves. T2 operating in T1 wake (Configuration A: 3D downstream distance and low turbulence background level).

A.2 Configuration B: Empty tunnel, 5D

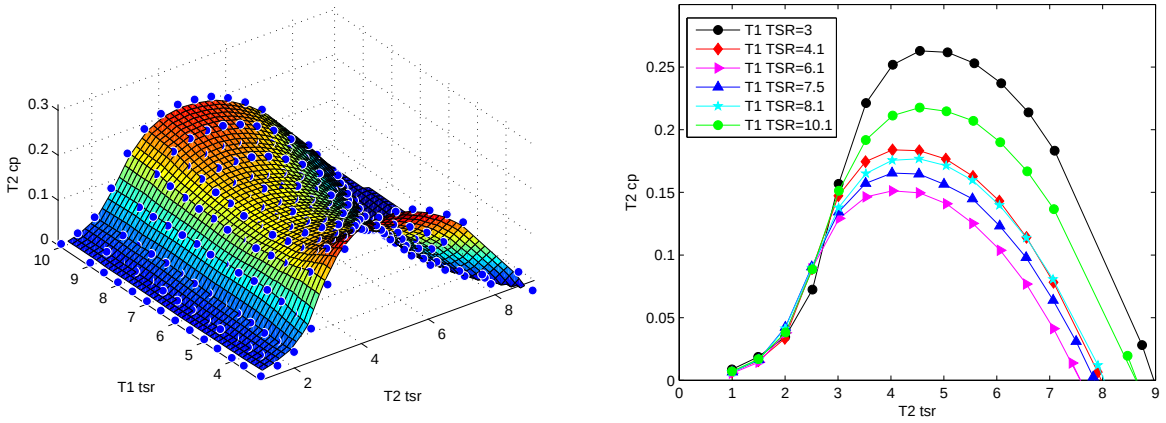

(a) Cp T2 surface

(b) Cp T2 selection of results

Figure A.5: Second turbine T2 power coefficient curves. T2 operating in T1 wake (Configuration B: 5D downstream distance and low turbulence background level).

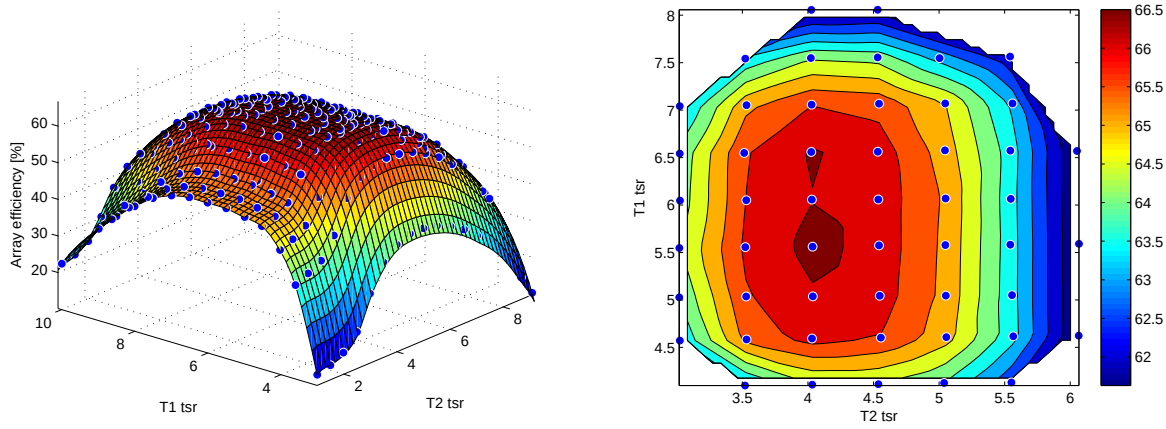

(a) Surface.

(b) Contour plot.

Figure A.6: Array efficiency (Configuration B: 5D downstream distance and low turbulence background level).

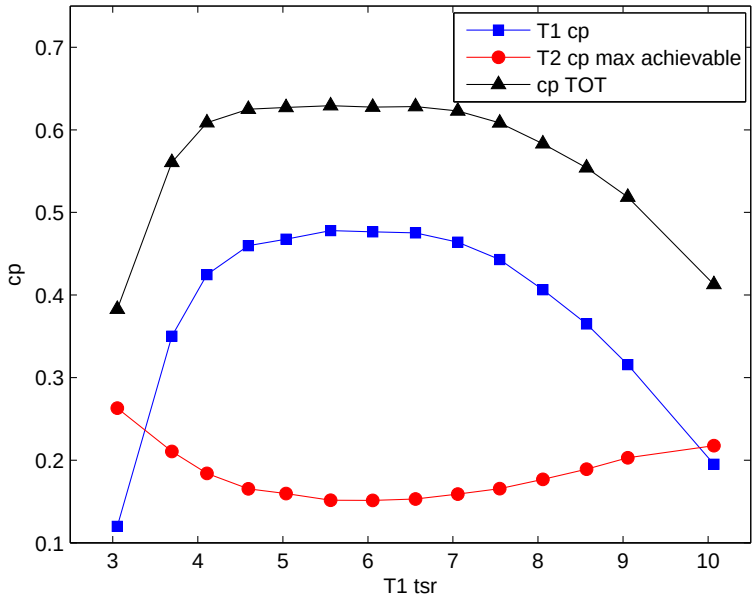

Figure A.7: Summary of Power performances (Configuration B: 5D downstream distance and low turbulence background level).

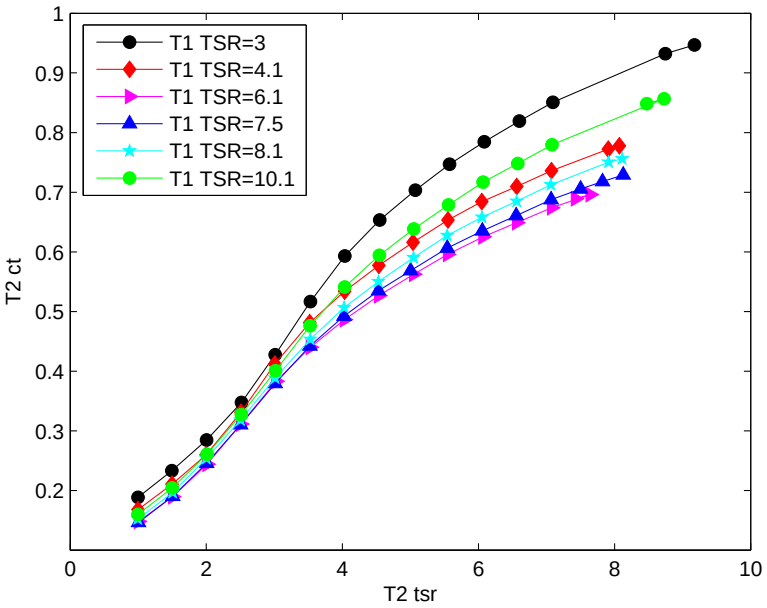

Figure A.8: Second turbine T2 thrust coefficient curves. T2 operating in T1 wake (Configuration B: 5D downstream distance and low turbulence background level).

A.3 Configuration C: Empty tunnel, 9D

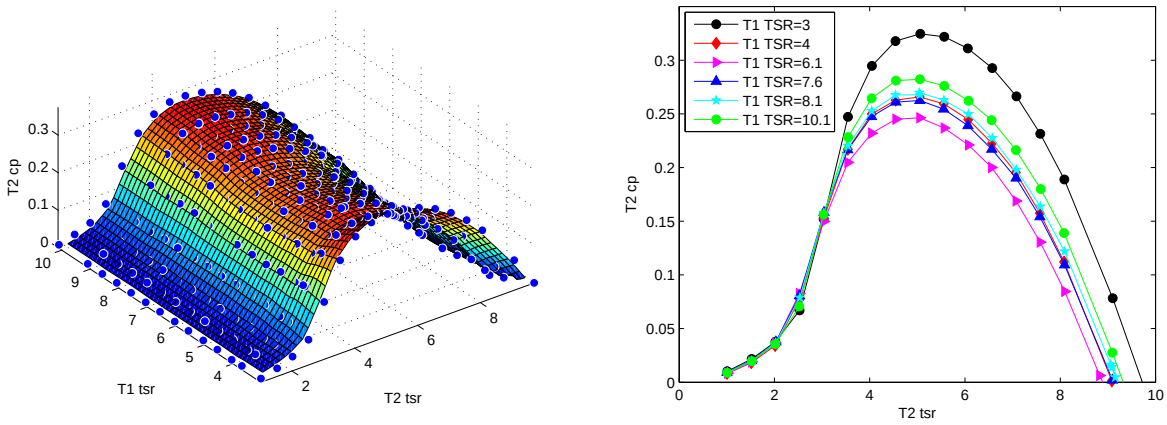

(a) Cp T2 surface

(b) Cp T2 selection of results

Figure A.9: Second turbine T2 power coefficient curves. T2 operating in T1 wake (Configuration C: 9D downstream distance and low turbulence background level).

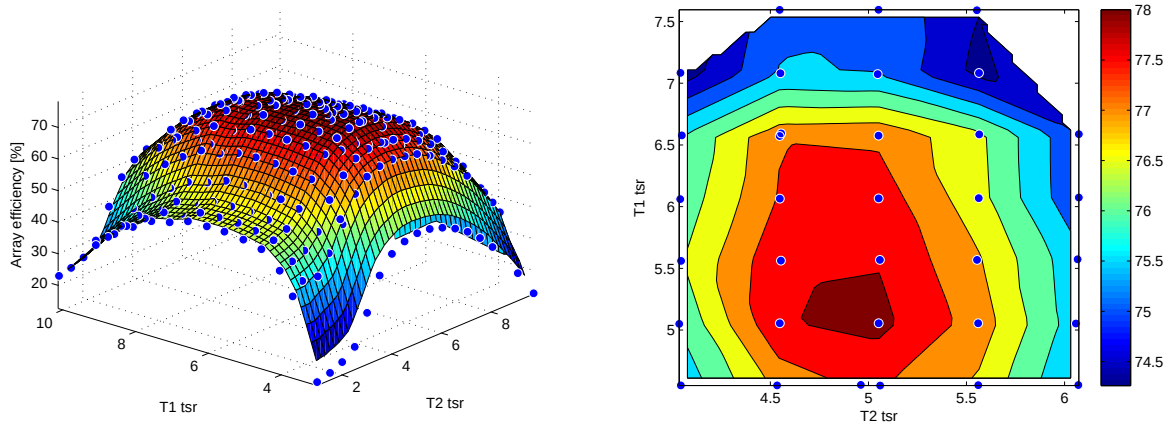

(a) Surface.

(b) Contour plot.

Figure A.10: Array efficiency (Configuration C: 9D downstream distance and low turbulence background level).

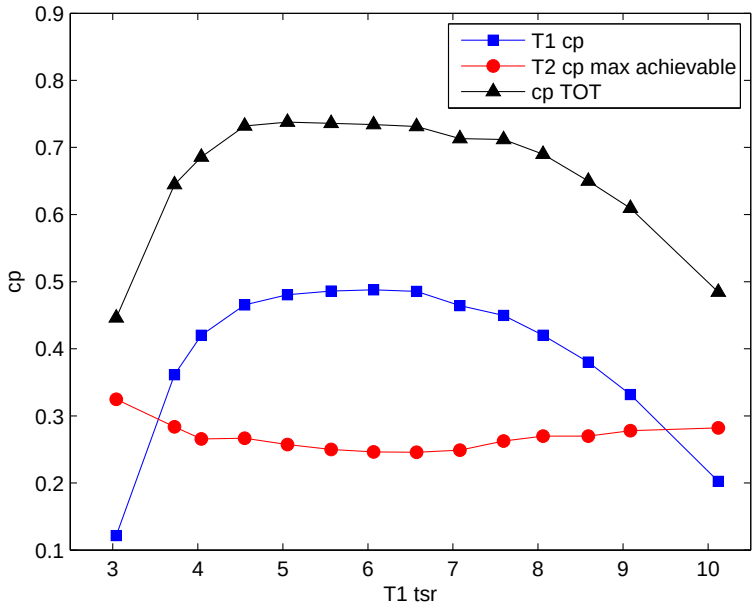

Figure A.11: Summary of Power performances (Configuration C: 9D downstream distance and low turbulence background level).

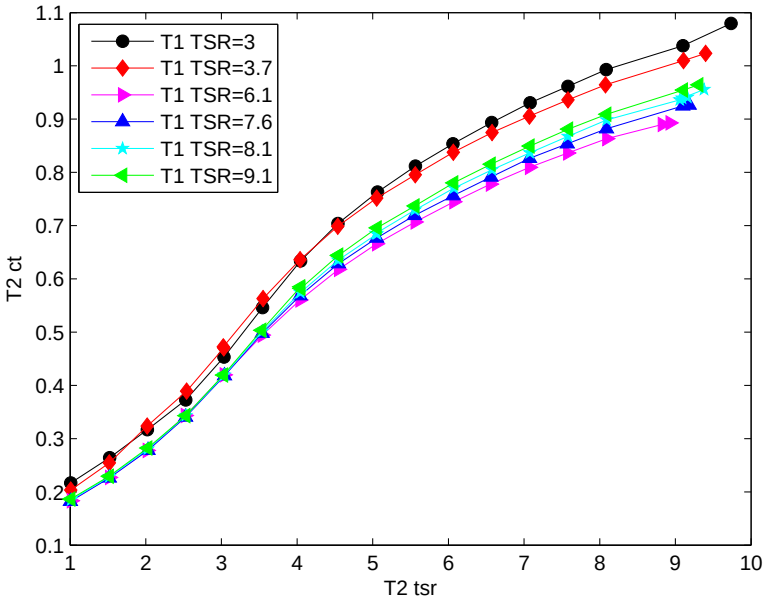

Figure A.12: Second turbine T2 thrust coefficient curves. T2 operating in T1 wake (Configuration C: 3D downstream distance and low turbulence background level).

A.4 Configuration D: Grid, 3D

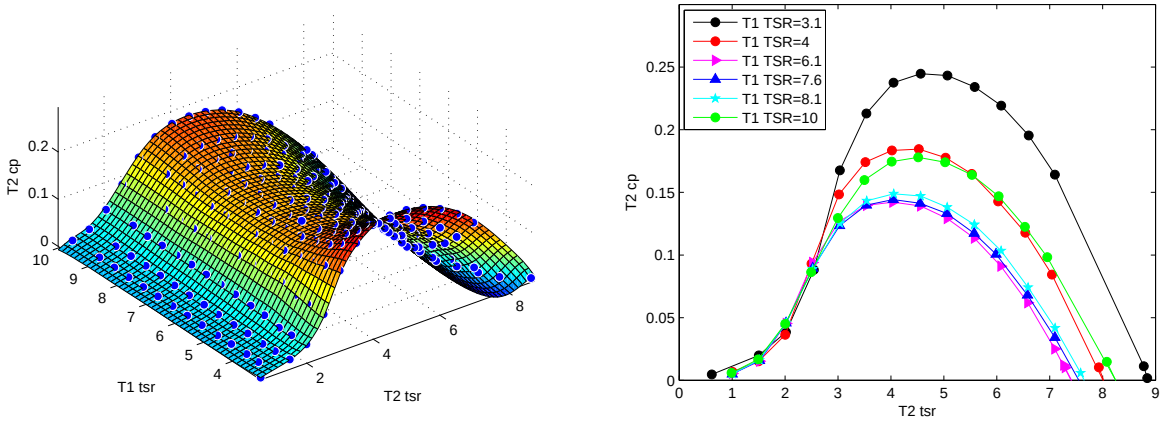

(a) Cp T2 surface

(b) Cp T2 selection of results

Figure A.13: Second turbine T2 power coefficient curves. T2 operating in T1 wake (Configuration D: 3D downstream distance and high turbulence background level).

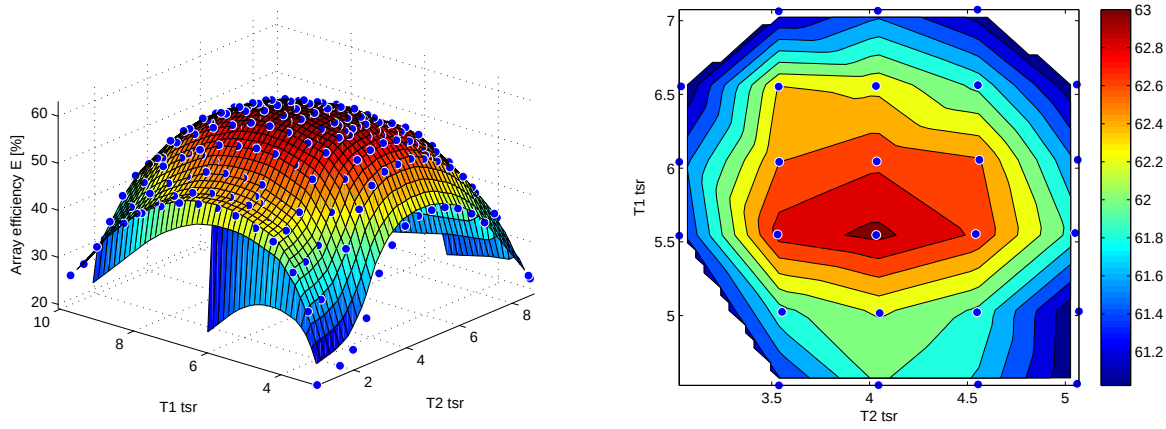

(a) Surface

(b) Contour plot.

Figure A.14: Array efficiency (Configuration D: 3D downstream distance and high turbulence background level).

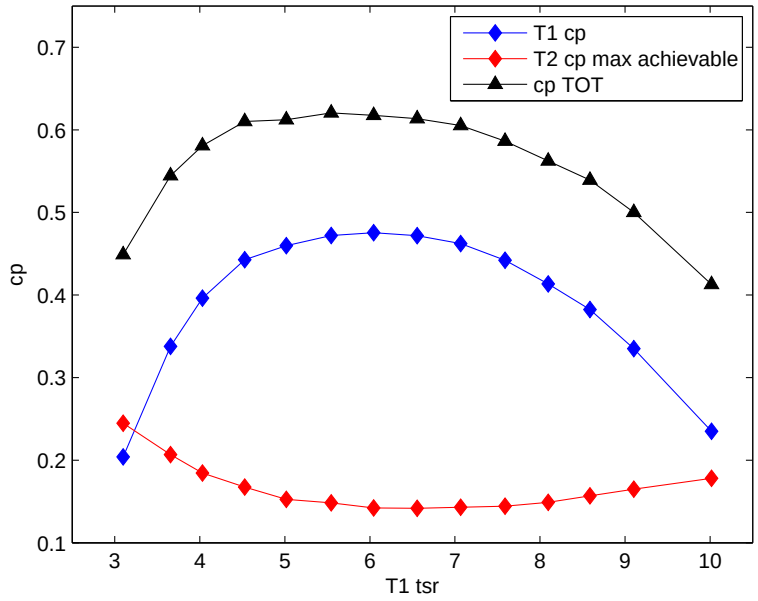

Figure A.15: Summary of Power performances (Configuration D: 3D downstream distance and high turbulence background level).

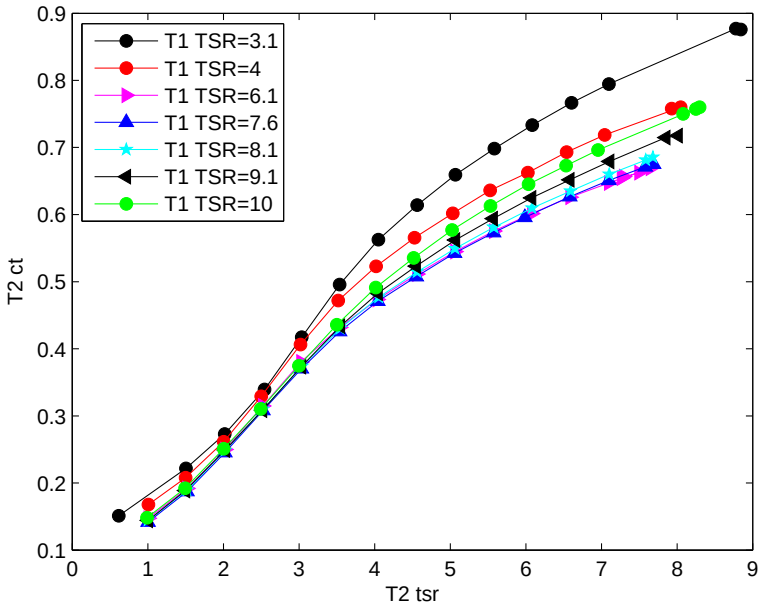

Figure A.16: Second turbine T2 thrust coefficient curves. T2 operating in T1 wake (Configuration D: 3D downstream distance and high turbulence background level).

A.5 Configuration E: Grid, 5D

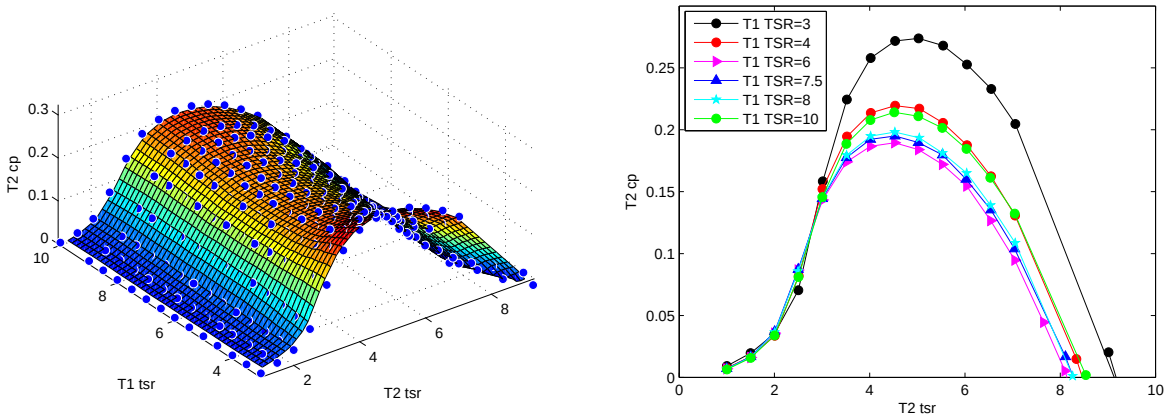

(a) Cp T2 surface

(b) Cp T2 selection of results

Figure A.17: Second turbine T2 power coefficient curves. T2 operating in T1 wake (Configuration E: 5D downstream distance and high turbulence background level).

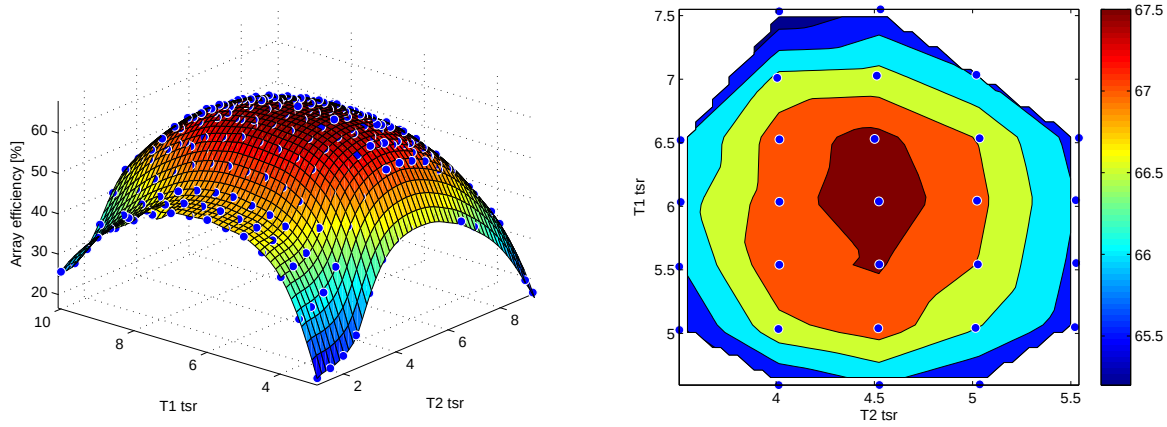

(a) Surface.

(b) Contour plot.

Figure A.18: Array efficiency (Configuration E: 5D downstream distance and high turbulence background level).

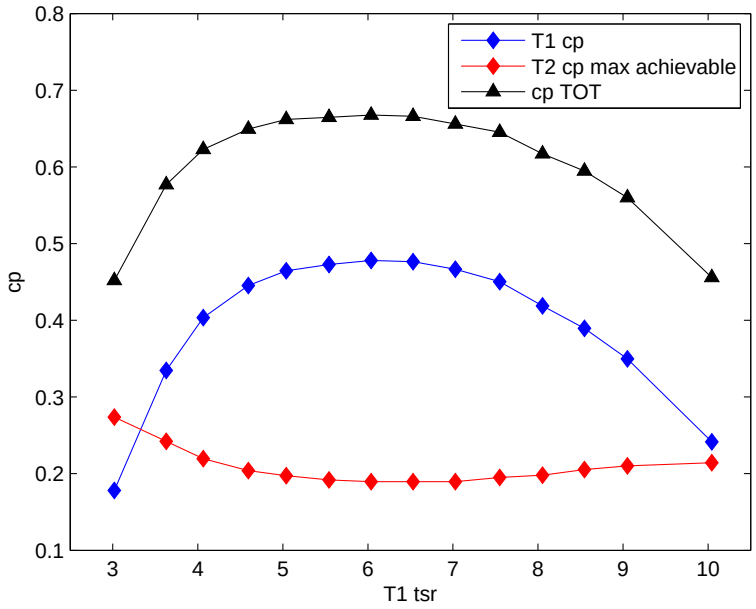

Figure A.19: Summary of Power performances (Configuration E: 5D downstream distance and high turbulence background level).

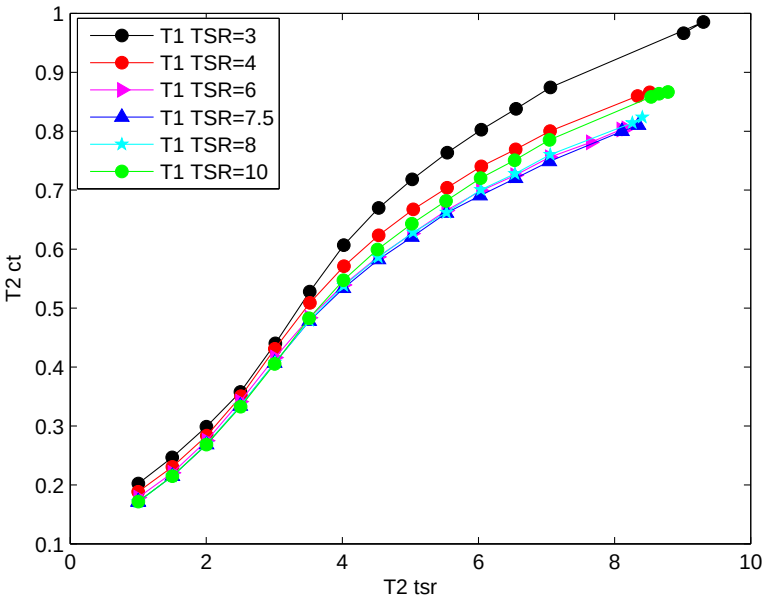

Figure A.20: Second turbine T2 thrust coefficient curves. T2 operating in T1 wake (Configuration E: 5D downstream distance and high turbulence background level).

A.6 Configuration F: Grid, 9D

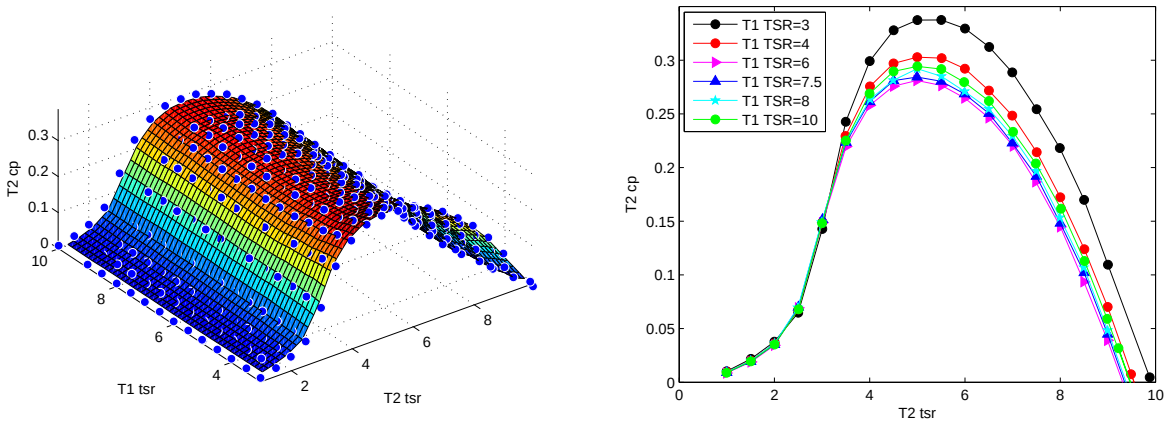

(a) Cp T2 surface

(b) Cp T2 selection of results

Figure A.21: Second turbine T2 power coefficient curves. T2 operating in T1 wake (Configuration F: 9D downstream distance and high turbulence background level).

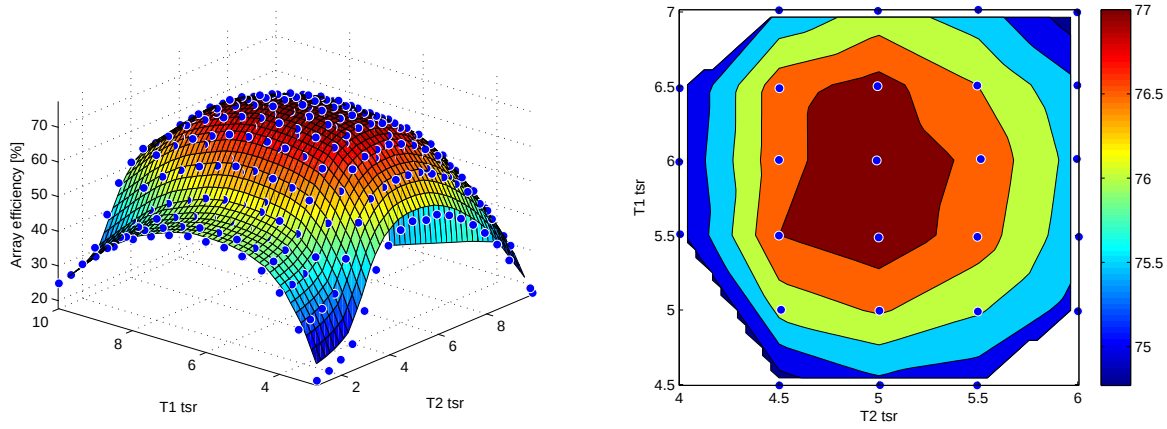

(a) Surface.

(b) Contour plot.

Figure A.22: Array efficiency (Configuration F: 9D downstream distance and high turbulence background level).

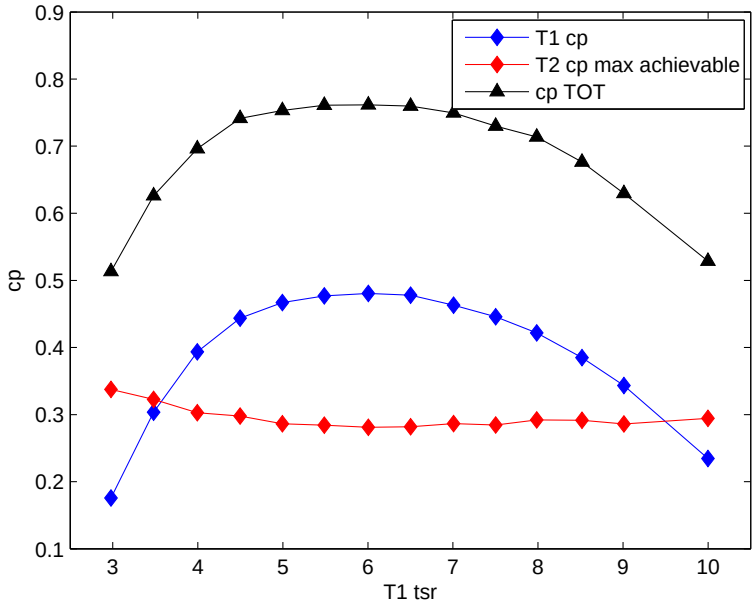

Figure A.23: Summary of Power performances (Configuration F: 9D downstream distance and high turbulence background level).

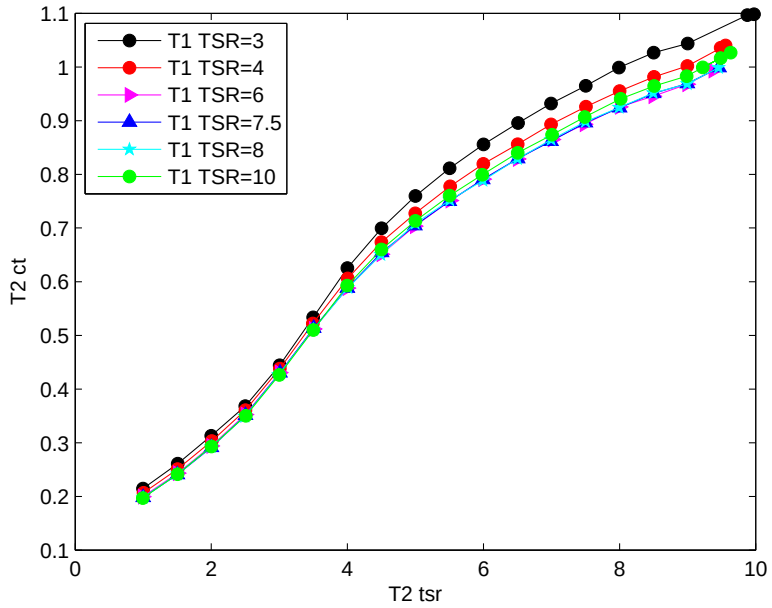

Figure A.24: Second turbine T2 thrust coefficient curves. T2 operating in T1 wake (Configuration F: 9D downstream distance and high turbulence background level).

References

[1] Tony Burton. *Wind energy handbook*. Wiley, Chichester, West Sussex, 2011.

[2] J.F. Manwell, J.G. McGowan, and A.L. Rogers. *Wind Energy Explained*. Chicester : John Wiley & Sons, Ltd., 2010.

[3] B Sanderse. Aerodynamics of wind turbine wakes. *Energy Research Center of the Netherlands (ECN), ECN-E–09-016, Petten, The Netherlands, Tech. Rep*, 2009.

[4] S. A Ivanell. *Numerical Computation of Wind Turbine Wakes*. PhD thesis, Gotland University, 2009.

[5] Jan Bartl. Wake measurements behind an array of two model wind turbines. Master's thesis, Norwegian University of Science and Technology, Department of Energy and Process Engineering, 2011.

[6] Kjersti Røkenes. *Investigation of terrain effects with respect to wind farm siting*. PhD thesis, Norwegian University of Science and Technology, Department of Energy and Process Engineering, 2009.

[7] S. Sarmast. *Numerical study on instability and interaction of wind turbine wakes*. PhD thesis, KTH Stockholm, 2013.

[8] Per-Åge Krogstad and J.A. Lund. An experimental and numerical study of the performance of a model turbine. *Wind Energy*, 15(3):443–457, 2012.

[9] Finn E. Jorgensen. *How to measure turbulence with hot-wire anemometers: a practical guide*. Dantec Dynamics, 2002.

[10] G.H. Brundtland, World Commission on Environment, and Development. *Report of the World Commission on Environment and Development: "our Common Future" : Annex*. UN, 1987.

[11] Søren Krohn Poul-Erik Morthorst Shimon Awerbuch. The economics of wind energy. Technical report, European Wind Energy Association, 2009.

[12] Dr. Jami Hossain Nopenyo Dabla Danish Ahmad. World wind resource assessment report. Technical report, World Wind Energy Association, December 2014.

[13] Jørgen Højstrup. Spectral coherence in wind turbine wakes. *Journal of Wind Engineering and Industrial Aerodynamics*, 80(1–2):137 – 146, 1999.

[14] Fabio Pierella. *Experimental Investigation of Wind Turbine Wakes and Their Interaction*. PhD thesis, NTNU, 2014.

[15] Jan-Ake Dahlberg. Assessment of the lillgrund wind farm: power performance wake effects. *Vattenfall Vindkraft AB, 6_1 LG Pilot Report, http://www. vattenfall. se/sv/file/15_Assessment_of_the_Lillgrund_W. pdf_16596737. pdf (cited March 30, 2012)*, 2009.

[16] M. Steinbuch, W.W. de Boer, O.H. Bosgra, S.A.W.M. Peters, and J. Ploeg. Optimal control of wind power plants. *Journal of Wind Engineering and Industrial Aerodynamics*, 27(1–3):237 – 246, 1988.

[17] GP Corten, P Schaak, and ETG Bot. More power and less loads in wind farms - heat and flux. In *European Wind Energy Conference Exhibition, London, UK*, 2004.

[18] Gunner Chr Larsen, Helge Aagaard Madsen, Niels Troldborg, Torben J Larsen, Pierre-Elouan Réthoré, Peter Fuglsang, Søren Ott, Jakob Mann, Thomas Buhl, Morten Nielsen, et al. Topfarm-next generation design tool for optimisation of wind farm topology and operation. Technical report, Danmarks Tekniske Universitet, Risø Nationallaboratoriet for Bæredygtig Energi, 2011.

[19] Daria Madjidian and Anders Rantzer. A stationary turbine interaction model for control of wind farms. In *IFAC 18th World Congress*, 2011.

[20] Jaejoon Lee, Eunkuk Son, Byungho Hwang, and Soogab Lee. Blade pitch angle control for aerodynamic performance optimization of a wind farm. *Renewable Energy*, 54:124–130, 2013.

[21] Kristine Mikkelsen. Effect of free stream turbulence on wind turbine performance, 2013.

[22] H. Glauert. Airplane propellers. In *Aerodynamic Theory*, pages 169–360. Springer Berlin Heidelberg, 1935.

[23] M.O. Hansen. *Aerodynamics of wind turbines : rotors, loads and structure / Martin O.L. Hansen.* London : James & James, 2000.

[24] Karin Åhlund. investigation of the nrel nasa/ames wind turbine aerodynamics database. Technical report, Swedish Defence Research Agency, 2004.

[25] L.J. Vermeer, J.N. Sørensen, and A. Crespo. Wind turbine wake aerodynamics. *Progress in Aerospace Sciences*, 39:467 – 510, 2003.

[26] C.G. Helmis, K.H. Papadopoulos, D.N. Asimakopoulos, P.G. Papageorgas, and A.T. Soilemes. An experimental study of the near-wake structure of a wind turbine operating over complex terrain. *Solar Energy*, 54(6):413 – 428, 1995.

[27] J.D. Anderson. *Fundamentals of aerodynamics.* Singapore : McGraw-Hill, 2011.

[28] D Smith and GJ Taylor. Further analysis of turbine wake development and interaction data. In *Proceedings of the 13th BWEA Wind Energy Conference, Swansea, UK*, pages 325–331, 1991.

[29] L. P. Chamorro, M. Guala, R.E.A. Arndt, and F. Sotiropoulos. On the evolution of turbulent scales in the wake of a wind turbine model. *Journal of Turbulence*, page N27, 2012.

[30] M.S. Adaramola and P.-A. Krogstad. Experimental investigation of wake effects on wind turbine performance. *Renewable Energy*, 36(8):2078 – 2086, 2011.

[31] D. M. Somers. *S825 and S826 Airfoils: 1994–1995.* Jan 2005.

[32] Per-Åge Krogstad and Muyiwa S. Adaramola. Performance and near wake measurements of a model horizontal axis wind turbine. *Wind Energy*, 15(5):743–756, 2012.

[33] John Amund Karlsen. Performance calculations for a model turbine. Master's thesis, NTNU, 2009.

[34] Per-Åge Krogstad and Pål Egil Eriksen. "blind test" calculations of the performance and wake development for a model wind turbine. *Renewable Energy*, 50(0):325–333, February 2013.

[35] S. Goldstein. A note on the measurement of total head and static pressure in a turbulent stream. *Proceedings of the Royal Society of London A: Mathematical, Physical and Engineering Sciences*, 155(886):570–575, 1936.

[36] D. Olivari and M. Carbonaro. *Hot wire measurements. Measurements techiques in Fluid Dynamics. An Introduction.* Von Karman Institute for Fluid Dynamics, 1994.

[37] E.O. Doebelin. *Measurement systems : application and design / Ernest O. Doebelin.* Boston : McGraw-Hill Higher Education, 2004.

[38] Ganji A. Wheeler, A. and V. Krishnan. *Introduction to Engineering Experimentation.* Upper Saddle River, 2004.

[39] S.B. Pope. *Turbulent flows / Stephen B. Pope.* Cambridge : Cambridge University Press, 2000.

[40] Fabio Pierella, Per-Age Krogstad, and Lars Setran. Blind test 2 calculations for two in-line model wind turbines where the downstream turbine operates at various rotational speeds. *Renewable Energy*, 70(0):62–77, October 2014.

[41] Kari Medby Loland. Wind turbine in yawed operation. Master's thesis, NTNU, 2011.

[42] Majid Bastankhah and Fernando Porte-Agel. A new analytical model for wind-turbine wakes. *Renewable Energy*, 70(0):116 – 123, 2014. Special issue on aerodynamics of offshore wind energy systems and wakes.

[43] N. O. Jensen. A note on wind generator interaction. Technical report, Risø National Laboratory, Roskilde, Denmark, 1983.

[44] Larsen GC Rados K. Pryor SC Frandsen et al. Barthelmie RJ, Folkerts L. Comparison of wake model simulation with off-shore wind turbine wake profiles mmeasure by sodar. *Journal of Atmospheric Ocean Technol.*, 2005.

[45] Jensen LE Barthelmie RJ. Evaluation of wind farm efficiency and wind turbine wakes at the nysted off-shore wind farm. *Wind Energy*, 13:573–86, 2010.

[46] Enevoldsen P. Bikermose B. Jensen L. Cleve J, Greyner M. Model-based analysis of wake flow data in the nysted offshore wind farm. *Wind Energy*, 2009.